

# Allowed region of the mean values of angular momentum observables and their uncertainty relations

Arun Sehrawat<sup>1,\*</sup>

<sup>1</sup>*Harish-Chandra Research Institute, HBNI, Chhatnag Road, Jhansi, Allahabad 211019, India*

The expectation values of operators drawn from a single quantum state cannot be outside of a particular region, called their allowed region or the joint numerical range of the operators. Basically, the allowed region is an image of the state space under the Born rule. The maximum-eigenvalue-states—of every linear combination of the operators of interest—are sufficient to generate boundary of the allowed region. In this way, we obtain the numerical range of certain Hermitian operators (observables) that are functions of the angular momentum operators. Especially, we consider here three kinds of functions—combinations of powers of the ladder operators, powers of the angular momentum operators and their anticommutators—and discover the allowed regions of different shapes. By defining some specific concave (and convex) functions on the joint numerical range, we also achieve tight uncertainty (and certainty) relations for the observables. Overall, we demonstrate how the numerical range and uncertainty relations change as the angular momentum quantum number grows. Finally, we apply the quantum de Finetti theorem by taking a multi-qubit system and attain the allowed regions and tight uncertainty relations in the limit where the quantum number goes to infinity.

## I. INTRODUCTION

Can the numbers in  $\vec{r} = (x, y, \dots, z)$  be the expectation values—obtained from a single state  $\rho$ —of the operators in  $\vec{E} = (X, Y, \dots, Z)$ ? To provide a definite “yes or no” answer, we need to know the region  $\mathcal{E}$  of all possible mean vectors  $\vec{e} := \langle \vec{E} \rangle_\rho$  for a given vector operator  $\vec{E}$ . If and only if  $\vec{r} \in \mathcal{E}$  then there exists at least one  $\rho$  such that  $\vec{r} = \vec{e}$ , thus  $\mathcal{E}$  is called *allowed region* of the mean values. The allowed region is also known as the joint numerical range [1, 2] and the quantum convex support [3] of  $\vec{E}$ .

Only pure states  $\rho = \rho^2$  are usually considered to define the numerical range [4–6], but here we take the whole state space that includes mixed states. Hence,  $\mathcal{E}$  is always a convex set. Here, we are interested in  $\mathcal{E}$  for  $n$  *bounded* Hermitian operators (observables) of a  $d$ -level quantum system (qudit), where  $n$  and  $d$  are finite numbers, and we treat  $d \rightarrow \infty$  as a limiting case. Many important results about the numerical range of  $n = 2$  Hermitian operators are contained in Book [4].

Although the numerical range is largely investigated in mathematics, recently it is used to study the phase transitions [2, 7–11]. The numerical range also plays a central role in [1, 2, 12], where numerical techniques are provided to get—an uncertainty relation (UR)—a state-independent lower bound of the sum of squared standard deviations of two observables. A UR based on such a sum is introduced in [13]. In [14], the Wigner distribution is built on the numerical range of a set of observables, and its properties are analyzed.

In Sec. II, we present a simple procedure to obtain  $\mathcal{E}$  for a general  $\vec{E}$ . It is—taken from [1, 2, 7] and Chap. 5 in [4]—established on the fact that all the expectation

values of a Hermitian operator lie between its extreme eigenvalues. If we consider operators  $\hat{\eta} \cdot \vec{E}$  for all real unit vectors  $\hat{\eta} \in \mathbb{R}^n$ , then it will be sufficient to draw the boundary  $\partial\mathcal{E}$  of the permitted region by using the above fact. Since  $\mathcal{E}$  is a convex and bounded set in  $\mathbb{R}^n$  in the case of bounded operators, it is completely specified by its boundary, and  $\partial\mathcal{E} \subseteq \mathcal{E}$  for a finite  $d$  [4]. In [15] a different scheme—based on a result from [16, 17] about the positivity of  $\rho$ —is provided to get the allowed region  $\mathcal{E}$ . There it is shown how to build uncertainty and certainty measures on  $\mathcal{E}$  to achieve a tight UR and certainty relation (CR), which is briefly repeated in Sec. II.

For a qubit,  $d = 2$ ,  $\partial\mathcal{E}$  is always an ellipsoid (possibly degenerate) [15, 18–20], and every tight UR and CR can be achieved by using it [15, 19, 21]. In the case of a qutrit,  $d = 3$ , all possible shapes of  $\mathcal{E}$  are classified in [5, 6] for  $n = 2, 3$  Hermitian operators. In any dimension  $d$ , the joint numerical range of a pair of projectors that have no common eigenvector is the convex hull of two ellipses [22, 23]. To specify  $\mathcal{E}$  for an arbitrary  $\vec{E}$  in a higher dimension is a difficult task, therefore we consider the angular momentum operators in Sec. III and their polynomials in Secs. IV–VIII at the places of  $X, Y, \dots, Z$  and present  $\mathcal{E}$ , tight URs, and CRs for the angular momentum quantum numbers  $j = \frac{d-1}{2} = \frac{1}{2}, 1, \frac{3}{2}, 2, \dots$ . There are known URs for the angular momentum operators [24–28], but our uncertainty measures and URs are different as described in Sec. II.

Our main contribution lies in Secs. IV–VIII and Appendix, while Secs. II and III are kept to introduce necessary notations for the paper. Basically, we consider three types of operators: combinations of powers of the ladder operators in Sec. IV, powers of the angular momentum operators in Secs. V, VII, and VIII and their anticommutators in Secs. VI and VIII. The quadratic polynomials of the momentum operators in these sections are responsible for the spin squeezing [29].

\* Email: arunsehrawat@hri.res.in

We want to emphasize that the plots given in Sec. V for the boundary  $\partial\mathcal{E}$  already appeared in [10], where the authors used a multi-qubit system that inspires Sec. VIII here. In Sec. VIII, we choose a multi-qubit system and use the quantum de Finetti theorem [30, 31] to obtain the allowed regions—for the operators investigated in the earlier sections—in the limit  $j \rightarrow \infty$ . We summarize the main results and present an outlook in Sec. IX.

## II. ALLOWED REGION AND UNCERTAINTY MEASURES ON IT

With a given density operator  $\rho$  on a  $d$ -dimensional Hilbert space  $\mathcal{H}_d$ , one can compute the average values of all the  $n$  Hermitian operators in  $\vec{E} = (X, Y, \dots, Z)$  by the Born rule. The rule can be perceived as a linear map

$$\rho \longmapsto \text{tr}(\rho \vec{E}) = \langle \vec{E} \rangle_\rho = \vec{\varepsilon} \quad (1)$$

from the state space  $\Omega$  onto the allowed region, also known as the joint numerical range [1, 2],

$$\mathcal{E} := \{ \vec{\varepsilon} \mid \rho \in \Omega \} \subset \mathbb{R}^n. \quad (2)$$

Basically,  $\Omega$  is the collection of all positive semidefinite operators, on  $\mathcal{H}_d$ , with the unit trace. We often write  $\langle \cdot \rangle_\rho$  without the subscript as all the mean values in  $\vec{\varepsilon}$  are drawn from a same state  $\rho$ .

For a single Hermitian operator  $X = X^\dagger$ ,  $\mathcal{E}$  is just the closed interval  $[x_m, x_M]$  that includes all real numbers between the minimum and maximum eigenvalues of  $X$  [4]. The numerical range  $\mathcal{E}$  of  $\vec{E}$  is always a convex set because  $\Omega$  is. As long as the dimension  $d$  is finite,  $\mathcal{E}$  is also a compact (closed and bounded) set [32] in a hyperrectangle specified by the Cartesian product

$$\mathcal{H} := [x_m, x_M] \times [y_m, y_M] \times \dots \times [z_m, z_M] \quad (3)$$

of closed intervals bounded by the extreme eigenvalues of the operators in  $\vec{E}$ .  $\mathcal{E}$  touches each facet of the hyperrectangle at some points that come from the smallest- or largest-eigenvalue-states of one of the  $n$  operators. If  $X, Y, \dots, Z$  mutually commute—that is,  $XY = YX$  and so on—then we can find their common eigenbasis  $\{|\mathbf{e}_l\rangle\}_{l=1}^d$ . And,  $\mathcal{E}$  will be a convex polytope

$$\text{Conv} \{ \langle \mathbf{e}_l | \vec{E} | \mathbf{e}_l \rangle \mid l = 1, \dots, d \} \quad (4)$$

in  $\mathbb{R}^n$ . The convex hull of a set  $\{\dots\}$  is denoted by  $\text{Conv}\{\dots\}$ . All the extreme points of (4) will be a subset of  $\{\langle \mathbf{e}_l | \vec{E} | \mathbf{e}_l \rangle\}_{l=1}^d$ . An extreme point of  $\mathcal{E}$  inevitably comes from a pure state—that is an extreme point of the state space  $\Omega$ —but not every pure state provides an extreme point of  $\mathcal{E}$  unless (1) is a bijective mapping.

The following procedure to obtain  $\mathcal{E}$  is borrowed from [1, 2, 7] and Chap. 5 in [4], and a different method is given in [15]. Let us take  $n = 3$  Hermitian operators  $X, Y$ , and  $Z$ , and the procedure can be extended to any number

of operators. First, we build a two-parameter family of operators as

$$\Lambda(\theta, \phi) := \hat{\eta}(\theta, \phi) \cdot \vec{E}, \quad \text{where } \vec{E} = (X, Y, Z), \quad (5)$$

$$\hat{\eta}(\theta, \phi) := (\sin \theta \cos \phi, \sin \theta \sin \phi, \cos \theta), \quad (6)$$

$\theta \in [0, \pi]$ , and  $\phi \in [0, 2\pi)$ . An eigenvalue and eigenket of  $\Lambda$ ,

$$\Lambda(\theta, \phi) |\lambda(\theta, \phi)\rangle = \lambda(\theta, \phi) |\lambda(\theta, \phi)\rangle, \quad (7)$$

generally depend on the angles  $\theta$  and  $\phi$ . We call a density operator  $\varrho$  an eigenstate associated with an eigenvalue  $\lambda$  of  $\Lambda$  if and only if  $\Lambda\varrho = \lambda\varrho = \varrho\Lambda$ .

For every  $(\theta, \phi)$ , there are lower and upper bounds

$$\lambda_m(\theta, \phi) \leq \langle \Lambda(\theta, \phi) \rangle_\rho \leq \lambda_M(\theta, \phi), \quad (8)$$

where  $\lambda_m$  and  $\lambda_M$  are the minimum and maximum eigenvalues of  $\Lambda$ . It is sufficient to take only the maximum eigenvalues  $\lambda_M$  because  $\Lambda(\pi - \theta, \pi + \phi) = -\Lambda(\theta, \phi)$  and the smallest eigenvalue of  $\Lambda(\theta, \phi)$  is the largest eigenvalue of  $\Lambda(\pi - \theta, \pi + \phi)$ . Or, equivalently, one can keep both the eigenvalues and take  $\theta, \phi \in [0, \pi]$ .

Now let us define a supporting (tangent) hyperplane

$$\mathbb{H}(\theta, \phi) := \{ \vec{r} = (x, y, z) \in \mathbb{R}^3 \mid \hat{\eta}(\theta, \phi) \cdot \vec{r} = \lambda_m(\theta, \phi) \} \quad (9)$$

of  $\mathcal{E}$  with the normal vector  $\hat{\eta}(\theta, \phi)$ . According to the right-hand-side inequality in (8)—that is,

$$\hat{\eta}(\theta, \phi) \cdot \vec{\varepsilon} \leq \lambda_M(\theta, \phi) \quad (10)$$

due to (5) and (6)—the allowed region  $\mathcal{E}$  is enclosed by these tangent planes for all  $\theta$ 's and  $\phi$ 's. For each  $(\theta, \phi)$ , the intersection

$$\mathbb{H}(\theta, \phi) \cap \mathcal{E} =: \mathcal{F}(\theta, \phi) \quad (11)$$

is called a proper *face* of  $\mathcal{E}$ . The boundary of  $\mathcal{E}$  is the union of these faces:

$$\partial\mathcal{E} = \bigcup_{\theta, \phi} \mathcal{F}(\theta, \phi). \quad (12)$$

Since  $\mathcal{E}$  is a compact and convex set,  $\mathcal{F}$  is also a compact and convex set, and the set of all extreme points

$$\text{ext}(\mathcal{E}) = \bigcup_{\theta, \phi} \text{ext}(\mathcal{F}(\theta, \phi)). \quad (13)$$

For more details on the supporting hyperplane and the faces, we point to [33].

Corresponding to the biggest eigenvalue  $\lambda_M(\theta, \phi)$  of  $\Lambda(\theta, \phi)$ , let us denote the eigenspace by  $\mathcal{E}(\theta, \phi) \subseteq \mathcal{H}_d$  and an eigenket by  $|\theta, \phi\rangle_k$ . Note that every ket in the whole paper represents a normalized vector. At a particular  $(\theta, \phi)$  if  $\lambda_M$  is degenerate (that is, the dimension of  $\mathcal{E}$  is more than 1) then we generally use a subscript  $k$  to differentiate eigenkets. All the maximum-eigenvalue-states—which are  $\{|\theta, \phi\rangle_k \langle \theta, \phi|\}$  and all their convex combinations (mixtures)—saturate inequality (10) and generate the whole face in (11):

$$\mathcal{F}(\theta, \phi) = \text{Conv} \{ \langle \theta, \phi | \vec{E} | \theta, \phi \rangle \mid |\theta, \phi\rangle \in \mathcal{E}(\theta, \phi) \}. \quad (14)$$

If a face only has one point—that certainly occurs when  $\lambda_m$  is nondegenerate and may even occur in a degenerate case [for example, see Sec. V]—then it is called an *exposed*-extreme point. Degeneracy is a necessary but not sufficient requirement for a face to have more than one distinct points.

In conclusion, we exploit (10) and (14) for all  $\theta \in [0, \pi]$  and  $\phi \in [0, 2\pi]$  to completely specify—the allowed region through its boundary— $\partial\mathcal{E}$ . With  $\mathcal{E}$  one can provide a definite yes/no answer to the question asked at the beginning of Introduction. Note that (10) represents a single necessary condition, but once we take (10) for all  $\theta$ 's and  $\phi$ 's then they will be sufficient. Necessary and sufficient restrictions on the mean vector  $\vec{\epsilon}$  are collectively called as the *quantum contains* (QCs) in [15].

*A side remark:* If each operator in  $\vec{E}' = (\Gamma_1, \dots, \Gamma_\kappa)$  is a real linear sum,  $\Gamma_k = T_{kx}X + T_{ky}Y + T_{kz}Z$ , of the operators in  $\vec{E}$  then the allowed region  $\mathcal{E}'$  for  $\vec{E}'$  can be obtained directly from  $\mathcal{E}$  by the  $\kappa \times 3$  real matrix  $T$ . As an example, through the orthogonal projection  $\vec{E} \mapsto (X, Y, 0) = \vec{E}'$  one can have the allowed region for  $X$  and  $Y$  from  $\mathcal{E}$ . Another example, if  $T$  is an orthogonal matrix on  $\mathbb{R}^3$ , then  $\mathcal{E}$  can be turned into  $\mathcal{E}'$  by a composition of a rotation and at most one reflection.

When an operator  $X$  has more than two distinct outcomes (eigenvalues), then we need two *independent* real numbers,  $\langle X \rangle$  and  $\langle X^2 \rangle$ , to characterize uncertainty,  $\Delta X = \sqrt{\langle X^2 \rangle - \langle X \rangle^2}$ , about its measurement-outcomes. In the case of Shannon entropy  $H(\vec{p}) = -\sum_{l=1}^d p_l \ln p_l$ , we require  $d-1$  real numbers from  $\vec{p} = (p_1, \dots, p_d)$ , where  $p_l$  is the probability of getting  $l$ th outcome in a measurement for  $X$ . If  $X$  has a degenerate eigenvalue such as in the following sections, then there exist infinitely-many distinct projective measurements for  $X$ , and thus there is no unique probability vector  $\vec{p}$  and the Shannon entropy  $H(\vec{p})$ . However, the mean values  $\langle X \rangle$ ,  $\langle X^2 \rangle$ , and thus the standard deviation  $\Delta X$  are the same for every measurement for  $X$ .

Now suppose we only have the mean value  $\langle X \rangle$ , and we want to quantify uncertainty—about the outcomes of  $X$ —using it. In this situation, we can build uncertainty and certainty measures as described in [15]: For an operator  $X$ , provided  $x_m \neq x_M$ , first we construct two positive semi-definite operators

$$\dot{X} := \frac{x_M I - X}{x_M - x_m} \quad \text{and} \quad \ddot{X} := \frac{X - x_m I}{x_M - x_m} \quad (15)$$

such that  $\dot{X} + \ddot{X}$  is the identity operator  $I$ . Both  $\langle \dot{X} \rangle, \langle \ddot{X} \rangle \in [0, 1]$  are functions of  $\langle X \rangle \in [x_m, x_M]$  only. Then we define certain concave and convex functions of  $\langle X \rangle$

$$h(\langle X \rangle) := -(\langle \dot{X} \rangle \ln \langle \dot{X} \rangle + \langle \ddot{X} \rangle \ln \langle \ddot{X} \rangle), \quad (16)$$

$$u_\kappa(\langle X \rangle) := \langle \dot{X} \rangle^\kappa + \langle \ddot{X} \rangle^\kappa, \quad 0 < \kappa < \infty, \quad \text{and} \quad (17)$$

$$u_{\max}(\langle X \rangle) := \max \{ \langle \dot{X} \rangle, \langle \ddot{X} \rangle \}. \quad (18)$$

The concave functions  $h \in [0, \ln 2]$  and  $u_\kappa \in [1, 2^{1-\kappa}]$  for  $0 < \kappa < 1$  can be treated as uncertainty measures, and

the convex functions  $u_\kappa \in [2^{1-\kappa}, 1]$  for  $1 < \kappa < \infty$  and  $u_{\max} \in [\frac{1}{2}, 1]$  will be certainty measures.

Note that, like the standard deviation  $\Delta X$  and Shannon entropy  $H(\vec{p})$ , the above uncertainty measures do not reach their minimum values when the system is in an eigenstate of  $X$  unless the state corresponds to an extreme eigenvalue  $x_m$  or  $x_M$ . Naturally, if one can access only the mean value then she can be certain only in the two situations  $\langle X \rangle = x_m$  and  $\langle X \rangle = x_M$ . So, (16)–(18) are (un)certainty measures about the outcomes of  $X$  given only the mean value  $\langle X \rangle$ , not the state  $\rho$ , and they are different from  $\Delta X$  and  $H(\vec{p})$  particularly when  $X$  has more than two distinct outcomes.

Since the addition of concave functions is also a concave function, for example,

$$u_{1/2}(\vec{\epsilon}) := u_{1/2}(\langle X \rangle) + u_{1/2}(\langle Y \rangle) + u_{1/2}(\langle Z \rangle) \quad (19)$$

acts as a combined uncertainty measure on the compact and convex set  $\mathcal{E}$ . Its global minimum will be at  $\text{ext}(\mathcal{E}) \subseteq \partial\mathcal{E}$  [see (12)–(14)]. Suppose  $u_{1/2}(\vec{\epsilon})$  reaches its absolute minimum, symbolized by  $u_{1/2}$ , at some  $\theta$  and  $\phi$ , then the tight UR  $u_{1/2} \leq u_{1/2}(\vec{\epsilon})$  is saturated by a subset of kets in the eigenspace  $\mathcal{E}(\theta, \phi)$ . For every UR based on the above formulation, its minimum uncertainty kets always lie in

$$\bigcup_{\theta, \phi} \mathcal{E}(\theta, \phi). \quad (20)$$

In the same way, one can reach the global maximum of a convex function (combined certainty measure) and then enjoy a tight CR with its maximum certainty kets in (20).

By replacing the average vector  $\vec{\epsilon} = (\langle X \rangle, \langle Y \rangle, \langle Z \rangle)$  with  $\vec{r} = (x, y, z)$  in the tight UR  $u_{1/2} \leq u_{1/2}(\vec{\epsilon})$ , one can specify a region

$$\mathcal{R}_{u_{1/2}} := \{ \vec{r} \in \mathcal{H} \mid u_{1/2} \leq u_{1/2}(\vec{r}) \}, \quad (21)$$

in hyperrectangle (3).  $\mathcal{R}$ —bounded by a UR or CR—is a convex set in the space of expectation values. Obviously  $\mathcal{R}$  contains the allowed region  $\mathcal{E}$ , and there exists no quantum state  $\rho$  for any point outside  $\mathcal{E}$ , for instance, in the relative complement  $\mathcal{R} \setminus \mathcal{E}$ . The boundary  $\partial\mathcal{E}$  touches the boundary  $\partial\mathcal{R}_{u_{1/2}}$  at those points that come from the minimum uncertainty states associated with the UR [for example, see Fig. 1].

An uncertainty measure such as  $u_{1/2}(\vec{\epsilon})$  reaches its trivial lower bound 3—which is just the sum of individual lower bounds of  $u_{1/2}(\langle X \rangle)$ ,  $u_{1/2}(\langle Y \rangle)$ , and  $u_{1/2}(\langle Z \rangle)$ —if and only if a vertex  $(x_{m,M}, y_{m,M}, z_{m,M})$  of  $\mathcal{H}$  lies in the numerical range  $\mathcal{E}$ . This will happen when there exist a common eigenket  $|e\rangle$  that corresponds to an extreme eigenvalue of every operator in  $\vec{E} = (X, Y, Z)$ . It can also happen in a limiting case where  $\mathcal{E}$  shares a few corners of  $\mathcal{H}$  in a limit, say,  $j \rightarrow \infty$  [see Secs. V, VII, and VIII]. In such cases, all URs and CRs based on (15)–(19) will become trivial, and their regions  $\mathcal{R} = \mathcal{H}$ .

Since the standard deviation  $\Delta$  and  $h$  of (16) are different functions, URs based on them are difficult to compare. Nevertheless, suppose both  $\delta \leq \Delta X + \Delta Y$  and

$\mathfrak{h} \leq h(\langle X \rangle) + h(\langle Y \rangle)$  are *tight* URs for the two non-commuting operators  $X$  and  $Y$ , where  $\delta \geq 0$  and  $\mathfrak{h} \geq 0$  depend on the operators but not on the state  $\rho$ . If and only if  $\delta = 0$  then there exists a state (common eigenstate) where both  $X$  and  $Y$  have no spread in their measurement-outcomes. We cannot make such a statement regarding  $\mathfrak{h}$  because there can be a situation [see Sec. V] where  $X$  and  $Y$  share a common eigenket ( $\delta = 0$ ) but it does not correspond to their extreme eigenvalues ( $\mathfrak{h} > 0$ ). So  $\mathfrak{h} = 0$  implies  $\delta = 0$  but not vice versa. Clearly our URs and CRs based on (15)–(19) are different from the URs based on the standard deviation [1, 13, 25–27, 34] and on the Shannon entropy [24, 28, 35].

### III. ANGULAR MOMENTUM OPERATORS

One can describe the three angular momentum operators

$$J_x = \frac{1}{2}(J_+ + J_-), \quad J_y = \frac{1}{2i}(J_+ - J_-), \quad \text{and} \quad J_z \quad (22)$$

as

$$J_{\pm} |m\rangle = \sqrt{(j \mp m)(j \pm m + 1)} |m \pm 1\rangle \quad \text{and} \quad (23)$$

$$J_z |m\rangle = m |m\rangle, \quad (24)$$

where  $i = \sqrt{-1}$ ,

$$\mathfrak{B}_z = \{ |m\rangle \mid m = j, j-1, \dots, -j+1, -j \} \quad (25)$$

is an eigenbasis of  $J_z$ , and  $j$  can be  $\frac{1}{2}, 1, \frac{3}{2}, 2, \dots$ . In the paper, every operator is dimensionless, and each ket is represented in the basis  $\mathfrak{B}_z$ . As the quantum number  $m$  can only acquire  $2j+1$  discrete values for a fixed  $j$ , here our system of interest is of  $d = 2j+1$  levels.

To obtain the permissible region  $\mathcal{E}$  for  $\vec{J} = (J_x, J_y, J_z)$ , we begin with

$$\begin{pmatrix} J'_x \\ J'_y \\ J'_z \end{pmatrix} = \begin{pmatrix} \cos \theta \cos \phi & \cos \theta \sin \phi & -\sin \theta \\ -\sin \phi & \cos \phi & 0 \\ \sin \theta \cos \phi & \sin \theta \sin \phi & \cos \theta \end{pmatrix} \begin{pmatrix} J_x \\ J_y \\ J_z \end{pmatrix}. \quad (26)$$

One can show that the components of  $\vec{J}' = (J'_x, J'_y, J'_z)$  follow the same commutation relations that  $J_x, J_y$ , and  $J_z$  obey, for example,  $J_x J_y - J_y J_x = i J_z$ . Hence,  $J'_x, J'_y$ , and  $J'_z$  are also angular momentum operators, and their spectrum  $j, \dots, -j$  is independent of  $\theta$  and  $\phi$ .

In fact,  $J'_z$  is our  $\Lambda(\theta, \phi)$  here, and the angular momentum coherent state-vector [36, 37]

$$|\theta, \phi\rangle = \sum_{m=-j}^j \sqrt{\frac{(2j)!}{(j+m)!(j-m)!}} \left(\cos \frac{\theta}{2}\right)^{j+m} \left(\sin \frac{\theta}{2}\right)^{j-m} e^{-im\phi} |m\rangle \quad (27)$$

is its eigenket corresponding to  $\lambda_M = j$ . Furthermore,

$$\langle \theta, \phi | \vec{J} | \theta, \phi \rangle = j \hat{\eta}(\theta, \phi) \quad (28)$$

generate the boundary of  $\mathcal{E}$ , which is a closed ball classified by

$$\langle J_x \rangle^2 + \langle J_y \rangle^2 + \langle J_z \rangle^2 \leq j^2. \quad (29)$$

Here every face  $\mathcal{F}(\theta, \phi)$  of  $\mathcal{E}$  [see (14)] is made of a single exposed-extreme point (28). For the three momentum observables, URs based on the standard deviation and entropy are achieved in [24–28]. While in [15], tight URs and CRs based on (15)–(19) are derived by employing QC (29), where a maximum-certainty or minimum-uncertainty ket is a coherent ket (27).

### IV. POWERS OF LADDER OPERATORS

The ladder operators  $J_{\pm}$  [see (23)] are non-Hermitian operators such that  $J_{\pm}^\dagger = J_{\mp}$ , whereas

$$\Lambda_\gamma(\phi) = e^{i\phi} J_+^\gamma + e^{-i\phi} J_-^\gamma = \cos \phi X_\gamma + \sin \phi Y_\gamma, \quad (30)$$

$$X_\gamma = (J_+^\gamma + J_-^\gamma), \quad \text{and} \quad Y_\gamma = i(J_+^\gamma - J_-^\gamma) \quad (31)$$

are Hermitian operators for every angle  $\phi \in [0, 2\pi)$  and the power  $\gamma = 1, \dots, d$ . For  $\gamma = 1$ ,  $X_\gamma = 2J_x$  and  $Y_\gamma = -2J_y$ , and they are the null operator when  $\gamma = d$ .

It is known due to [16, 17] that the characteristic equation of an operator, say,  $\Lambda$  on a  $d$ -dimensional space is

$$\sum_{l=0}^d (-1)^l S_l \lambda^{d-l} = 0, \quad (32)$$

where

$$S_0 = 1, \quad S_1 = \text{tr}(\Lambda), \quad \text{and} \quad (33)$$

$$S_l = \frac{1}{l!} \sum_{i=1}^l (-1)^{i-1} \text{tr}(\Lambda^i) S_{l-i} \quad (34)$$

are the symmetric functions of its eigenvalues. By showing that  $\text{tr}(\Lambda^i)$  is independent of  $\phi$  for every  $i = 1, \dots, d$ , one can certify that  $S_l$  ( $l = 1, \dots, d$ ), characteristic equation (32), and all the eigenvalues of  $\Lambda_\gamma(\phi)$  are also independent of  $\phi$ . As a result, inequalities (8) and (10) here become

$$-\lambda_M \leq \cos \phi \langle X_\gamma \rangle + \sin \phi \langle Y_\gamma \rangle \leq \lambda_M, \quad (35)$$

where  $\lambda_M$  is the largest eigenvalue of  $X_\gamma$  (and of  $Y_\gamma$ ) for a given  $\gamma$ ; see Table I. Inequalities (35) tell that the average value of  $\Lambda_\gamma(\phi)$  must be in a fixed interval  $[-\lambda_M, \lambda_M]$  in every direction  $\phi$ , which implies

$$\vec{\varepsilon}' \cdot \vec{\varepsilon}' \leq \lambda_M^2 \quad (36)$$

for  $\vec{\varepsilon}' = (\langle X_\gamma \rangle, \langle Y_\gamma \rangle)$ . Hence, the allowed region  $\mathcal{E}$  of the mean vectors is the closed disk bounded by QC (36). By the same reasoning: whenever  $\lambda_M(\theta, \phi)$  is the same for all the angles  $\theta$ 's and  $\phi$ 's, then  $\mathcal{E}$  is enclosed by a sphere of radius  $\lambda_M$  centered at the origin [for instance, see (29), (36), (89), and (103)].

TABLE I. For  $\gamma = 2, 3$ , and 4, the greatest eigenvalues  $\lambda_M$  of  $\Lambda_\gamma(\phi)$  [of (30)] corresponding to different  $j$ -values are listed in the three columns on the right-hand-side. Since the spectrum of  $\Lambda_\gamma(\phi)$  does not depend on  $\phi$ ,  $\lambda_M$  is also an extreme eigenvalue of  $X_\gamma$  as well as of  $Y_\gamma$ . The associated eigenkets  $|\phi\rangle_k$  are arranged in Tables IV and V in Appendix .

$j$	for $\gamma = 2$	for $\gamma = 3$	for $\gamma = 4$
$\frac{1}{2}$	0	0	0
1	2	0	0
$\frac{3}{2}$	$2\sqrt{3}$	6	0
2	$4\sqrt{3}$	12	24
$\frac{5}{2}$	$4\sqrt{7}$	24	$24\sqrt{5}$
3	$2(3 + 2\sqrt{6})$	$12\sqrt{10}$	120
$\frac{7}{2}$	$2\sqrt{3(21 + 4\sqrt{21})}$	$6\sqrt{115}$	$120\sqrt{3}$
4	$8\sqrt{13}$	$12\sqrt{70}$	360

Since  $J_\pm^\gamma |m\rangle$  is directly proportional to  $|m \pm \gamma\rangle$ , we can divide basis (25) into  $\gamma$  number of disjoint subsets in such a way that the linear span of a subset delivers an invariant subspace

$$\mathcal{S}_k^\gamma := \text{span}\{|j - k\rangle, |j - k - \gamma\rangle, |j - k - 2\gamma\rangle, \dots\} \quad (37)$$

of  $J_\pm^\gamma$  and thus of  $\Lambda_\gamma(\phi)$ . So, one can search eigenvector(s)  $|\phi\rangle$  associated with  $\lambda_M$  of  $\Lambda_\gamma(\phi)$  in these subspaces rather than in the whole Hilbert space  $\mathcal{H}_d = \bigoplus_{k=0}^{\gamma-1} \mathcal{S}_k^\gamma$ , where  $\bigoplus$  symbolizes the direct sum. In Appendix , Tables IV and V carry these eigenkets for  $\gamma = 2, 3$ , and 4. When  $\lambda_M$  is twofold degenerate then two orthonormal eigenkets  $|\phi\rangle_k$  and  $|\phi\rangle_{k'}$  are registered in the tables, where the subscript  $k$  illustrates  $|\phi\rangle_k \in \mathcal{S}_k^\gamma$ .

In the case of double-degeneracy, a general eigenket will be a superposition

$$|\phi\rangle = \cos \mu |\phi\rangle_k + \sin \mu e^{i\nu} |\phi\rangle_{k'} \in \mathcal{E}(\phi), \quad (38)$$

where  $\mathcal{E}(\phi)$  is the eigenspace,  $\mu \in [0, \frac{\pi}{2}]$ , and  $\nu \in [0, 2\pi)$ . When we compute  $\langle \phi | X_\gamma | \phi \rangle$  using (38), then we encounter cross-terms such as  ${}_k \langle \phi | X_\gamma | \phi \rangle_{k'}$  that all will be zero here. It is because  $X_\gamma |\phi\rangle_{k'}$  and  $|\phi\rangle_k$  lie in mutually orthogonal invariant subspaces  $\mathcal{S}_{k'}^\gamma$  and  $\mathcal{S}_k^\gamma$ , respectively, of  $X_\gamma$ . Therefore, every  $\langle \phi | \vec{E} | \phi \rangle$  will fall on a line segment connecting the two extreme points

$${}_k \langle \phi | \vec{E} | \phi \rangle_k \quad \text{and} \quad {}_{k'} \langle \phi | \vec{E} | \phi \rangle_{k'}; \quad (39)$$

$\vec{E} = (X_\gamma, Y_\gamma)$  in this section. The line segment forms a face  $\mathcal{F}(\phi)$  [as per (14)] of the permitted region  $\mathcal{E}$ . If the degree of degeneracy is three, then  $\mathcal{F}(\phi)$  will be the convex hull of three extreme points such as (39), and so on. Here, both points in (39) turn out to be the same, hence every eigenket associated with  $\lambda_M(\phi)$  produces a single extreme point

$$\langle \phi | \vec{E} | \phi \rangle = \lambda_M (\cos \phi, \sin \phi) = \lambda_M \hat{\eta}(\phi) \quad (40)$$

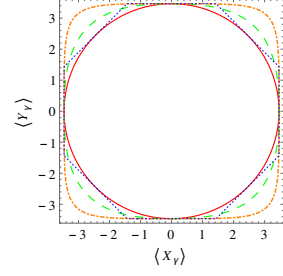


FIG. 1. (Color online) In the case  $j = \frac{3}{2}$  and  $\gamma = 2$ ,  $\lambda_M = 2\sqrt{3}$ , hyperrectangle (3) is the square  $[-\lambda_M, \lambda_M]^{\times 2}$ , and the regions  $\mathcal{R}$ 's are defined with respect to (21). The boundaries of regions  $\mathcal{R}_h, \mathcal{R}_{u_{1/2}}, \mathcal{R}_{u_2}$ , and  $\mathcal{R}_{u_{\max}}$  determined by (41)–(44) are depicted through the dashed, dot-dashed, solid, and dotted (green, orange, red, and blue) closed-curves. Here,  $\mathcal{R}_{u_2} = \mathcal{E}$ , which is clearly contained in all the other regions, and  $\mathcal{R}_h \subset \mathcal{R}_{u_{1/2}}$ .

of  $\mathcal{E}$ . Taking Tables I, IV, and V, one can verify (40). Indeed, points (40) saturate QC (36) and create the boundary  $\partial \mathcal{E}$ .

Now, following the procedure laid out at the end of Sec. II, we achieve tight relations

$$\ln 2 \leq h(\vec{\epsilon}) = h(\langle X_\gamma \rangle) + h(\langle Y_\gamma \rangle), \quad (41)$$

$$1 + \sqrt{2} \leq u_{1/2}(\vec{\epsilon}), \quad (42)$$

$$u_2(\vec{\epsilon}) \leq \frac{3}{2}, \quad \text{and} \quad (43)$$

$$u_{\max}(\vec{\epsilon}) \leq \frac{1+\sqrt{2}}{\sqrt{2}}, \quad (44)$$

which hold in every dimension  $d \geq 2$  and for every power  $1 \leq \gamma < d$ . At boundary points (40), both  $h(\langle \phi | \vec{E} | \phi \rangle)$  and  $u_{1/2}(\langle \phi | \vec{E} | \phi \rangle)$  hit their global minima given in (41) and (42), respectively, at  $\phi = 0, \frac{\pi}{2}, \pi, \frac{3\pi}{2}$ . Hence, for both the URs, minimum uncertainty states are the eigenstates of  $\{X_\gamma, Y_\gamma\}$  corresponding to  $\pm \lambda_M$ . Similarly,  $u_{\max}(\langle \phi | \vec{E} | \phi \rangle)$  reaches its absolute maximum at  $\phi = \frac{\pi}{4}, \frac{3\pi}{4}, \frac{5\pi}{4}, \frac{7\pi}{4}$ , thus CR (44) is saturated by the extreme-eigenvalue-states of  $\frac{1}{\sqrt{2}}(X_\gamma \pm Y_\gamma)$ . Whereas CR (43) is the same as QC (36), therefore it is *optimal* in the sense [15] that it provides the smallest region  $\mathcal{R}_{u_2} = \mathcal{E}$  as shown in Fig. 1. Furthermore, (43) is saturated by  $|\phi\rangle \langle \phi|$  for all  $\phi \in [0, 2\pi)$ .

## V. SQUARE OF ANGULAR MOMENTUM OPERATORS

Squared angular momentum operators obey

$$J_x^2 + J_y^2 + J_z^2 = j(j+1)I, \quad (45)$$

hence we get only two independent real numbers out of the three  $\langle J_x^2 \rangle$ ,  $\langle J_y^2 \rangle$ , and  $\langle J_z^2 \rangle$ . So, in this section, we present the allowed region  $\mathcal{E}$  for  $\vec{E} = (J_x^2, J_y^2)$  and  $j = \frac{1}{2}, \dots, 4$ , and  $\infty$  by taking

$$\Lambda(\phi) = \cos \phi J_x^2 + \sin \phi J_y^2 = \hat{\eta}(\phi) \cdot \vec{E} \quad (46)$$

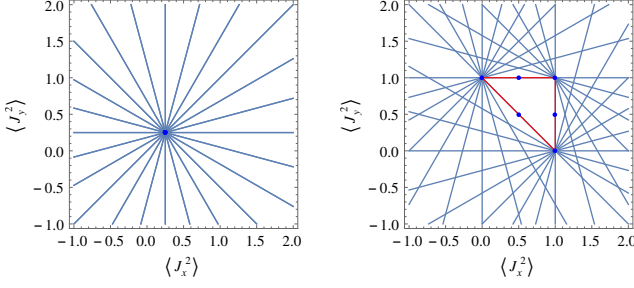


FIG. 2. (Color online) For  $j = \frac{1}{2}$  and 1, the permitted regions  $\mathcal{E}$  of  $(\langle J_x^2 \rangle, \langle J_y^2 \rangle)$  are—exhibited in the left- and right-hand-side pictures—the single point  $(\frac{1}{4}, \frac{1}{4})$  and the triangle whose boundary is shown in red color, respectively. The blue lines are the supporting hyperplanes (9) of  $\mathcal{E}$  at  $\phi = 0, \frac{2\pi}{24}, \dots, 23\frac{2\pi}{24}$ .

according to (5). Here hyperrectangle (3) is the square

$$[\frac{1}{4}, j^2]^{\times 2} \quad \text{or} \quad [0, j^2]^{\times 2}, \quad \text{and} \quad (47)$$

$$J_i^2 = \frac{I - \frac{J_i^2}{j^2}}{1 - \frac{1}{4j^2}} \quad \text{or} \quad J_i^2 = I - \frac{J_i^2}{j^2} \quad (i = x, y) \quad (48)$$

for a half-integer or an integer  $j$ . The operator  $J_i^2$  is constructed with respect to (15).

In the case of  $j = \frac{1}{2}$ ,  $J_x^2 = J_y^2 = \frac{1}{4}I$ , thus  $\mathcal{E}$  is just the single point  $(\frac{1}{4}, \frac{1}{4})$  exhibited in Fig. 2. For  $j > \frac{1}{2}$ ,  $J_x^2$ ,  $J_y^2$ , and their linear combinations (46) have two mutually orthogonal invariant subspaces  $\mathcal{S}_0^2$  and  $\mathcal{S}_1^2$  [defined in (37)] such that  $\mathcal{S}_0^2 \oplus \mathcal{S}_1^2 = \mathcal{H}_d$ . Like the previous section, we shall look for eigenkets of  $\Lambda(\phi)$  in the subspaces for a given  $j = \frac{d-1}{2}$ .

For  $j = 1$ ,  $J_x^2$  and  $J_y^2$  are rank-2 projectors that commute with each other, and their common eigenbasis is the union of

$$|e_{1,3}\rangle = \frac{1}{\sqrt{2}}(|+1\rangle \pm |-1\rangle) \in \mathcal{S}_0^2 \quad \text{and} \quad |e_2\rangle = |0\rangle \in \mathcal{S}_1^2. \quad (49)$$

In this case,  $\mathcal{E}$  is the convex hull of three points  $(1, 0)$ ,  $(1, 1)$ , and  $(0, 1)$  as per (4). It means that  $\mathcal{E}$  is a triangle displayed in Fig. 2. The maximum eigenvalue

$$\lambda_M(\phi) = \max\{\cos\phi, \sin\phi, \cos\phi + \sin\phi\} \quad (50)$$

of  $\Lambda(\phi)$  becomes twofold degenerate at  $\phi = 0, \frac{\pi}{2}$ , and  $\frac{5\pi}{4}$ . Sides of the triangle are in fact three faces  $\mathcal{F}(\phi)$  of  $\mathcal{E}$  at these angles, that is, they are produced by the maximum-eigenvalue-states of  $J_x^2$ ,  $J_y^2$ , and  $J_z^2$ . One can realize that

$$\Lambda(\frac{5\pi}{4}) = \frac{1}{\sqrt{2}}[J_z^2 - j(j+1)I] = -\Lambda(\frac{\pi}{4}) \quad (51)$$

through (45) and (46). As  $J_x^2$  and  $J_y^2$  commute in the case of  $j = \frac{1}{2}, 1$ , a UR or CR for them will be a trivial inequality.

For  $j > 1$ , the maximum-eigenvalue-states of  $J_x^2$ ,  $J_y^2$ , and  $J_z^2$  yield three separate extreme points

$$(j^2, \frac{j}{2}), \quad (\frac{j}{2}, j^2), \quad \text{and} \quad (\frac{j}{2}, \frac{j}{2}) \quad (52)$$

of  $\mathcal{E}$ , respectively. Whereas eigenstates related to the minimum characteristic value  $\frac{1}{4}$  or 0 of  $J_x^2$ ,  $J_y^2$ , and  $J_z^2$  provide the extreme points

$$(\frac{1}{4}, \frac{j(j+1)}{2} - \frac{1}{8}), (\frac{j(j+1)}{2} - \frac{1}{8}, \frac{1}{4}), \quad \text{and} \quad (\frac{j(j+1)}{2} - \frac{1}{8}, \frac{j(j+1)}{2} - \frac{1}{8}) \quad (53)$$

for a half-integer  $j$  and

$$(0, \frac{j(j+1)}{2}), \quad (\frac{j(j+1)}{2}, 0), \quad \text{and} \quad (\frac{j(j+1)}{2}, \frac{j(j+1)}{2}) \quad (54)$$

for an integer  $j$ , respectively. These points are illustrated by blue dots in Figs. 2–5.

In the following, we present the eigenvalue  $\lambda_M(\phi)$  of  $\Lambda(\phi)$  [given in (46)], the corresponding eigenkets  $|\phi\rangle$ , and the expectation values  $\langle\phi|J_x^2|\phi\rangle$  and  $\langle\phi|J_y^2|\phi\rangle$  in that order for quantum numbers  $j = \frac{3}{2}, \dots, 4$ .  $\lambda_M(\phi)$  is expressed in terms of

$$f(\phi), g(\phi) = \cos\phi \pm \sin\phi \quad \text{for all} \quad \phi \in [0, 2\pi). \quad (55)$$

In the case of half-integer  $j = \frac{3}{2}, \frac{5}{2}, \frac{7}{2}$ ,  $\lambda_M$  is twofold degenerate at every  $\phi$ , hence two eigenkets  $|\phi\rangle_{0,1} \in \mathcal{S}_{0,1}^2$  are provided. Both  $|\phi\rangle_{0,1}$  produce a single extreme point of  $\mathcal{E}$ . As the two kets belong to mutually orthogonal invariant subspaces of  $J_x^2$  and  $J_y^2$ , all their normalized linear combinations [see (38) and the text around it] will also deliver the same point  $\langle\phi|\vec{E}|\phi\rangle$ . In the case of  $j = 2, 3, 4$ ,  $\lambda_M$  is twofold degenerate only at  $\phi = 0, \frac{\pi}{2}$ , and  $\frac{5\pi}{4}$ , and the corresponding extreme points are already registered in (52). So, for an integer  $j$ , only one eigenket is presented below.

For every  $j = \frac{3}{2}, \dots, 4$ , the maximum-eigenvalue-kets  $|\phi\rangle$  are stated in terms of coefficients  $\alpha, \beta, \varsigma$  that are real functions of the parameter  $\phi$ . As all these coefficients become zero or indeterminate at  $\phi = \frac{5\pi}{4}$ , none of the formulas supplied below for  $|\phi\rangle$ , and thus for  $\langle\phi|\vec{E}|\phi\rangle$  are applicable at that angle. With (51), we can directly realize  $|\phi = \frac{5\pi}{4}\rangle = |\pm j\rangle$ , and  $\langle\pm j|\vec{E}|\pm j\rangle = (\frac{j}{2}, \frac{j}{2})$  is already listed in (52).

For  $j = \frac{3}{2}, \dots, 4$ , the boundary  $\partial\mathcal{E}$  is represented graphically in Figs. 3–5 by the (red) closed-curves and parametrically by  $\langle\phi|\vec{E}|\phi\rangle$ . In Figs. 2–5, the supporting hyperplanes  $\mathbb{H}(\phi)$  [defined in (9)] at equally spaced angles  $\phi = k\frac{2\pi}{24}$ ,  $k = 0, \dots, 23$ , are depicted by the (blue) lines. One can observe that each hyperplane touches  $\mathcal{E}$  only at one point when  $j > 1$ , which implies that each face  $\mathcal{F}(\phi)$  [defined in (11)] is then made of a single extreme point, and  $\text{ext}(\mathcal{E}) = \partial\mathcal{E}$ .

Now let us start with  $j = \frac{3}{2}$ , where the maximum eigenvalue of  $\Lambda(\phi)$  is

$$\lambda_M(\phi) = \frac{1}{4}(5f + 2\sqrt{f^2 + 3g^2}) \quad \text{for all} \quad \phi \in [0, 2\pi) \quad (56)$$

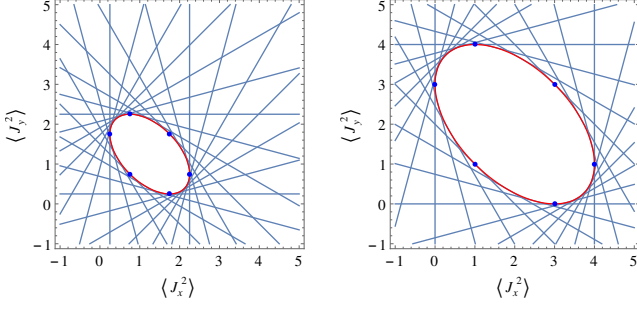


FIG. 3. (Color online) The left and right red ellipses with their interiors represent the allowed region  $\mathcal{E}$  of  $\vec{\epsilon} = (\langle J_x^2 \rangle, \langle J_y^2 \rangle)$  in the case of  $j = \frac{3}{2}$  and  $j = 2$ , respectively. The points (1, 1), (4, 1), and (1, 4) on the right-hand-side ellipse come from the common eigenkets  $|\mathbf{e}_1\rangle$ ,  $|\mathbf{e}_2\rangle$ , and  $|\mathbf{e}_3\rangle$ , respectively, given in (64).

[for  $f, g$  see (55)]. Two mutually orthogonal eigenkets associated with  $\lambda_M$  are

$$\begin{aligned} |\phi\rangle_0 &= \frac{1}{\sqrt{\alpha^2 + \beta^2}} (\alpha |+\frac{3}{2}\rangle + \beta |-\frac{1}{2}\rangle) \in \mathcal{S}_0^2 \text{ and} \\ |\phi\rangle_1 &= \frac{1}{\sqrt{\alpha^2 + \beta^2}} (\beta |+\frac{1}{2}\rangle + \alpha |-\frac{3}{2}\rangle) \in \mathcal{S}_1^2, \text{ where} \\ \alpha(\phi) &= 2\sqrt{3}g \text{ and } \beta(\phi) = 4\lambda_M - 3f. \end{aligned} \quad (57)$$

One can show that both  $|\phi\rangle_{0,1}$  and all their superpositions contribute a single extreme point

$$\begin{aligned} \langle \phi | J_x^2 | \phi \rangle &= \frac{3\alpha^2 + 4\sqrt{3}\alpha\beta + 7\beta^2}{4(\alpha^2 + \beta^2)}, \\ \langle \phi | J_y^2 | \phi \rangle &= \frac{3\alpha^2 - 4\sqrt{3}\alpha\beta + 7\beta^2}{4(\alpha^2 + \beta^2)} \end{aligned} \quad (58)$$

of  $\mathcal{E}$ . The boundary  $\partial\mathcal{E}$ —characterized by its parametric form (58)—is an ellipse [see Fig. 3]. The QC

$$(\langle J_x^2 \rangle + \langle J_y^2 \rangle - \frac{5}{2})^2 + \frac{(\langle J_x^2 \rangle - \langle J_y^2 \rangle)^2}{3} \leq 1 \quad (59)$$

completely identifies the permitted region here, and the inequality is saturated by the maximum-eigenvalue-states of  $\Lambda(\phi)$  for all  $\phi$ 's. The equality in (59) describes the ellipse.

Next we pick  $j = 2$ , where the largest characteristic value of  $\Lambda(\phi)$  is

$$\lambda_M(\phi) = 2f + \sqrt{f^2 + 3g^2} \text{ for all } 0 \leq \phi < 2\pi. \quad (60)$$

For an angle  $\phi$  other than  $0, \frac{\pi}{2}$ , and  $\frac{5\pi}{4}$ ,  $\lambda_M$  is non-degenerate, and thus we have only one largest-eigenvalue-ket

$$\begin{aligned} |\phi\rangle_0 &= \frac{1}{\sqrt{2\alpha^2 + \beta^2}} (\alpha | +2 \rangle + \beta | 0 \rangle + \alpha | -2 \rangle) \in \mathcal{S}_0^2, \\ \alpha(\phi) &= \sqrt{6}g \text{ and } \beta(\phi) = 2(\lambda_M - f). \end{aligned} \quad (61)$$

These kets generate the borderline

$$\langle \phi | \vec{E} | \phi \rangle = \left( \frac{2\alpha^2 + 2\sqrt{6}\alpha\beta + 3\beta^2}{2\alpha^2 + \beta^2}, \frac{2\alpha^2 - 2\sqrt{6}\alpha\beta + 3\beta^2}{2\alpha^2 + \beta^2} \right) \quad (62)$$

of  $\mathcal{E}$ , which is the other ellipse displayed in Fig. 3. All the pure states  $|\phi\rangle_0 \langle \phi|$  made of (61) saturate QC

$$\frac{(\langle J_x^2 \rangle + \langle J_y^2 \rangle - 4)^2}{4} + \frac{(\langle J_x^2 \rangle - \langle J_y^2 \rangle)^2}{12} \leq 1. \quad (63)$$

That is to say that points (62) follow the equality in (63). And, the same is true for the three extreme points in (52).

Before formulating a set of tight URs and CRs for  $j = 2$  by following the procedure described in the last part of Sec. II, let us first note that operators  $J_x^2, J_y^2$  and thus all their linear sums (46) possess three common orthogonal eigenkets

$$\begin{aligned} |\mathbf{e}_1\rangle &= \frac{1}{\sqrt{2}} (|+2\rangle - |-2\rangle) \in \mathcal{S}_0^2 \subset \mathcal{H}_5, \\ |\mathbf{e}_2\rangle &= \frac{1}{\sqrt{2}} (|+1\rangle + |-1\rangle) \in \mathcal{S}_1^2 \subset \mathcal{H}_5, \text{ and} \\ |\mathbf{e}_3\rangle &= \frac{1}{\sqrt{2}} (|+1\rangle - |-1\rangle) \in \mathcal{S}_1^2 \subset \mathcal{H}_5. \end{aligned} \quad (64)$$

Now, taking (16)–(19) with (48), we combine uncertainty or certainty measures for  $\vec{\epsilon} = (\langle J_x^2 \rangle, \langle J_y^2 \rangle)$  and obtain the tight relations

$$0 < 4 \ln 2 - \sqrt{3} \ln(2 + \sqrt{3}) \leq h(\vec{\epsilon}), \quad (65)$$

$$2 < \frac{1}{2}(3 + \sqrt{3}) \leq u_{1/2}(\vec{\epsilon}), \quad (66)$$

$$u_2(\vec{\epsilon}) \leq \frac{7}{4} < 2, \text{ and} \quad (67)$$

$$u_{\max}(\vec{\epsilon}) \leq 1 + \frac{\sqrt{3}}{2} < 2 \quad (68)$$

by finding the absolute minima of concave and maxima of convex functions on  $\partial\mathcal{E}$  in (62). Relations (65), (67), and (68) are saturated by  $\phi$ -kets (61) at  $\phi = \frac{3\pi}{4}, \frac{7\pi}{4}$ . Whereas, the extreme-eigenvalue-states of  $J_x^2$  and  $J_y^2$  are the minimum uncertainty states for UR (66). By the way, we get the same relations (65)–(68) for  $j = \frac{3}{2}$ , and the states which saturate them will then be from (57).

In (65)–(68), the strict inequality signs ( $<$ ) represent the trivial lower or upper bounds. Clearly, we achieve *nontrivial* tight URs and CRs despite the non-commuting operators  $J_x^2$  and  $J_y^2$  share three eigenvectors (64). It is because the situation described in the last two paragraphs of Sec. II does not occur here. On the other hand, a UR based on the standard deviations of  $J_x^2$  and  $J_y^2$  will be a trivial one as  $\Delta J_x^2 = 0 = \Delta J_y^2$  when the system is in their common eigenstate.

As  $J_x^2$  is a degenerate operator, there exist infinitely-many distinct projective measurements for it, and similarly for  $J_y^2$ . If  $|\mathbf{e}_l\rangle\langle\mathbf{e}_l|$  is a part of both the measurements for  $J_x^2$  and  $J_y^2$ , then we also get a tight and trivial UR  $0 \leq H(\vec{p}) + H(\vec{q})$  based on the Shannon entropy, where  $\vec{p}$  and  $\vec{q}$  are the probability vectors associated with the two measurements. However, with a different choice of measurements, one can get a nontrivial entropic UR. Since all such measurements provide the same mean vector  $\vec{\epsilon} = (\langle J_x^2 \rangle, \langle J_y^2 \rangle)$ , the relation in (65)–(68) are independent of the measurement-settings used for  $J_x^2$  and  $J_y^2$ .

Now we move to  $j = \frac{5}{2}$ , where the biggest eigenvalue



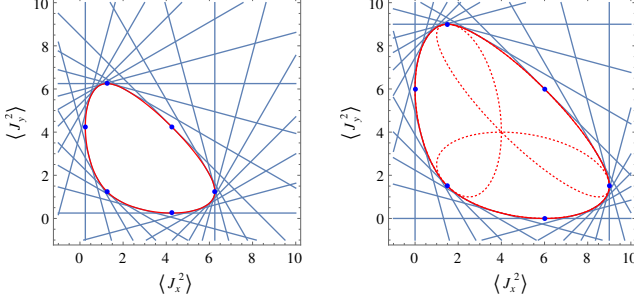


FIG. 4. (Color online) For  $j = \frac{5}{2}$  and  $j = 3$ , the boundary  $\partial\mathcal{E}$  of the joint numerical range of  $\vec{E} = (J_x^2, J_y^2)$  is exhibited by red solid-curves in the left- and right-hand-side panels. One can observe that  $\mathcal{E}$  for  $j = 3$  is the convex hull of three ellipses. A part of an ellipse that belongs to the boundary is shown by a solid-curve, and the remaining piece that falls inside  $\mathcal{E}$  is illustrated by a dotted-curve. The ellipses are centered at  $(5, 5)$ ,  $(2, 5)$ , and  $(5, 2)$  [see their Eqs. (77)].

of operator (46) is

$$\lambda_M(\phi) = \frac{1}{4} \left[ \frac{35f}{3} + 2\sqrt{\frac{p}{3}} \cos \left( \frac{1}{3} \arccos \left( \frac{-q}{2} \sqrt{\frac{27}{p^3}} \right) \right) \right],$$

$$p(\phi) = \frac{112}{3}(f^2 + 3g^2), \quad q(\phi) = \frac{1280}{27}(f^3 - 9fg^2), \quad (69)$$

for all  $0 \leq \phi < 2\pi$ . The two associated orthonormal eigenvectors are

$$|\phi\rangle_0 = \frac{1}{\sqrt{\alpha^2 + 1 + \beta^2}} (\alpha |+\frac{5}{2}\rangle + |+\frac{1}{2}\rangle + \beta |-\frac{3}{2}\rangle),$$

$$|\phi\rangle_1 = \frac{1}{\sqrt{\alpha^2 + 1 + \beta^2}} (\beta |+\frac{3}{2}\rangle + |-\frac{1}{2}\rangle + \alpha |-\frac{5}{2}\rangle), \quad (70)$$

$$\text{where } \alpha(\phi) = \frac{2\sqrt{10}g}{4\lambda_M - 5f} \quad \text{and} \quad \beta(\phi) = \frac{6\sqrt{2}g}{4\lambda_M - 13f}.$$

Both  $|\phi\rangle_{0,1} \in \mathcal{S}_{0,1}^2$ , all their superpositions, and all possible mixtures of  $|\phi\rangle_0\langle\phi|$  and  $|\phi\rangle_1\langle\phi|$  give a single point

$$\langle\phi|J_x^2|\phi\rangle = \frac{17 + 4\sqrt{10}\alpha + 5\alpha^2 + 12\sqrt{2}\beta + 13\beta^2}{4(\alpha^2 + 1 + \beta^2)},$$

$$\langle\phi|J_y^2|\phi\rangle = \frac{17 - 4\sqrt{10}\alpha + 5\alpha^2 - 12\sqrt{2}\beta + 13\beta^2}{4(\alpha^2 + 1 + \beta^2)} \quad (71)$$

at the boundary  $\partial\mathcal{E}$  displayed in Fig. 4.

Next we take  $j = 3$ , and the maximum eigenvalue is

$$\lambda_M(\phi) = \begin{cases} \lambda_1(\phi) & \text{for } 0 \leq \phi \leq \frac{\pi}{2} \\ \lambda_2(\phi) & \text{for } \frac{\pi}{2} \leq \phi \leq \frac{5\pi}{4} \\ \lambda_3(\phi) & \text{for } \frac{5\pi}{4} \leq \phi \leq 2\pi \end{cases}, \quad \text{where}$$

$$\lambda_1 = 5f + \sqrt{f^2 + 15g^2}, \quad (72)$$

$$\lambda_2 = \frac{1}{2} (7f - 3g + \sqrt{8\sqrt{2}f^2 - 3fg + 3g^2}), \quad \text{and}$$

$$\lambda_3 = \frac{1}{2} (7f + 3g + \sqrt{8\sqrt{2}f^2 + 3fg + 3g^2})$$

are distinct eigenvalues of  $\Lambda(\phi)$ . The corresponding

eigenkets are

$$|\lambda_1(\phi)\rangle \propto \alpha_1 (|+2\rangle + |-2\rangle) + \beta_1 |0\rangle \in \mathcal{S}_1^2,$$

$$|\lambda_2(\phi)\rangle \propto \alpha_2 (|+3\rangle - |-3\rangle) + \beta_2 (|+1\rangle - |-1\rangle),$$

$$|\lambda_3(\phi)\rangle \propto \alpha_3 (|+3\rangle + |-3\rangle) + \beta_3 (|+1\rangle + |-1\rangle), \quad (73)$$

$$\text{where } \alpha_1 = \sqrt{30}g, \quad \beta_1 = 2\lambda_1 - 8f,$$

$$\alpha_2 = \sqrt{15}g, \quad \beta_2 = 2\lambda_2 - 3f,$$

$$\alpha_3 = \sqrt{15}g, \quad \beta_3 = 2\lambda_3 - 3f,$$

and  $|\lambda_{2,3}\rangle \in \mathcal{S}_0^2$ . Since the three vectors on the right-hand-side in (73) are not normalized, we put the proportionality sign  $\propto$  there. In (72), one can observe that the degree of degeneracy of  $\lambda_M$  is two only at  $\phi = 0, \frac{\pi}{2}$ , and  $\frac{5\pi}{4}$ .

With the unit step function

$$\zeta(\phi) := \begin{cases} 0 & \text{if } \phi < 0 \\ 1 & \text{if } 0 \leq \phi \end{cases}, \quad (74)$$

we can compactly express  $\lambda_M(\phi)$  and the corresponding eigenket

$$|\phi\rangle = |\lambda_1(\phi)\rangle (1 - \zeta(\phi - \frac{\pi}{2})) +$$

$$|\lambda_2(\phi)\rangle \zeta(\phi - \frac{\pi}{2}) (1 - \zeta(\phi - \frac{5\pi}{4})) +$$

$$|\lambda_3(\phi)\rangle \zeta(\phi - \frac{5\pi}{4}) \in \mathcal{H}_7, \quad (75)$$

which provides  $\text{ext}(\mathcal{E}) = \partial\mathcal{E}$ . We present  $\partial\mathcal{E}$  graphically by the (red) solid-curve in Fig. 4 and parametrically by joining

$$\langle\lambda_1|\vec{E}|\lambda_1\rangle = \left( \frac{8\alpha_1^2 + 2\sqrt{30}\alpha_1\beta_1 + 6\beta_1^2}{2\alpha_1^2 + \beta_1^2}, \frac{8\alpha_1^2 - 2\sqrt{30}\alpha_1\beta_1 + 6\beta_1^2}{2\alpha_1^2 + \beta_1^2} \right),$$

$$\langle\lambda_2|\vec{E}|\lambda_2\rangle = \left( \frac{3\alpha_2^2 + 2\sqrt{15}\alpha_2\beta_2 + 5\beta_2^2}{2(\alpha_2^2 + \beta_2^2)}, \frac{3\alpha_2^2 - 2\sqrt{15}\alpha_2\beta_2 + 17\beta_2^2}{2(\alpha_2^2 + \beta_2^2)} \right),$$

$$\langle\lambda_3|\vec{E}|\lambda_3\rangle = \left( \frac{3\alpha_3^2 + 2\sqrt{15}\alpha_3\beta_3 + 17\beta_3^2}{2(\alpha_3^2 + \beta_3^2)}, \frac{3\alpha_3^2 - 2\sqrt{15}\alpha_3\beta_3 + 5\beta_3^2}{2(\alpha_3^2 + \beta_3^2)} \right) \quad (76)$$

for  $\phi \in [0, \frac{\pi}{2})$ ,  $\phi \in [\frac{\pi}{2}, \frac{5\pi}{4})$ , and  $\phi \in [\frac{5\pi}{4}, 2\pi)$ , respectively. In Fig. 4, one can see that these parts of the boundary  $\partial\mathcal{E}$  come from three intersecting ellipses. One can check with (76) that  $\langle\lambda_k|\vec{E}|\lambda_k\rangle := (a_k, b_k)$  for  $k = 1, 2$ , and 3 satisfy the equations

$$\left( \frac{a_1 + b_1 - 10}{2} \right)^2 + \left( \frac{a_1 - b_1}{2\sqrt{15}} \right)^2 = 1,$$

$$\left( \frac{a_2 + b_2 - 7}{4} \right)^2 + \left( \frac{-7a_2 + b_2 + 9}{4\sqrt{15}} \right)^2 = 1, \quad \text{and} \quad (77)$$

$$\left( \frac{a_3 + b_3 - 7}{4} \right)^2 + \left( \frac{a_3 - 7b_3 + 9}{4\sqrt{15}} \right)^2 = 1,$$

respectively, of the ellipses. Like (64), here also both the operators in  $(J_x^2, J_y^2) = \vec{E}$  share a common eigenvector  $|\mathbf{e}\rangle = \frac{1}{\sqrt{2}}(|+2\rangle - |-2\rangle)$ . The eigenvector provides the point  $(4, 4)$  at which all the three ellipses intersect.



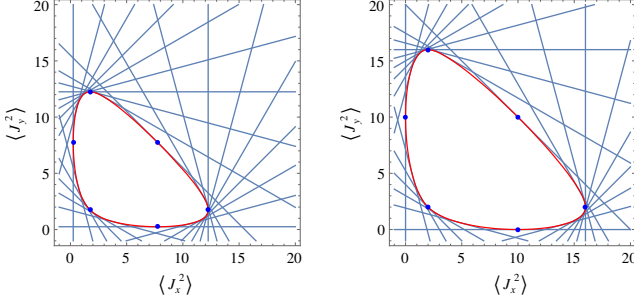


FIG. 5. (Color online) The left and right red closed-curves bound the allowed regions of the mean vectors  $\vec{\epsilon} = (\langle J_x^2 \rangle, \langle J_y^2 \rangle)$  for  $j = \frac{7}{2}$  and  $j = 4$ , respectively. There exists no quantum state for a point outside the closed-curves.

Now we proceed to  $j = \frac{7}{2}$ , where the maximum eigenvalue  $\lambda_M$  is twofold degenerate at all  $\phi$ 's:

$$\begin{aligned} \lambda_M(\phi) &= \frac{1}{4} \left( 21f + s + \frac{1}{2} \sqrt{-4s^2 - 2p - \frac{q}{s}} \right), \\ s(\phi) &= \sqrt{\frac{1}{6} \left( p + \sqrt{\Upsilon_0} \cos \left( \frac{1}{3} \arccos \left( \frac{\Upsilon_1}{2\sqrt{\Upsilon_0^3}} \right) \right) \right)}, \\ p(\phi) &= 168(f^2 + 3g^2), \quad q(\phi) = 512(f^3 - 9fg^2), \quad (78) \\ \Upsilon_0(\phi) &= 48384(f^2 + 3g^2)^2, \quad \text{and} \\ \Upsilon_1(\phi) &= 5971968(3f^6 - 5f^4g^2 + 145f^2g^4 + 49g^6). \end{aligned}$$

The related eigenkets are

$$\begin{aligned} |\phi\rangle_0 &\propto \alpha |+\frac{7}{2}\rangle + |+\frac{3}{2}\rangle + \beta |-\frac{1}{2}\rangle + \varsigma |-\frac{5}{2}\rangle \in \mathcal{S}_0^2, \\ |\phi\rangle_1 &\propto \varsigma |+\frac{5}{2}\rangle + \beta |+\frac{1}{2}\rangle + |-\frac{3}{2}\rangle + \alpha |-\frac{7}{2}\rangle \in \mathcal{S}_1^2, \quad (79) \\ \text{where } \alpha(\phi) &= \frac{2\sqrt{21}g}{4\lambda_M - 7f}, \quad \beta(\phi) = \frac{2\sqrt{21}g\alpha + 27f - 4\lambda_M}{-4\sqrt{15}g}, \\ \text{and } \varsigma(\phi) &= \frac{6\sqrt{5}g}{4\lambda_M - 19f} \beta. \end{aligned}$$

All the maximum-eigenvalue-states of  $\Lambda(\phi)$  give a single boundary point

$$\begin{aligned} \langle \phi | J_x^2 | \phi \rangle &= \frac{27 + 4\sqrt{21}\alpha + 7\alpha^2 + 31\beta^2 + 19\varsigma^2 + 4\sqrt{5}\beta(2\sqrt{3} + 3\varsigma)}{4(\alpha^2 + \beta^2 + \varsigma^2 + 1)}, \\ \langle \phi | J_y^2 | \phi \rangle &= \frac{27 - 4\sqrt{21}\alpha + 7\alpha^2 + 31\beta^2 + 19\varsigma^2 - 4\sqrt{5}\beta(2\sqrt{3} + 3\varsigma)}{4(\alpha^2 + \beta^2 + \varsigma^2 + 1)}, \quad (80) \end{aligned}$$

and the boundary  $\partial\mathcal{E}$  is showcased in Fig. 5. Note that (79) and (80) are not applicable at  $\phi = \frac{\pi}{4}, \frac{5\pi}{4}$ . At these two angles,  $|\phi\rangle$  is the minimum- and maximum-eigenvalue-states of  $J_z^2$ , and the corresponding boundary points are given in (53) and (52).

Next, in the case of  $j = 4$ , the largest eigenvalue of operator (46) is

$$\begin{aligned} \lambda_M(\phi) &= \frac{1}{2} \left[ \frac{40f}{3} + 2\sqrt{\frac{p}{3}} \cos \left( \frac{1}{3} \arccos \left( \frac{-q}{2} \sqrt{\frac{27}{p^3}} \right) \right) \right], \\ p(\phi) &= \frac{208}{3}(f^2 + 3g^2), \quad q(\phi) = \frac{4480}{27}(f^3 - 9fg^2). \quad (81) \end{aligned}$$

TABLE II. From left, the angular momentum quantum numbers are listed in the first column. The second and third columns contain the absolute minima of  $h(\vec{\epsilon})$  and  $u_{1/2}(\vec{\epsilon})$ , respectively. Whereas, the third and forth columns carry the global maxima of  $u_2(\vec{\epsilon})$  and  $u_{\max}(\vec{\epsilon})$  [for  $j > 4$ , see Appendix I]. Each extremum is appended with the  $\phi$ -values at which it occurs on the boundary of  $\mathcal{E}$ . Note that the numerical values given here are rounded to a few decimal places.

$j$	$h$	$u_{1/2}$	$u_2$	$u_{\max}$
$\frac{5}{2}$	0.419 at 1.965, 5.89	2.321 at 0, $\frac{\pi}{2}$	1.781 at 2.29, 5.57	1.882 at 2.36, 5.5
3	0.427 at 1.934, 5.92	2.321 at 0, $\frac{\pi}{2}$	1.774 at 2.281, 5.573	1.878 at 2.356, 5.498
$\frac{7}{2}$	0.351 at 1.981, 5.873	2.288 at 0, $\frac{\pi}{2}$	1.8225 at 2.29, 5.564	1.91 at 2.356, 5.498
4	0.356 at 1.951, 5.903	2.288 at 0, $\frac{\pi}{2}$	1.8164 at 2.282, 5.572	1.9014 at 2.356, 5.498

The associated eigenvector

$$|\phi\rangle_0 \propto \alpha (|+4\rangle + |-4\rangle) + \beta (|+2\rangle + |-2\rangle) + |0\rangle \quad (82)$$

provides an extreme point

$$\begin{aligned} \langle \phi | J_x^2 | \phi \rangle &= \frac{2(5+2\alpha^2+3\sqrt{10}\beta+2\sqrt{7}\alpha\beta+8\beta^2)}{2\alpha^2+2\beta^2+1}, \\ \langle \phi | J_y^2 | \phi \rangle &= \frac{2(5+2\alpha^2-3\sqrt{10}\beta-2\sqrt{7}\alpha\beta+8\beta^2)}{2\alpha^2+2\beta^2+1} \quad (83) \end{aligned}$$

of the numerical range  $\mathcal{E}$ , where

$$\beta(\phi) = \frac{-3\sqrt{10}g}{(2\sqrt{7}g)^2 + 16f - 2\lambda_M}, \quad \alpha(\phi) = \frac{2\sqrt{7}g}{2\lambda_M - 4f} \beta \quad (84)$$

for all except  $\phi = \frac{5\pi}{4}$ . All the extreme points lie on the (red) closed-curve in Fig. 5.

Like (65)–(68), we consider the combined uncertainty and certainty measures based on  $\{h, u_{1/2}\}$  and  $\{u_2, u_{\max}\}$  and achieve their global minima  $\{h, u_{1/2}\}$  and maxima  $\{u_2, u_{\max}\}$ , respectively, by employing the parametric form  $\langle \phi | \vec{E} | \phi \rangle$  of the boundary  $\partial\mathcal{E}$ . Table II carries all the extrema and the values of parameter  $\phi$  at which they occur for  $j = \frac{5}{2}, \dots, 4$ . With the minima and maxima one can have tight URs and CRs such as (65)–(68), and with the  $\phi$ -values one can have the minimum-uncertainty or maximum-certainty states  $|\phi\rangle\langle\phi|$ . Roughly, the extrema occur in those parts of the boundary which are near to the corners of hyperrectangle (47). As we increase  $j$  these parts get closer to the corners, and as  $j \rightarrow \infty$  the allowed region becomes a triangle that shares three corners with the hyperrectangle  $\mathcal{H}$ . Moreover, all our URs and CRs become (more precisely, tends to) trivial in the limit  $j \rightarrow \infty$  [for a justification, see the last two paragraphs of Sec. II].

One can observe that  $\mathcal{E}$  takes the triangular shape as we move from Fig. 3 to Fig. 5. In Fig. 6 and Appendix , we present  $\{h, u_{1/2}, u_2, u_{\max}\}$  as functions of

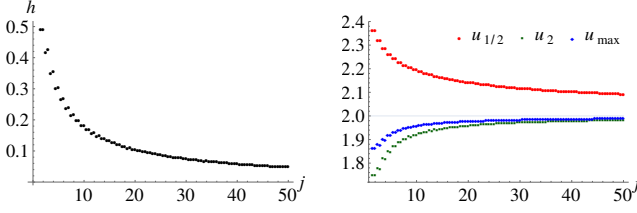


FIG. 6. The left and right plots exhibit the values of  $h$  and of  $\{u_{1/2}, u_2, u_{\max}\}$ , which are obtained numerically for the quantum numbers  $j = \frac{3}{2}, 2, \frac{5}{2}, \dots, 50$ . The values are documented in Appendix . These plots suggest slow convergence in  $h \rightarrow 0$  and  $u_{1/2} \rightarrow 2$  in comparison to  $u_2 \rightarrow 2$  and  $u_{\max} \rightarrow 2$  as  $j \rightarrow \infty$ .

$j = \frac{3}{2}, 2, \dots, 50$ . There one can see that the tight lower bounds  $h$  and  $u_{1/2}$  of  $h(\vec{\epsilon})$  and  $u_{1/2}(\vec{\epsilon})$  decrease toward their trivial lower bounds 0 and 2, respectively, as  $j$  increases. While the upper bounds  $u_2$  and  $u_{\max}$  of  $u_2(\vec{\epsilon})$  and  $u_{\max}(\vec{\epsilon})$  increase in the direction of their trivial upper bound 2.

To visualize  $\mathcal{E}$  for a very large quantum number  $j$ , we first apply the uniform scaling

$$(J_x, J_y, J_z) \mapsto \left( \frac{J_x}{j}, \frac{J_y}{j}, \frac{J_z}{j} \right) \quad (85)$$

and then the limit  $j \rightarrow \infty$ . After which hyperrectangle (47) becomes the square  $[0, 1]^{\times 2}$ , and the extreme points in (52) approach to

$$(1, 0), \quad (0, 1), \quad \text{and} \quad (0, 0), \quad (86)$$

respectively. In the limit  $j \rightarrow \infty$ , the convex hull of points (86) is the allowed region of  $\frac{1}{j^2}(\langle J_y^2 \rangle, \langle J_z^2 \rangle)$ , which is indeed a triangle. It is again justified in Sec. VIII by applying the quantum de Finetti theorem [30, 31]. We want to stress that the boundary-plots in Figs. 2–5 are obtained in [10] by taking a  $N$ -qubit system that we consider in Sec. VIII. By the way, the points in (53) and (54) fall on sides of the triangle after scaling (85) and then the limit.

## VI. ANTICOMMUTATORS OF ANGULAR MOMENTUM OPERATORS

In this section, we consider the anticommutators

$$\begin{aligned} A_1 &:= J_x J_z + J_z J_x, \\ A_2 &:= J_y J_z + J_z J_y, \quad \text{and} \\ A_3 &:= J_x J_y + J_y J_x = -\frac{1}{2} Y_2 \end{aligned} \quad (87)$$

of the angular momentum operators;  $Y_\gamma$  is defined in (31). In Sec. IV, we learned that the maximum and minimum eigenvalues of  $Y_2$  are the same in magnitude but opposite in sign. Hence, the extreme eigenvalues  $\pm a_M$  of  $A_3$  are  $\pm \frac{\lambda_M}{2}$ , where  $\lambda_M$  is—an extreme eigenvalue of  $Y_2$ —listed in Table I. Since the anticommutators in (87) are unitarily equivalent, they all share a common spectrum.

Consequently, in the case of  $\vec{E} = (A_1, A_2, A_3)$ , hyperrectangle (3) is the cube  $[-a_M, a_M]^{\times 3}$ .

First, let us only take  $A_1$  and  $A_2$ . Like in Sec. IV, one can show that the trace of different powers of

$$\Lambda(\phi) = \cos \phi A_1 + \sin \phi A_2 \quad (88)$$

and thus all its eigenvalues are independent of  $\phi$ . As a result, the permitted region of  $(\langle A_1 \rangle, \langle A_2 \rangle)$  is completely identified by the QC

$$\langle A_1 \rangle^2 + \langle A_2 \rangle^2 \leq a_M^2. \quad (89)$$

Since we can cyclically transform one anticommutator into other by a unitary conjugation, the above statements are true for any pair of the three anticommutators. One can check that the orthogonal projection of  $\mathcal{E}$ —given below for  $\vec{E} = (A_1, A_2, A_3)$ —onto the  $\langle A_t \rangle \times \langle A_{t'} \rangle$ -plane,  $t \neq t'$ , is the circular disk specified by a QC such as (89). Moreover, URs and CRs for  $A_t$  and  $A_{t'}$  will be same as (41)–(44) for  $X_\gamma$  and  $Y_\gamma$ .

Now let us take

$$\Lambda(\theta, \phi) = \sin \theta (\cos \phi A_1 + \sin \phi A_2) + \cos \theta A_3 \quad (90)$$

as per (5) and present the allowed region  $\mathcal{E}$  of the mean vector  $\vec{\epsilon} = (\langle A_1 \rangle, \langle A_2 \rangle, \langle A_3 \rangle)$ . In the case of  $j = \frac{1}{2}$ , all the anticommutators are the null operator, thus  $\mathcal{E}$  only carries the origin  $(0, 0, 0)$ . For  $j = 1, \dots, \frac{5}{2}$ , in the following, the maximum eigenvalue  $\lambda_M(\theta, \phi)$  and the associated eigenkets  $|\theta, \phi\rangle$  of  $\Lambda(\theta, \phi)$  are provided as functions of  $\theta \in [0, \pi]$  and  $\phi \in [0, 2\pi)$ . Then it becomes cumbersome to deliver analytic expressions for them. Therefore, in the case of  $j = 3, \frac{7}{2}, 4, 25$ , and 50, we divide both the intervals  $[0, \pi]$  and  $[0, 2\pi]$  into, say,  $\kappa$  and  $\kappa'$  numbers of equal parts. And, only the angles  $\theta_k = k \frac{\pi}{\kappa}$  and  $\phi_{k'} = k' \frac{2\pi}{\kappa'}$  are chosen, where  $k = 0, 1, \dots, \kappa$  and  $k' = 0, 1, \dots, \kappa'$ . For every  $(\theta_k, \phi_{k'})$ , we compute  $\lambda_M, |\theta, \phi\rangle$ , face (14) of  $\mathcal{E}$ , and then by joining these faces we draw boundary (12) of  $\mathcal{E}$  in Figs. 8 and 9. In the next section, almost all plots are generated in this way.

In an even dimension  $d = 2j + 1$ ,  $\lambda_M(\theta, \phi)$  is twofold degenerate at every  $\theta$  and  $\phi$ . Hence, two orthogonal eigenkets  $|\theta, \phi\rangle_{1,2}$  are provided for  $j = \frac{3}{2}, \frac{5}{2}$ . In this section, the subscript of a ket, say,  $|\theta, \phi\rangle_1$  is just an index, and it does not represent that the ket belongs to an invariant subspace  $\mathcal{S}_1$  like before. In odd dimensions  $d = 3, 5, 7$ , and 9,  $\lambda_M(\theta, \phi)$  is twice degenerate only at  $\{(\theta_l, \phi_l)\}_{l=1}^4$ , which are recorded in Table III.

Now we begin with  $j = 1$ , where

$$\lambda_M(\theta, \phi) = \frac{2}{\sqrt{3}} \cos \left( \frac{1}{3} \arccos \left( \frac{-\sqrt{27}}{2} \cos \theta (\sin \theta)^2 \sin(2\phi) \right) \right). \quad (91)$$

At all the four degeneracy points  $\lambda_M = \frac{1}{\sqrt{3}}$ , and the pair

TABLE III. Four  $(\theta_l, \phi_l)$  and the corresponding unit vectors (6) are listed in the right and left columns. By replacing  $\theta$  and  $\phi$  with  $\pi - \theta$  and  $\pi + \phi$ , respectively, one can have the angles for the antipodal vectors  $\{-\hat{\eta}_l\}_{l=1}^4$ .

$\hat{\eta}(\theta, \phi)$	$\theta$	$\phi$
$\hat{\eta}_1 = \frac{1}{\sqrt{3}}(1, 1, 1)$	$\theta_1 = \arccos(\frac{1}{\sqrt{3}})$	$\phi_1 = \frac{\pi}{4}$
$\hat{\eta}_2 = \frac{1}{\sqrt{3}}(-1, 1, -1)$	$\theta_2 = \pi - \theta_1$	$\phi_2 = \frac{3\pi}{4}$
$\hat{\eta}_3 = \frac{1}{\sqrt{3}}(-1, -1, 1)$	$\theta_3 = \theta_1$	$\phi_3 = \frac{5\pi}{4}$
$\hat{\eta}_4 = \frac{1}{\sqrt{3}}(1, -1, -1)$	$\theta_4 = \theta_2$	$\phi_4 = \frac{7\pi}{4}$

$|\theta_l, \phi_l\rangle_{1,2}$  of eigenkets are

$$\begin{aligned}
|\theta_1, \phi_1\rangle_1 &= \frac{1}{\sqrt{2}}(|+1\rangle + i|-1\rangle) = |\theta_3, \phi_3\rangle_1, \\
|\theta_2, \phi_2\rangle_1 &= \frac{1}{\sqrt{2}}(|+1\rangle - i|-1\rangle) = |\theta_4, \phi_4\rangle_1, \\
|\theta_1, \phi_1\rangle_2 &= \frac{1}{\sqrt{6}}(e^{-i\frac{\pi}{4}}|+1\rangle + 2|0\rangle - e^{i\frac{\pi}{4}}|-1\rangle), \\
|\theta_2, \phi_2\rangle_2 &= \frac{1}{\sqrt{6}}(-e^{i\frac{\pi}{4}}|+1\rangle + 2|0\rangle + e^{-i\frac{\pi}{4}}|-1\rangle), \\
|\theta_3, \phi_3\rangle_2 &= \frac{1}{\sqrt{6}}(-e^{-i\frac{\pi}{4}}|+1\rangle + 2|0\rangle + e^{i\frac{\pi}{4}}|-1\rangle), \quad \text{and} \\
|\theta_4, \phi_4\rangle_2 &= \frac{1}{\sqrt{6}}(e^{i\frac{\pi}{4}}|+1\rangle + 2|0\rangle - e^{-i\frac{\pi}{4}}|-1\rangle).
\end{aligned} \tag{92}$$

At each  $(\theta_l, \phi_l)$ , by varying  $\mu \in [0, \frac{\pi}{2}]$  and  $\nu \in [0, 2\pi]$  in a general eigenket

$$|\theta_l, \phi_l\rangle = \cos \mu |\theta_l, \phi_l\rangle_1 + \sin \mu e^{i\nu} |\theta_l, \phi_l\rangle_2, \tag{93}$$

one can generate the face  $\mathcal{F}(\theta_l, \phi_l)$  of allowed region  $\mathcal{E}$  according to (14). These four faces are circular disks,  $\mathcal{F}(\theta_3, \phi_3)$  on  $\mathcal{E}$  is shown in Fig. 7 with its normal vector  $\hat{\eta}_3$ . Moreover, the four circles (boundary of the disks) are intersections of  $\partial\mathcal{E}$  and the unit sphere centered at the origin.

The maximum-eigenvalue-ket

$$|\theta, \phi\rangle = \begin{cases} |\theta_1, \phi_1\rangle_1 & \text{for } \theta \in [0, \theta_1) \text{ and } \phi \in \{\phi_1, \phi_3\} \\ |\theta_2, \phi_2\rangle_1 & \text{for } \theta \in (\theta_2, \pi] \text{ and } \phi \in \{\phi_2, \phi_4\} \end{cases}, \tag{94}$$

and for the rest of angles, the eigenkets are

$$\begin{aligned}
|\theta, \phi\rangle &\propto \alpha |+1\rangle + \beta |0\rangle + \varsigma |-1\rangle, \quad \text{where} \\
\alpha &= (e^{-i\phi} \lambda_M + i e^{i\phi} \cos \theta) \sin \theta, \\
\beta &= \sqrt{2}(\lambda_M^2 - (\cos \theta)^2), \quad \text{and} \\
\varsigma &= (-e^{i\phi} \lambda_M + i e^{-i\phi} \cos \theta) \sin \theta.
\end{aligned} \tag{95}$$

The eigenkets in (95) provide the parametric form

$$\begin{aligned}
\langle \theta, \phi | A_1 | \theta, \phi \rangle &= \frac{\beta((\alpha + \bar{\alpha}) - (\varsigma + \bar{\varsigma}))}{\sqrt{2}(|\alpha|^2 + \beta^2 + |\varsigma|^2)}, \\
\langle \theta, \phi | A_2 | \theta, \phi \rangle &= \frac{i\beta((\alpha - \bar{\alpha}) + (\varsigma - \bar{\varsigma}))}{\sqrt{2}(|\alpha|^2 + \beta^2 + |\varsigma|^2)}, \\
\langle \theta, \phi | A_3 | \theta, \phi \rangle &= \frac{i(\alpha \bar{\varsigma} - \bar{\alpha} \varsigma)}{|\alpha|^2 + \beta^2 + |\varsigma|^2}
\end{aligned} \tag{96}$$

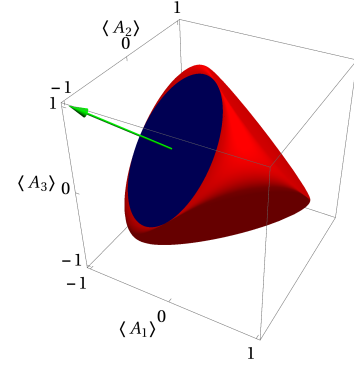


FIG. 7. (Color online) In the case of  $j = 1$ ,  $a_M = 1$ , and the numerical range  $\mathcal{E}$  of  $\vec{E} = (A_1, A_2, A_3)$  is the red strawberry-shaped region with the blue circular disk. The disk is the face  $\mathcal{F}(\theta_3, \phi_3)$  of  $\mathcal{E}$ , and the arrow is in the direction of its normal  $\hat{\eta}_3$ . There are total four such disks—normal to each unit vector  $\hat{\eta}_l$  in Table III—that are parts of the boundary  $\partial\mathcal{E}$ .

of the part—other than the four circular disks—of the boundary  $\partial\mathcal{E}$ . The overline in  $\bar{\alpha}$  denotes the complex conjugation of  $\alpha$ . With (96), one can realize that  $\mathcal{E}$  is the convex hull of Steiner's Roman surface described by

$$(\mathbf{a}_1 \mathbf{a}_2)^2 + (\mathbf{a}_2 \mathbf{a}_3)^2 + (\mathbf{a}_3 \mathbf{a}_1)^2 = -2 \mathbf{a}_1 \mathbf{a}_2 \mathbf{a}_3 \tag{97}$$

in [38] (see also [3, 6]), here  $-1 \leq \mathbf{a}_t = \frac{\langle A_t \rangle}{a_M} \leq 1$  and  $t = 1, 2, 3$ .

We combine (un)certainly measures for the three anti-commutators with respect to (15)–(19). Then, to reach their absolute extrema on the boundary, we vary the two angles in (96) and thus obtain the tight URs and CRs

$$\frac{1}{2}(6 \ln 6 - 5 \ln 5) \leq \sum_{t=1}^3 h(\langle A_t \rangle) = h(\vec{\epsilon}), \tag{98}$$

$$1 + 2\sqrt{2} \leq \sum_{t=1}^3 u_{1/2}(\langle A_t \rangle), \tag{99}$$

$$\sum_{t=1}^3 u_2(\langle A_t \rangle) \leq \frac{13}{6}, \quad \text{and} \tag{100}$$

$$\sum_{t=1}^3 u_{\max}(\langle A_t \rangle) \leq \frac{5}{2}. \tag{101}$$

Inequalities (98), (100), and (101) are saturated by the maximum-eigenvalue-states of  $-\hat{\eta}_l \cdot \vec{E}$  for  $l = 1, \dots, 4$  [for  $\hat{\eta}_l$ , see Table III]. Whereas (99) is saturated by the six extreme-eigenvalue-states of  $A_1, A_2$ , and  $A_3$ .

Next we pick  $j = \frac{3}{2}$ , where  $\lambda_M(\theta, \phi) = \sqrt{3} = a_M$  is the same for all angles. One can check that both the orthonormal eigenkets

$$\begin{aligned}
|\theta, \phi\rangle_1 &= \frac{1}{\sqrt{2}}(e^{-i\phi} \sin \theta |+\frac{3}{2}\rangle + |+\frac{1}{2}\rangle + i \cos \theta |-\frac{3}{2}\rangle), \\
|\theta, \phi\rangle_2 &= \frac{1}{\sqrt{2}}(-i \cos \theta |+\frac{3}{2}\rangle + |-\frac{1}{2}\rangle - e^{i\phi} \sin \theta |-\frac{3}{2}\rangle)
\end{aligned} \tag{102}$$

and all there normalized linear combinations such as (93) deliver a single point on the sphere of radius  $\sqrt{3}$  centered at the origin. In a nutshell, here the numerical range is bounded by the QC

$$\langle A_1 \rangle^2 + \langle A_2 \rangle^2 + \langle A_3 \rangle^2 \leq a_M^2. \quad (103)$$

Now we move to  $j = 2$ , where  $\lambda_M(\theta, \phi) = \sqrt{12} = a_M$  is also independent of both the angles, hence  $\mathcal{E}$  is completely determined by QC (103). Except for  $\theta \in \{\theta_1, \theta_2\}$ , here the maximum-eigenvalue-ket is given by

$$\begin{aligned} |\theta, \phi\rangle &\propto \alpha|+2\rangle + \beta|+1\rangle + |0\rangle + \varsigma|-1\rangle + \xi|-2\rangle, \text{ where} \\ \alpha &= \frac{3e^{-i\phi}(\sin\theta)\beta - i\sqrt{6}\cos\theta}{\sqrt{12}}, \\ \xi &= \frac{-3e^{i\phi}(\sin\theta)\varsigma + i\sqrt{6}\cos\theta}{\sqrt{12}}, \\ \beta &= \frac{((-i3e^{i\phi}\cos\theta + \sqrt{3}e^{-i\phi})c - i3\cos\theta(-i3e^{-i\phi}\cos\theta - \sqrt{3}e^{i\phi}))\sin\theta}{\sqrt{2}(c^2 - 9(\cos\theta)^2)}, \\ \varsigma &= \frac{((-i3e^{-i\phi}\cos\theta - \sqrt{3}e^{i\phi})c + i3\cos\theta(-i3e^{i\phi}\cos\theta + \sqrt{3}e^{-i\phi}))\sin\theta}{\sqrt{2}(c^2 - 9(\cos\theta)^2)}, \\ c &= \sqrt{12} - \frac{9(\sin\theta)^2}{\sqrt{12}}. \end{aligned} \quad (104)$$

At  $\theta = \theta_1$  and  $\theta = \theta_2$ , the denominators of  $\beta$  and  $\varsigma$  become zero, then (104) is no more applicable. In these cases, the eigenkets are

$$\begin{aligned} |\theta_1, \phi\rangle &= \frac{1}{\sqrt{6}}(e^{-i\phi}|+2\rangle + \sqrt{2}|+1\rangle + i\sqrt{2}|-1\rangle - ie^{i\phi}|-2\rangle), \\ |\theta_2, \phi\rangle &= \frac{1}{\sqrt{6}}(e^{-i\phi}|+2\rangle + \sqrt{2}|+1\rangle - i\sqrt{2}|-1\rangle + ie^{i\phi}|-2\rangle). \end{aligned} \quad (105)$$

As  $\lambda_M$  is twofold degenerate in the four directions. For each  $(\theta_l, \phi_l)$  in Table III, one eigenket can be retrieved from (105) and the other orthonormal eigenkets are

$$\begin{aligned} |\theta_1, \phi_1\rangle_2 &= \frac{1}{3}(\sqrt{2}|+2\rangle + e^{i\frac{\pi}{4}}|+1\rangle + i\sqrt{3}|0\rangle + e^{-i\frac{\pi}{4}}|-1\rangle - \sqrt{2}|-2\rangle), \\ |\theta_2, \phi_2\rangle_2 &= \frac{1}{3}(-\sqrt{2}|+2\rangle + e^{-i\frac{\pi}{4}}|+1\rangle + i\sqrt{3}|0\rangle + e^{i\frac{\pi}{4}}|-1\rangle + \sqrt{2}|-2\rangle), \\ |\theta_3, \phi_3\rangle_2 &= \frac{1}{3}(-\sqrt{2}|+2\rangle + e^{i\frac{\pi}{4}}|+1\rangle - i\sqrt{3}|0\rangle + e^{-i\frac{\pi}{4}}|-1\rangle + \sqrt{2}|-2\rangle), \\ |\theta_4, \phi_4\rangle_2 &= \frac{1}{3}(-\sqrt{2}|+2\rangle - e^{-i\frac{\pi}{4}}|+1\rangle + i\sqrt{3}|0\rangle - e^{i\frac{\pi}{4}}|-1\rangle + \sqrt{2}|-2\rangle). \end{aligned} \quad (106)$$

One can verify that the eigenkets in (104)–(106) yield different points

$$\langle\theta, \phi|\vec{E}|\theta, \phi\rangle = a_M \hat{\eta}(\theta, \phi) \quad (107)$$

of the boundary  $\partial\mathcal{E}$ , which is a sphere.

Like (98)–(101), here we achieve

$$2\ln 2 = \mathfrak{h} \leq h(\vec{\epsilon}) \quad (108)$$

$$1 + 2\sqrt{2} = \mathbf{u}_{1/2} \leq \mathbf{u}_{1/2}(\vec{\epsilon}), \quad (109)$$

$$\mathbf{u}_2(\vec{\epsilon}) \leq \mathbf{u}_2 = 2, \quad \text{and} \quad (110)$$

$$\mathbf{u}_{\max}(\vec{\epsilon}) \leq \mathbf{u}_{\max} = \frac{1}{2}(3 + \sqrt{3}) \quad (111)$$

by using parametric form (107) for both  $j = \frac{3}{2}$  as well as  $j = 2$ . Since  $\partial\mathcal{E}$  specified by (28) is also a sphere, the same URs and CRs (108)–(111) are reported in [15]

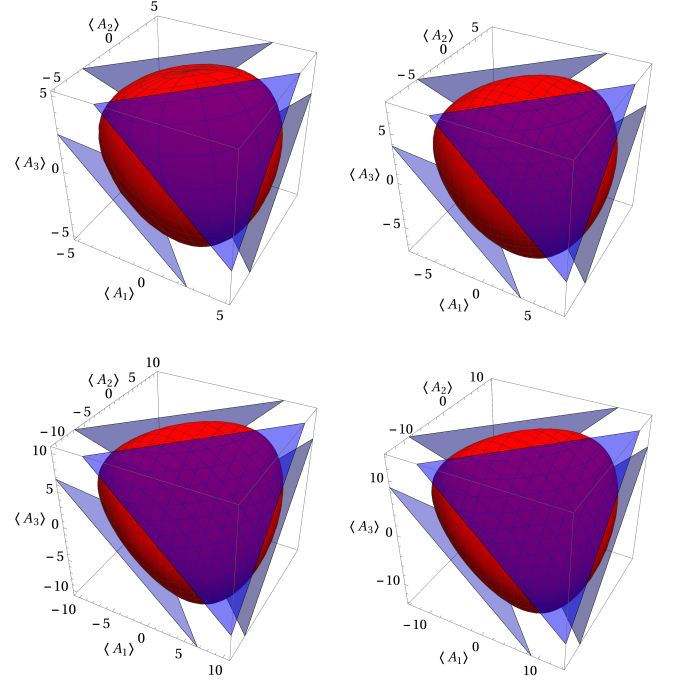


FIG. 8. (Color online) From top-left to bottom-right, moving horizontally, the allowed regions  $\mathcal{E}$  for the three anticommutators in (87) are illustrated by the red convex bodies for  $j = \frac{5}{2}, 3, \frac{7}{2}$ , and 4. The four supporting hyperplanes shown in blue color are normal to the four unit-vectors  $-\hat{\eta}_l$  registered in Table III.

for the three angular momentum operators. QC (103) and CR (110) are equal, therefore every  $|\theta, \phi\rangle\langle\theta, \phi|$  saturates (110). For URs (108) and (109), the minimum uncertainty states are the eigenstates of  $A_1, A_2, A_3$  related to their extreme-eigenvalues  $\pm a_M$ . The maximum- and minimum-eigenvalue-states of  $\Lambda(\theta_l, \phi_l)$  for every  $l = 1, \dots, 4$  saturate CR (111).

Next we take  $j = \frac{5}{2}$ , where  $\lambda_M(\theta, \phi)$  is

$$4\sqrt{\frac{7}{3}} \cos\left(\frac{1}{3} \arccos\left(5 \cos\theta(\sin\theta)^2 \sin(2\phi) \sqrt{\frac{3^3}{7^3}}\right)\right) \quad (112)$$

for all  $\theta$  and  $\phi$ . The two orthonormal eigenkets associated with  $\lambda_M$  are

$$\begin{aligned} |\theta, \phi\rangle_1 &\propto \alpha_1|+\frac{5}{2}\rangle + \beta_1|+\frac{3}{2}\rangle + |+\frac{1}{2}\rangle + \varsigma_1|-\frac{3}{2}\rangle + \xi_1|-\frac{5}{2}\rangle, \\ |\theta, \phi\rangle_2 &\propto \alpha_2|+\frac{5}{2}\rangle + \beta_2|+\frac{3}{2}\rangle + |-\frac{1}{2}\rangle + \varsigma_2|-\frac{3}{2}\rangle + \xi_2|-\frac{5}{2}\rangle, \end{aligned} \quad (113)$$

where

$$\begin{aligned}
\alpha_1 &= \frac{2\sqrt{5} e^{-i\phi} (\sin \theta) \beta_1 - i\sqrt{10} \cos \theta}{\lambda_M}, \\
\xi_1 &= \frac{-2\sqrt{5} e^{i\phi} (\sin \theta) \varsigma_1}{\lambda_M}, \\
\beta_1 &= \frac{2(-i\sqrt{50} e^{i\phi} \cos \theta + \sqrt{2} e^{-i\phi} \lambda_M) \sin \theta}{\lambda_M^2 - 20(\sin \theta)^2}, \\
\varsigma_1 &= \frac{i3\sqrt{2} \cos \theta \lambda_M}{\lambda_M^2 - 20(\sin \theta)^2}, \\
\alpha_2 &= \frac{2\sqrt{5} e^{-i\phi} (\sin \theta) \beta_2}{\lambda_M}, \\
\xi_2 &= \frac{-2\sqrt{5} e^{i\phi} (\sin \theta) \varsigma_2 + i\sqrt{10} \cos \theta}{\lambda_M}, \\
\beta_2 &= \frac{-i3\sqrt{2} \cos \theta \lambda_M}{\lambda_M^2 - 20(\sin \theta)^2}, \quad \text{and} \\
\varsigma_2 &= \frac{2(-i\sqrt{50} e^{-i\phi} \cos \theta - \sqrt{2} e^{i\phi} \lambda_M) \sin \theta}{\lambda_M^2 - 20(\sin \theta)^2}.
\end{aligned} \tag{114}$$

Both  $|\theta, \phi\rangle_{1,2}$  and all their superpositions provide a single boundary-point  $\langle \theta, \phi | \vec{E} | \theta, \phi \rangle$  of  $\mathcal{E}$ . The permitted regions for  $\vec{E} = (A_1, A_2, A_3)$ —with their four supporting hyperplanes (9) at  $\{(\pi - \theta_l, \pi + \phi_l)\}_{l=1}^4$ —are displayed in Fig. 8 for  $j = \frac{5}{2}, 3, \frac{7}{2}$ , and 4. To draw  $\partial\mathcal{E}$  for  $j = \frac{5}{2}$ , (112)–(114) are used. While, for  $j = 3, \frac{7}{2}$ , and 4, we obtain  $\partial\mathcal{E}$  numerically as described at the beginning of this section.

Like (85), now we apply the uniform scaling

$$(A_1, A_2, A_3) \mapsto \frac{1}{a_M}(A_1, A_2, A_3) = \frac{1}{a_M} \vec{E}, \tag{115}$$

and then the allowed region  $\mathcal{E}^{\text{US}}$  of  $\frac{1}{a_M} \vec{E}$  will be in the hyperrectangle  $\mathcal{H}^{\text{US}} = [-1, 1]^{\times 3}$  provided  $j \geq 1$ . Up to  $j = 50$  we have checked that  $\langle \pm a_M^{(t)} | A_{t'} | \pm a_M^{(t)} \rangle = \pm a_M \delta_{t t'}$  holds true, where  $|\pm a_M^{(t)}\rangle$  are the eigenkets of  $A_t$  corresponding to the extreme eigenvalues  $\pm a_M$ , and  $\delta_{t t'}$  is the Kronecker delta function. The above statement seems to hold for all  $j \geq 1$ , hence

$$(\pm 1, 0, 0), (0, \pm 1, 0), \text{ and } (0, 0, \pm 1) \tag{116}$$

will be the extreme points of  $\mathcal{E}^{\text{US}}$ .

According to (103),  $\mathcal{E}^{\text{US}}$  is the unit ball for  $j = \frac{3}{2}, 2$ , and as we increase  $j$  one can observe in Figs. 8 and 9 that  $\mathcal{E}^{\text{US}}$  monotonically contracts in the four directions  $\{-\hat{\eta}_l\}_{l=1}^4$  and expands in their antipodal directions  $\{\hat{\eta}_l\}_{l=1}^4$ . Using the quantum de Finetti theorem [30, 31] in the limit  $j \rightarrow \infty$ , we show in Sec. VIII that  $\mathcal{E}^{\text{US}}$  is the convex hull of Steiner's Roman surface characterized by

$$(\mathbf{a}_1 \mathbf{a}_2)^2 + (\mathbf{a}_2 \mathbf{a}_3)^2 + (\mathbf{a}_3 \mathbf{a}_1)^2 = 2 \mathbf{a}_1 \mathbf{a}_2 \mathbf{a}_3, \tag{117}$$

recall that  $-1 \leq \mathbf{a}_t = \frac{\langle A_t \rangle}{a_M} \leq 1$  for  $t = 1, 2$ , and 3. Even at a finite  $j$  one can clearly recognize the Roman surface, (117), in Fig. 9 that displays  $\mathcal{E}^{\text{US}}$  for  $j = 25, 50$ .

An uncertainty measure such as  $h(\vec{\epsilon})$  on  $\mathcal{E}$  is basically  $h(\frac{\vec{\epsilon}}{a_M})$  on  $\mathcal{E}^{\text{US}}$ . For  $j = \frac{3}{2}, 2, \dots, \frac{9}{2}$ ,  $h(\frac{\vec{\epsilon}}{a_M})$  reaches its absolute minimum  $\mathfrak{h} = 2 \ln 2$  at the six points in (116), and for all other  $j \geq 5$  the minimum  $\mathfrak{h}$  occurs at the four points

$$\frac{\langle \theta_l, \phi_l | \vec{E} | \theta_l, \phi_l \rangle}{a_M} = \frac{\langle \theta_l, \phi_l | A_1 | \theta_l, \phi_l \rangle}{a_M} \sqrt{3} \hat{\eta}_l \tag{118}$$

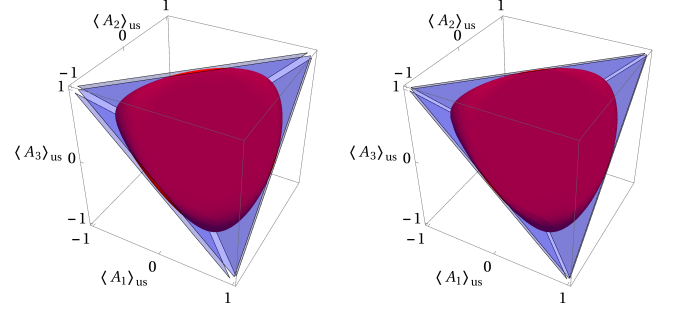


FIG. 9. (Color online) The red convex bodies on left- and right-hand-side represent regions  $\mathcal{E}^{\text{US}}$  of the average vectors  $\frac{1}{a_M} \vec{E}$  for the large quantum numbers  $j = 25$  and  $j = 50$ , respectively, for which  $a_M = 614.689$  and  $a_M = 2479.333$ . Here  $\langle A \rangle_{\text{US}}$  denotes  $\frac{\langle A \rangle}{a_M}$ . Like in Fig. 8, the four tangent hyperplane are painted in blue color.

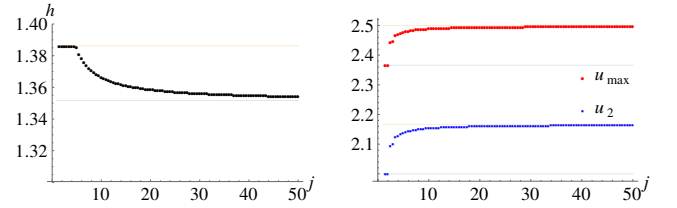


FIG. 10. We present list-plots of the tight lower bound  $\mathfrak{h}$  and the tight upper bounds  $\{u_2, u_{\text{max}}\}$  in the left and right panels for  $j = \frac{3}{2}, 2, \frac{5}{2}, \dots, 50$ . These bounds are printed in Appendix , with which one can enjoy the tight UR  $\mathfrak{h} \leq h(\vec{\epsilon})$  and the CRs  $u_2 \leq u_2(\vec{\epsilon})$  and  $u_{\text{max}} \leq u_{\text{max}}(\vec{\epsilon})$  for  $\{A_1, A_2, A_3\}$ .

in the directions  $\{\hat{\eta}_l\}_{l=1}^4$ . Although the maximum eigenvalue of  $\hat{\eta}_l \cdot \vec{E}$  is double degenerate but all its associated eigenkets  $|\theta_l, \phi_l\rangle$  give a single point (118) as long as  $j > 1$ . The mean value

$$\frac{\langle \theta_1, \phi_1 | A_1 | \theta_1, \phi_1 \rangle}{a_M} \in \left[ \frac{1}{\sqrt{3}}, \frac{2}{3} \right] \quad \text{for all } j > 1, \tag{119}$$

and it is given in Appendix for  $j = \frac{3}{2}, \dots, 50$ . Taking those numerical values, we compute  $h(\vec{\epsilon})$  at an extreme point (118) in order to have the tight lower bound  $\mathfrak{h}$  for  $j \geq 5$ . The values of  $\mathfrak{h}$  for  $j = \frac{3}{2}, \dots, 50$  are then plotted in Fig. 10 and recorded in Appendix .

The global minimum  $u_{1/2} = 1 + 2\sqrt{2}$  of combined uncertainty measure  $u_{1/2}(\vec{\epsilon}) \equiv u_{1/2}(\frac{\vec{\epsilon}}{a_M})$  occurs at points (116) for every  $j \geq 1$ , hence tight UR (109) [see also (99)] holds for all  $j \geq 1$ . The extreme-eigenvalue-kets  $|\pm a_M^{(t)}\rangle$  of the anticommutators are the minimum uncertainty kets for this UR. Next, both certainty measures  $u_2(\vec{\epsilon})$  and  $u_{\text{max}}(\vec{\epsilon})$  achieve their absolute maxima at the four points in (118) for  $j > 1$ , and thus the CRs  $u_2 \leq u_2(\vec{\epsilon})$  and  $u_{\text{max}} \leq u_{\text{max}}(\vec{\epsilon})$  are saturated by the maximum-eigenvalue-states of  $\hat{\eta}_l \cdot \vec{E}$ ,  $l = 1, \dots, 4$ . Like  $h(\vec{\epsilon})$ , taking mean value (119) from Appendix , we compute the upper bounds  $u_2$  and  $u_{\text{max}}$  for  $j = \frac{3}{2}, \dots, 50$ , record them in Appendix and plot them in Fig. 10.



In a nutshell, the lower- and upper-bounds of combined uncertainty- and certainty-measures obey:

$$\begin{aligned} \mathfrak{h} &\in \left[ \frac{1}{2}(6 \ln 6 - 5 \ln 5), 2 \ln 2 \right], \quad \mathfrak{u}_{1/2} = 1 + 2\sqrt{2}, \\ \mathfrak{u}_2 &\in \left[ 2, \frac{13}{6} \right], \quad \text{and} \quad \mathfrak{u}_{\max} \in \left[ \frac{1}{2}(3 + \sqrt{3}), \frac{5}{2} \right] \end{aligned} \quad (120)$$

for all  $j = 1, \frac{3}{2}, \dots, \infty$ . In Fig. 10 [see also Appendix ], one can perceive that as  $j$  increases  $\mathfrak{h}$  monotonically decreases whereas both  $\mathfrak{u}_2$  and  $\mathfrak{u}_{\max}$  increases, and in the limit  $j \rightarrow \infty$  we have

$$\begin{aligned} \frac{\langle \theta_1, \phi_1 | A_1 | \theta_1, \phi_1 \rangle}{a_M} &\rightarrow \frac{2}{3}, \\ \mathfrak{h} &\rightarrow \frac{1}{2}(6 \ln 6 - 5 \ln 5), \\ \mathfrak{u}_2 &\rightarrow \frac{13}{6}, \quad \text{and} \\ \mathfrak{u}_{\max} &\rightarrow \frac{5}{2}. \end{aligned} \quad (121)$$

Although relations (98)–(101) are not always tight but they are nontrivial and hold for all  $j = 1, \frac{3}{2}, \dots, \infty$ .

## VII. POWERS OF ANGULAR MOMENTUM OPERATORS

The first and second powers of angular momentum operators are studied in Secs. III and V, respectively, here we consider

$$\vec{E}_\gamma = ((J_x)^\gamma, (J_y)^\gamma, (J_z)^\gamma) \quad (122)$$

with higher but finite integer powers  $\gamma = 3, 4, \dots$ . Since analytic expressions of  $\lambda_M(\theta, \phi)$  and  $|\theta, \phi\rangle$  are cumbersome, we compute here the boundary points  $\langle \theta, \phi | \vec{E}_\gamma | \theta, \phi \rangle$  numerically by taking only a finite set of  $(\theta_k, \phi_{k'})$ . Then, by connecting these points as per (12) and (14), we draw boundaries of the allowed regions in Figs. 11, 13, 15, and 16.

Let us first take odd powers  $\gamma = 3, 5, \dots$ , where hyperrectangle (3) for  $\vec{E}_\gamma$  will be the cube  $[-j^\gamma, j^\gamma]^{\times 3}$ . Since  $J_x^\gamma$  is directly proportional to  $J_x$  when  $j = \frac{1}{2}, 1$ , the allowed region  $\mathcal{E}_\gamma$  is bounded by the sphere—centered at the origin  $(0, 0, 0)$ —of radius  $j^\gamma$  for the two quantum numbers. By picking  $\gamma = 3$ , we display  $\mathcal{E}_3$  for  $j = \frac{3}{2}, 2, \frac{5}{2}$ , and 10 in Fig. 11. One can observe that as we increase  $j$  the (boundary of) allowed region changes its shape from a sphere to an octahedron, in fact, it is true for all finite odd powers  $\gamma > 1$ .

Now, let us apply uniform scaling (85), where the permissible region for  $\frac{1}{j^\gamma} \vec{E}_\gamma$  is denoted by  $\mathcal{E}_\gamma^{\text{US}}$ . For every  $j$  and all positive odd powers,

$$(\pm 1, 0, 0), (0, \pm 1, 0), \text{ and } (0, 0, \pm 1) \quad (123)$$

lie on the boundary of  $\mathcal{E}_\gamma^{\text{US}}$ . These six extreme points [see Fig. 11] come from the eigenkets of  $J_x, J_y$ , and  $J_z$  corresponding to the eigenvalues  $\pm j$ . In the case of an odd  $\gamma > 1$ , as we increase  $j$  from  $\frac{1}{2}$  to  $\infty$ ,  $\mathcal{E}_\gamma^{\text{US}}$  monotonically shrinks from the unit sphere centered at the origin

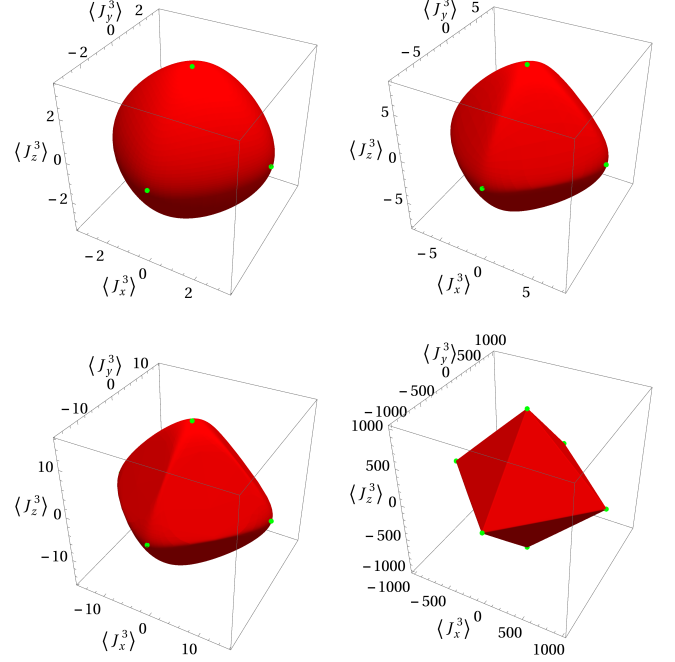


FIG. 11. (Color online) From top-left to bottom-right, moving row by row, the numerical ranges of  $\vec{E}_{\gamma=3}$  of (122) for  $j = \frac{3}{2}, 2, \frac{5}{2}$ , and 10 are the red convex bodies. For each  $j$ , the green extreme points  $(\pm j^3, 0, 0)$ ,  $(0, \pm j^3, 0)$ , and  $(0, 0, \pm j^3)$  are provided by the extreme-eigenvalue-kets of  $J_x, J_y$ , and  $J_z$ .

to the octahedron with vertices (123). With the help of quantum de Finetti theorem [30, 31], it is shown in Sec. VIII that indeed  $\mathcal{E}_\gamma^{\text{US}}$  becomes the octahedron in the limit  $j \rightarrow \infty$ . The eight unit vectors  $\{\pm \hat{\eta}_l\}_{l=1}^4$  in Table III are normals to eight faces of the octahedron. With these vectors, we define another family of regions

$$\mathcal{G}_\vartheta := \left\{ \vec{r} \in [-1, 1]^{\times 3} \mid \sum_{l=1}^4 (\sqrt{3} \hat{\eta}_l \cdot \vec{r})^{2\vartheta} \leq 4 \right\} \quad (124)$$

such that as we increase  $\vartheta \in \{1, 2, 3, \dots, \infty\}$   $\mathcal{G}_\vartheta$  also contracts from the unit sphere to the octahedron, and points (123) lie on the boundary of every  $\mathcal{G}_\vartheta$  like  $\mathcal{E}_\gamma^{\text{US}}$ . Moreover, there always exit two  $\vartheta \leq \vartheta'$  such that  $\mathcal{G}_\vartheta \supseteq \mathcal{E}_\gamma^{\text{US}} \supseteq \mathcal{G}_{\vartheta'}$ , hence  $\mathcal{G}_\vartheta$  and  $\mathcal{G}_{\vartheta'}$  are outer and inner approximations of the numerical range  $\mathcal{E}_\gamma^{\text{US}}$ . In particular, the boundary  $\partial \mathcal{E}_\gamma^{\text{US}}$  lies between the octahedron  $\partial \mathcal{G}_\infty$  and the unit sphere  $\partial \mathcal{G}_1$ .

Recall that the two extreme eigenvalues of an operator in  $\frac{1}{j^\gamma} \vec{E}_\gamma$  [for  $\vec{E}_\gamma$ , see (122)] are  $\pm 1$  for an odd number  $\gamma$ . Using (15)–(19), we establish uncertainty and certainty functions of the mean vector  $\vec{\epsilon} = \frac{1}{j^\gamma} \langle \vec{E}_\gamma \rangle$  and achieve

$$2 \ln 2 \leq h(\vec{\epsilon}), \quad (125)$$

$$1 + 2\sqrt{2} \leq u_{1/2}(\vec{\epsilon}), \quad (126)$$

$$u_2(\vec{\epsilon}) \leq 2, \quad \text{and} \quad (127)$$

$$u_{\max}(\vec{\epsilon}) \leq \mathfrak{u}_{\max} \in \left[ 2, \frac{3+\sqrt{3}}{2} \right] \quad (128)$$



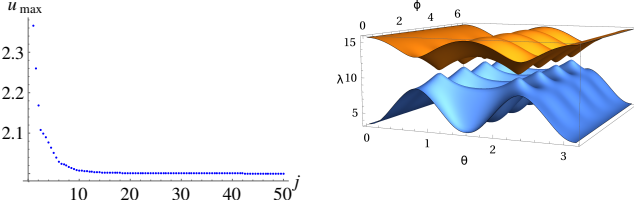


FIG. 12. On the left-hand-side, taking  $\gamma = 3$ , we plot the values of upper-bound  $u_{\max}$ —appears in tight CR (128)—for  $j = 1, \frac{3}{2}, 2, \dots, 50$ . The values are filed in Appendix . On the right-hand-side, choosing  $\gamma = 3$  and  $j = \frac{5}{2}$ , we plot the largest and second-largest eigenvalues  $\lambda(\theta, \phi)$  of  $\hat{\eta}(\theta, \phi) \cdot \vec{E}_\gamma$  as functions of  $\theta$  and  $\phi$  [for  $\vec{E}_\gamma$ , see (122)]. One can recognize that the gap between eigenvalues is the smallest at  $\{(\theta_l, \phi_l), (\pi - \theta_l, \pi + \phi_l)\}_{l=1}^4$  [for  $(\theta_l, \phi_l)$ , see Table III].

on  $\mathcal{E}_\gamma^{\text{us}} \subseteq \mathcal{G}_1$ . The functions  $h, u_{1/2}$ , and  $u_2$  reach their lower and upper bounds at the six extreme points in (123). Hence, inequalities (125)–(127) are saturated by the extreme-eigenvalue-states of  $J_x, J_y$ , and  $J_z$ . These three relations hold for all  $j$  and positive odd powers  $\gamma$ .

The CR (128) is saturated by the extreme-eigenvalue-states of the operators,  $\pm \hat{\eta}_l \cdot \vec{E}_\gamma$ , in the eight directions  $\{\pm \hat{\eta}_l\}_{l=1}^4$ . Since the numerical range  $\mathcal{E}_\gamma^{\text{us}}$  shrinks in these directions, the upper bound  $u_{\max}$  decreases monotonically from  $\frac{3+\sqrt{3}}{2}$  to 2 as  $j$  goes from  $\frac{1}{2}$  to  $\infty$ . In Fig. 12 and Appendix , taking  $\gamma = 3$ , we present the values of  $u_{\max}$  for  $j = 1, \frac{3}{2}, 2, \dots, 50$ . One can clearly observe predictions of the quantum de Finetti theorem even at  $j = 10$ :  $\mathcal{E}_3^{\text{us}}$  in Fig. 11 becomes almost the octahedron, and  $u_{\max} \approx 2.00759$  [see Appendix and Fig. 12] approaches 2. If one wants a CR based on  $u_{\max}$  that holds for all the quantum numbers  $j$  then  $u_{\max}(\vec{\epsilon}) \leq \frac{3+\sqrt{3}}{2}$  can be adopted, it is not tight for  $j > 1$  but it is non-trivial. Besides, one can safely employ  $u_{\max}(\vec{\epsilon}) \leq 2.00759$  as a legitimate CR for all  $j \geq 10$  and  $\gamma = 3$ .

In Fig. 12, for  $\gamma = 3$  and  $j = \frac{5}{2}$ , we also plot the largest and second-largest eigenvalues of  $\Lambda(\theta, \phi) = \hat{\eta}(\theta, \phi) \cdot \vec{E}_\gamma$ . There one can perceive that the gap between the eigenvalues is least at eight different  $(\theta, \phi)$  that correspond to  $\{\pm \hat{\eta}_l\}_{l=1}^4$ . The gap at these eight places reduces as  $j$  grows, and it seems to disappear at  $j \rightarrow \infty$ . By the way, such a situation appears in the study of quantum phase transitions. The gap is already very small for  $j = 10$ , and the two eigenvalues are, 586.116 and 585.098, almost equal at  $(\theta_l, \phi_l)$ . In other words, the maximum eigenvalue  $\lambda_m(\theta_l, \phi_l)$  turns almost degenerate for a large quantum number  $j$ , and the degeneracy is a necessary requirement for the allowed region to have a flat face (that has more than one distinct points). Therefore, eight flat faces appear on the boundary  $\partial \mathcal{E}_\gamma^{\text{us}}$  for an odd power  $\gamma \geq 3$ .

Now we take even powers  $\gamma = 4, 6, \dots$  for  $\vec{E}_\gamma$  of (122),

then hyperrectangle (3) becomes

$$\mathcal{H}_\gamma = \begin{cases} [(\frac{1}{2})^\gamma, j^\gamma]^{\times 3} & \text{for a half-integer } j \\ [0, j^\gamma]^{\times 3} & \text{for an integer } j \end{cases}. \quad (129)$$

In the case of  $j = \frac{1}{2}, 1$ , and  $\frac{3}{2}$ , one can compute the mean value  $\langle (J_x)^\gamma \rangle$  from  $\langle J_x^2 \rangle$  by using the Cayley-Hamilton theorem for  $J_x$ , and similarly for the other two operators in  $\vec{E}_\gamma$ . As a result, the numerical range  $\mathcal{E}_\gamma$  of  $\vec{E}_\gamma$ —directly obtained from the numerical range of  $(J_x^2, J_y^2)$  in Sec. V—will be a single point, a triangle, and an elliptical disk for  $j = \frac{1}{2}, 1$ , and  $\frac{3}{2}$ , respectively.

Recall from Sec. V that  $\mathcal{S}_0^2$  and  $\mathcal{S}_1^2$  [stated in (37)] are two mutually orthogonal invariant subspaces of  $J_x^2$  and  $J_y^2$ . Hence, they will also be invariant subspaces of  $\Lambda(\theta, \phi) = \hat{\eta}(\theta, \phi) \cdot \vec{E}_\gamma$  for all even  $\gamma \geq 2$ . Moreover, one can find eigenvectors of  $\Lambda$  in these subspaces like Sec. V. Here also, for every half-integer  $j$ , the maximum eigenvalue  $\lambda_m(\theta, \phi)$  of  $\Lambda(\theta, \phi)$  is at least twofold degenerate in all the directions  $(\theta, \phi)$ .

Now we only focus on  $\gamma = 4$ . The maximum-eigenvalue-kets  $|\pm j\rangle$  and the minimum-eigenvalue-kets  $|\pm \frac{1}{2}\rangle$  or  $|0\rangle$  of  $J_z^4$  provide

$$\begin{aligned} \langle \pm j | (J_{x,y})^4 | \pm j \rangle &= \frac{j(3j-1)}{4} \quad \text{and} \\ \langle \pm \frac{1}{2} | (J_{x,y})^4 | \pm \frac{1}{2} \rangle &= \frac{j(j+1)(6j(j+1)-7)+\frac{23}{8}}{16} \quad \text{or} \quad (130) \\ \langle 0 | (J_{x,y})^4 | 0 \rangle &= \frac{j(j+1)(3j(j+1)-2)}{8}. \end{aligned}$$

One will have similar relations with the extreme-eigenvalue-kets of  $J_x^4$  and  $J_y^4$ . In this way, analogues to (52)–(54), we have six extreme points of the allowed region  $\mathcal{E}_4$ . These points are illustrated in Figs. 13, 15, and 16, where we present  $\mathcal{E}_4$  for  $j = 2, \frac{5}{2}, 3, \frac{7}{2}$ , and 25. Let us analyze these one by one.

In the case of  $j = 2$ , the operator  $\Lambda(\theta_1, \phi_1) = \hat{\eta}_1 \cdot \vec{E}_4$  has only two distinct eigenvalues  $8\sqrt{3}$  and  $6\sqrt{3}$  [for  $\hat{\eta}_1$ , see Table. III]. With the eigenvalues, one can have two parallel supporting hyperplanes whose outward-pointing normals are  $\pm \hat{\eta}_1$  as per (8) and (9). Here the numerical range  $\mathcal{E}_4$  is the convex hull of an ellipse in one of the planes and the three extreme points

$$(16, 1, 1), \quad (1, 16, 1), \quad \text{and} \quad (1, 1, 16) \quad (131)$$

lie in the other plane. The ellipse is specified by the equality in

$$\begin{aligned} \left( \frac{\langle J_x^4 \rangle + \langle J_y^4 \rangle - 16}{8} \right)^2 + \left( \frac{\langle J_x^4 \rangle - \langle J_y^4 \rangle}{8\sqrt{3}} \right)^2 &\leq 1, \quad \text{and} \\ \sqrt{3} \langle \hat{\eta}_1 \cdot \vec{E}_4 \rangle &= \langle J_x^4 \rangle + \langle J_y^4 \rangle + \langle J_z^4 \rangle = 24 \end{aligned} \quad (132)$$

describes its plane. According to (14), the elliptical face  $\mathcal{F}(\theta_1, \phi_1)$  identified by (132) and the triangular face  $\mathcal{F}(\pi - \theta_1, \pi + \phi_1)$  made of the points in (131) are the images of the two sets of eigenstates that are associated with the maximum and minimum eigenvalues of  $\hat{\eta}_1 \cdot \vec{E}_4$ .

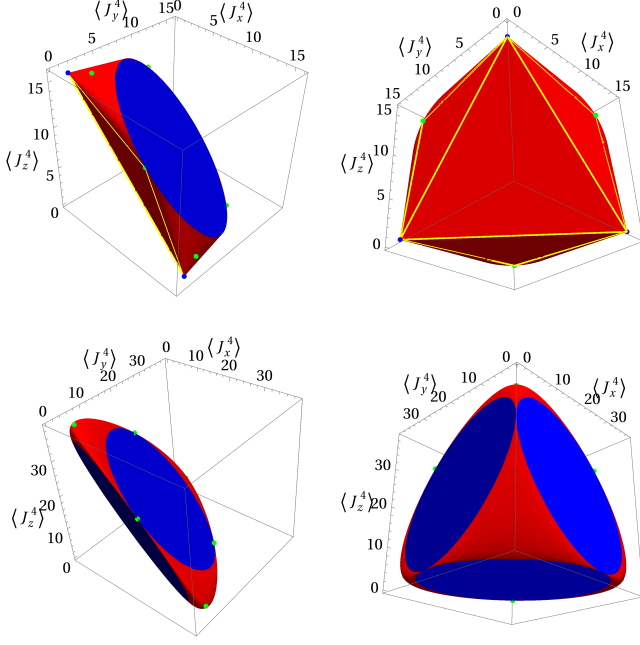


FIG. 13. (Color online) The red convex bodies in the top and bottom rows are the allowed regions  $\mathcal{E}_4$  for  $\vec{E}_4$  [in (122)] when  $j = 2$  and  $j = \frac{5}{2}$ , respectively. In each row, the same region is shown from different viewpoints. In all the pictures, the green points come from the extreme-eigenvalue-states of  $J_x^4$ ,  $J_y^4$ , and  $J_z^4$  as per (130). In the case of  $j = 2$ , the top row, the three blue points and the blue elliptical disk represent (131) and (132), respectively. The blue points and boundary of the disk form the set of all extreme points of  $\mathcal{E}_4$ . Furthermore, there are four triangles—illustrated by the yellow lines—on the boundary  $\partial\mathcal{E}_4$ , and their vertices are the blue points and the three green points  $(0, 12, 12)$ ,  $(12, 0, 12)$ , and  $(12, 12, 0)$ . In the case of  $j = \frac{5}{2}$ , the bottom row, the boundary  $\partial\mathcal{E}_4$  has four elliptical disks painted in blue color.

In other words, the conditions in (132) are only met by the maximum-eigenvalue-states of  $\hat{\eta}_1 \cdot \vec{E}_4$ . One can see in Fig. 13 that there are three more triangles on the boundary  $\partial\mathcal{E}_4$  whose outward normals are  $\vec{\eta} = -(1, 1, 7)$  and the two obtained by permuting the entries in  $\vec{\eta}$ . The lowest eigenvalue 24 of  $J_x^4 + J_y^4 + 7J_z^4$  is threefold degenerate, hence  $\mathcal{E}_4$  gets a triangular face in the direction of  $\vec{\eta}$ .

For  $j = 2$ , there is not a single eigenvalue of  $\Lambda(\theta, \phi)$  that stays the largest throughout the parameter space  $[0, \pi] \times [0, 2\pi]$  of  $\theta$  and  $\phi$ . Four distinct eigenvalues  $\lambda(\theta, \phi)$  compete and cross each other, known as the *level crossing*, in different parts of the parameter space as shown in Fig. 14. There we highlight points one in red and four in black color—that correspond to the ellipse and triangles—where the maximum eigenvalue  $\lambda_m(\theta, \phi)$  becomes double and triple degenerate, respectively.

Next, in the case of  $j = \frac{5}{2}$ ,  $\Lambda(\theta, \phi)$  has three distinct eigenvalues, and each one is double degenerate for all  $\theta$  and  $\phi$ . Although one of the eigenvalues stays the largest in the whole parameter space  $[0, \pi] \times [0, 2\pi]$ , it meets

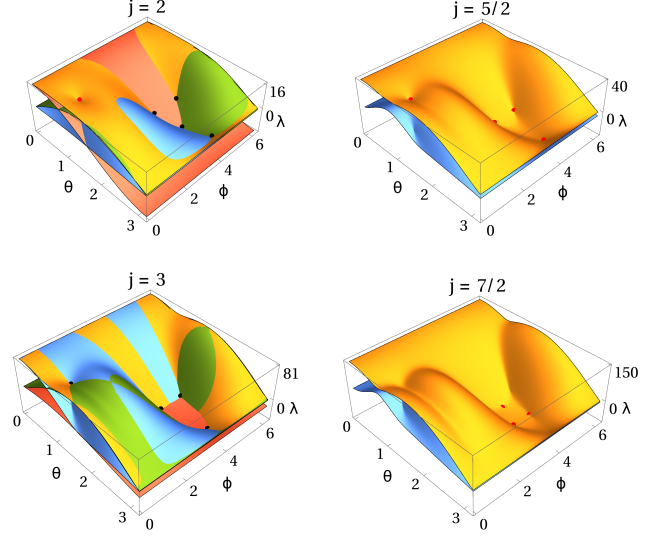


FIG. 14. (Color online) For  $j = 3, \dots, \frac{7}{2}$ , we plot different eigenvalues of  $\Lambda(\theta, \phi) = \hat{\eta}(\theta, \phi) \cdot \vec{E}_4$  in separate colors on the parameter space  $[0, \pi] \times [0, 2\pi]$ .  $\vec{E}_{\gamma=4}$  is given in (122). One can recognize the maximum eigenvalue  $\lambda_m(\theta, \phi)$  from the top view. In the case of integer  $j$ -values, one out of four eigenvalues of  $\Lambda$  dominates in a region of the parameter space, and one can observe the level crossings in the two left-hand-side pictures. There one can easily spot points where—three colors join— $\lambda_m$  becomes threefold degenerate, some of them are indicated by black dots. The black dots correspond to the triangular faces of the allowed regions  $\mathcal{E}_4$  in Figs. 13 and 15. Whereas, in the case of  $j = \frac{5}{2}$  and  $j = \frac{7}{2}$ , the largest and the second-largest eigenvalues meet only at four and six individual points, respectively. These four and three out of the six points are marked in red color. The red dots in all the above pictures have link with the elliptical faces of  $\mathcal{E}_4$  in Figs. 13 and 15.

the second-largest eigenvalue at four different  $(\theta, \phi)$ . In other words, the maximum eigenvalue  $\lambda_m(\theta, \phi)$  becomes fourfold degenerate only at these 4 points featured in red color in Fig. 14. Consequently, we observe four flat faces [see Fig. 13 for  $j = \frac{5}{2}$ ] on the boundary of the numerical range  $\mathcal{E}_4$ . All these faces are elliptical in shape. One of these is described by

$$\left( \frac{\langle J_x^4 \rangle + \langle J_y^4 \rangle - \frac{803}{24}}{\frac{50}{3}} \right)^2 + \left( \frac{\langle J_x^4 \rangle - \langle J_y^4 \rangle}{\frac{50}{\sqrt{3}}} \right)^2 \leq 1 \text{ and} \\ \sqrt{3} \langle \hat{\eta}_1 \cdot \vec{E}_4 \rangle = \langle J_x^4 \rangle + \langle J_y^4 \rangle + \langle J_z^4 \rangle = \frac{803}{16}, \quad (133)$$

and another is by

$$\left( \frac{\langle J_x^4 \rangle + \langle J_y^4 \rangle - 39.7056}{10.4194} \right)^2 + \left( \frac{\langle J_x^4 \rangle - \langle J_y^4 \rangle}{30.7721} \right)^2 \leq 1 \text{ and} \\ \langle J_x^4 \rangle + \langle J_y^4 \rangle + 4.076923 \langle J_z^4 \rangle = 50.37981. \quad (134)$$

Like (132), the second equations in (133) and (134) identify the tangent hyperplanes of  $\mathcal{E}_4$  in which the associated ellipses reside. One can check that only

the eigenstates attached to the biggest eigenvalue  $\frac{803}{16\sqrt{3}}$  of  $\hat{\eta}_1 \cdot \vec{E}_4$  and  $-50.37981$  of  $-(J_x^4 + J_y^4 + 4.076923 J_z^4)$  satisfy (133) and (134), respectively. Since the operator  $J_x^4 + 4.076923 J_y^4 + J_z^4$  is unitarily equivalent to  $J_x^4 + J_y^4 + 4.076923 J_z^4$ , by the cyclic permutations of  $\{x, y, z\}$  in (134) one can obtain relations that characterize the two remaining elliptical faces of the allowed region. Note that numbers such as 4.076923 are rounded to a few decimal places.

Next, we take  $j = 3$ , where the allowed region is the convex hull of three intersecting ellipses and the point  $(16, 16, 16)$  that is marked in blue color in Fig. 15. There one can notice blue curves, which are the parts—of the ellipses—that lie on the boundary  $\partial\mathcal{E}_4$ . The remaining (unseen) parts of ellipses fall inside the numerical range  $\mathcal{E}_4$ . One of the ellipses can be characterized by the equality in

$$\left(\frac{\langle J_x^4 \rangle + \langle J_y^4 \rangle - 82}{20}\right)^2 + \left(\frac{\langle J_x^4 \rangle - \langle J_y^4 \rangle}{20\sqrt{15}}\right)^2 \leq 1 \text{ and} \\ \langle 2J_x^4 + 2J_y^4 + 5J_z^4 \rangle = 204, \quad (135)$$

and the other two by permuting  $\{x, y, z\}$  in these relations. The second equation in (135) describes the plane where the ellipse stays. Note that this plane is not a supporting plane of  $\mathcal{E}_4$  but it passes through the allowed region. Moreover the eigenvalue 204 of  $2J_x^4 + 2J_y^4 + 5J_z^4$  is not an extreme eigenvalue.

Like  $j = 2$ , the level crossings occur also in the case of  $j = 3$ . In Fig. 14, we mark four points in black color where  $\lambda_m(\theta, \phi)$  turns triple degenerate. In these four directions— $\hat{\eta}_1, \vec{\eta} = -(1, 1, 3.55739)$ , and the two obtained by permuting the entries in  $\vec{\eta}$ — $\mathcal{E}_4$  has four triangular faces [see Fig. 15]. One can check that the biggest eigenvalues  $34\sqrt{3}$  and  $-88.9183$  of the operators  $\hat{\eta}_1 \cdot \vec{E}_4$  [for  $\hat{\eta}_1$ , see Table III] and  $\vec{\eta} \cdot \vec{E}_4$  are threefold degenerate, and the associated eigenstates generate the triangular faces.

Now we move to  $j = \frac{7}{2}$ , where each eigenvalue of  $\Lambda(\theta, \phi)$  is at least double degenerate, and there are at most four distinct eigenvalues over the whole parameter space. Its maximum eigenvalue  $\lambda_m(\theta, \phi)$  becomes fourfold degenerate at six different  $(\theta, \phi)$ , and three of them are indicated by the red-dots in Fig. 14. The allowed region  $\mathcal{E}_4$  has three elliptical faces in the directions  $(\theta, \phi)$  associated with the red-dots. One of the faces is characterized by

$$\left(\frac{\langle J_x^4 \rangle + \langle J_y^4 \rangle - 36.96675}{21.71172}\right)^2 + \left(\frac{\langle J_x^4 \rangle - \langle J_y^4 \rangle}{20.731196}\right)^2 \leq 1 \text{ and} \\ \langle J_x^4 + J_y^4 + 0.3890792 J_z^4 \rangle = 71.8851, \quad (136)$$

and the remaining two by the permutations of  $\{x, y, z\}$  in these relations. Only the eigenstates associated with the smallest eigenvalue 71.8851 of  $J_x^4 + J_y^4 + 0.3890792 J_z^4$  meet all the conditions in (136).

Finally, after the uniform scaling (85), we present the allowed  $\mathcal{E}_4^{\text{us}}$  in Fig. 16 in the case of a large quantum

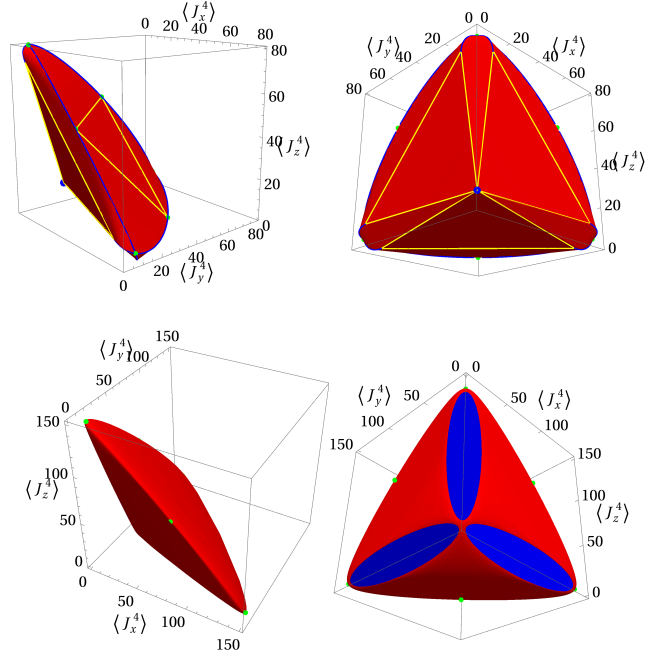


FIG. 15. (Color online) The red convex bodies in the top and bottom rows depict the numerical range  $\mathcal{E}_4$  of  $\vec{E}_{\gamma=4}$  in the case of quantum numbers  $j = 3$  and  $j = \frac{7}{2}$ , respectively. Like Fig. 13, each row carries the same  $\mathcal{E}_4$ . In the top-pictures, the blue curves are parts of three ellipses, the blue point is  $16(1, 1, 1)$ , and the yellow lines constitute four different triangles on the boundary  $\partial\mathcal{E}_4$ . The ellipses cross each other at the three green points, such as  $(81, 6, 6)$ , that come from the maximum-eigenvalue states of  $J_x^4$ ,  $J_y^4$ , and  $J_z^4$  [see (130)]. The blue point is a vertex of the triangles, and the other vertices—fall on the ellipses—are  $(73.6649, 1.24132, 10.8375)$ , the green point  $(51, 51, 0)$ , and the rest obtained by the permutations of their entries. In the bottom-pictures, for  $j = \frac{7}{2}$ , one can see three elliptical disks in blue color on the boundary of  $\mathcal{E}_4$ . The vector  $-(1, 1, 0.3890792)$  is an outward normal to the supporting hyperplane in which one of the disks resides.

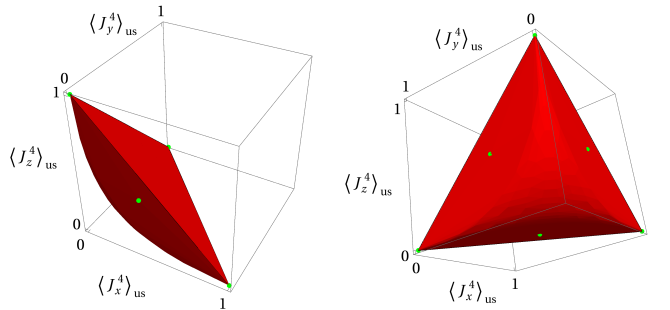


FIG. 16. (color online) For  $j = 25$ , the numerical range  $\mathcal{E}_4^{\text{us}}$  of  $\frac{1}{j^4}\vec{E}_4$  is shown through—the red convex body—two different directions. Here we present the mean values  $\langle J_x^4 \rangle_{\text{us}} := \langle (\frac{J_x}{j})^4 \rangle$ ,  $\langle J_y^4 \rangle_{\text{us}}$ , and  $\langle J_z^4 \rangle_{\text{us}}$  after the uniform scaling (85). As per (130), here two of the green points are  $(0.001184, 0.001184, 1)$  and  $(0.405184, 0.405184, 0)$ .

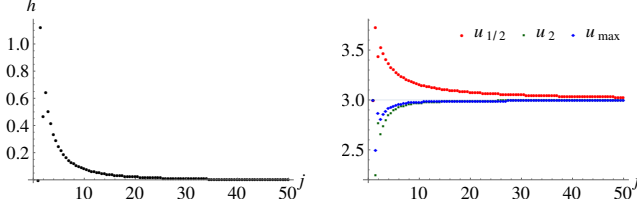


FIG. 17. Like Fig. 6, the plots exhibit the lower bounds of  $h(\bar{\epsilon})$  and  $u_{1/2}(\bar{\epsilon})$  and the upper bounds of  $u_2(\bar{\epsilon})$  and  $u_{\max}(\bar{\epsilon})$  on  $\mathcal{E}_4$  as functions of the quantum number  $j = 1, \frac{3}{2}, \dots, 50$ .

number  $j = 25$ . One can notice a curved surface at the boundary  $\partial\mathcal{E}_4^{\text{us}}$ , which is predicted by the quantum de Finetti theorem in the limit  $j \rightarrow \infty$  [see the next section]. If we apply this limit to the mean values in (130) then we realize

$$\lim_{j \rightarrow \infty} \frac{1}{j^4} \langle \pm j | \vec{E}_4 | \pm j \rangle = (0, 0, 1) \quad \text{and} \quad (137)$$

$$\lim_{j \rightarrow \infty} \frac{1}{j^4} \langle \pm \frac{1}{2} | \vec{E}_4 | \pm \frac{1}{2} \rangle = (\frac{3}{8}, \frac{3}{8}, 0) = \lim_{j \rightarrow \infty} \frac{1}{j^4} \langle 0 | \vec{E}_4 | 0 \rangle.$$

One can recognize that two of the green points in Fig. 16 are indeed close to  $(\frac{3}{8}, \frac{3}{8}, 0)$  and a corner  $(0, 0, 1)$  of the hypercube  $[0, 1]^3 = \lim_{j \rightarrow \infty} \frac{1}{j^4} \mathcal{H}_4$  [for  $\mathcal{H}_{\gamma=4}$ , see (129)].

Like before, according to (15)–(19), here we build our combined uncertainty  $\{h, u_{1/2}\}$  and certainty  $\{u_2, u_{\max}\}$  functions of the mean vector  $\bar{\epsilon} = \langle \vec{E}_4 \rangle$ . Then, for every  $j = 1, \frac{3}{2}, \dots, 50$ , we compute values of these functions on a finite set of boundary points of  $\mathcal{E}_4$  and consider the minimum values of  $h, u_{1/2}$  as their lower bounds  $\mathfrak{h}, \mathfrak{u}_{1/2}$  and the maximum values of  $u_2, u_{\max}$  as their upper bounds  $\mathfrak{u}_2, \mathfrak{u}_{\max}$ . With a bound one has a UR or CR. We plot these bounds in Fig. 17 and record them in Appendix . These bounds are accurate up to a first few decimal places, and one can improve them by taking more boundary points or adopting a procedure such as reported in [1].

The uncertainty and certainty measures reach their extreme values  $\{\mathfrak{h}, \mathfrak{u}_{1/2}, \mathfrak{u}_2, \mathfrak{u}_{\max}\}$  in those parts of the boundary which are close to the corners of hyperrectangle (129). As these parts move toward the corners [see Figs. 13, 15, and 16] as  $j$  grows, the lower bounds decrease and the upper bounds increase [see Fig. 17]. In the limit  $j \rightarrow \infty$ , the allowed region will share three vertices of the hyperrectangle [see (137)] and  $\mathfrak{h}, \mathfrak{u}_{1/2}, \mathfrak{u}_2$ , and  $\mathfrak{u}_{\max}$  will hit their trivial values 0, 3, 3, and 3, respectively.

## VIII. N-QUBIT SYSTEM

In this section, one by one, we consider (122) and

$$\begin{aligned} \vec{E}_\gamma &= (A_{1,\gamma}, A_{2,\gamma}, A_{3,\gamma}), \quad \text{where} \\ A_{1,\gamma} &:= (J_x)^\gamma (J_z)^\gamma + (J_z)^\gamma (J_x)^\gamma, \\ A_{2,\gamma} &:= (J_y)^\gamma (J_z)^\gamma + (J_z)^\gamma (J_y)^\gamma, \quad \text{and} \\ A_{3,\gamma} &:= (J_x)^\gamma (J_y)^\gamma + (J_y)^\gamma (J_x)^\gamma. \end{aligned} \quad (138)$$

As before  $\gamma$  is a finite positive integer. Here, in both the cases, the main task is to achieve the allowed region for  $\vec{E}_\gamma$  in the limit  $j \rightarrow \infty$ . To complete the task, we take a system of  $N$  spin- $\frac{1}{2}$  particles (qubits), and applying the famous quantum de Finetti theorem [30, 31] in the limit  $N \rightarrow \infty$ .

Let us begin with the vector Pauli operator  $\vec{\sigma}_i = (\mathbf{X}_i, \mathbf{Y}_i, \mathbf{Z}_i)$  that acts on  $i$ th qubit's Hilbert space, and

$$\vec{\mathbf{J}} = (\mathbf{J}_x, \mathbf{J}_y, \mathbf{J}_z) := \frac{1}{2} \sum_{i=1}^N \vec{\sigma}_i \quad (139)$$

is the total angular momentum vector operator on  $N$ -qubit Hilbert space  $\mathcal{H}_2^{\otimes N}$ . The operator  $\mathbf{J}^2 = \vec{\mathbf{J}} \cdot \vec{\mathbf{J}}$  has eigenvalues  $j(j+1)$  where  $j = \frac{N}{2}, \frac{N}{2}-1, \dots, 0$  or  $\frac{1}{2}$  when  $N$  is an even or odd number. In an eigenbasis of (degenerate operator)  $\mathbf{J}^2$ , the components of  $\vec{\mathbf{J}}$  reveal their block-diagonal forms, for instance,

$$\mathbf{J}_z = \frac{1}{2} \sum_{i=1}^N \mathbf{Z}_i = J_z^{(\frac{N}{2})} \oplus J_z^{(\frac{N}{2}-1)} \oplus \dots \oplus J_z^{(0 \text{ or } \frac{1}{2})}, \quad (140)$$

where  $\oplus J_z^{(\frac{N}{2}-1)}$  denotes the direct sum of multiple copies of the angular momentum operator  $J_z$  corresponding to the quantum number  $j = \frac{N}{2} - 1$ , and so on. There is only one copy of  $J_z^{(\frac{N}{2})}$  in the direct sum. For more details, we point the reader to [37, 39]. Polynomials of  $\mathbf{J}_x, \mathbf{J}_y$ , and  $\mathbf{J}_z$  such as

$$(\mathbf{J}_x)^\gamma, (\mathbf{J}_y)^\gamma, (\mathbf{J}_z)^\gamma, \quad (141)$$

$$\begin{aligned} \mathbf{A}_{1,\gamma} &:= (\mathbf{J}_x)^\gamma (\mathbf{J}_z)^\gamma + (\mathbf{J}_z)^\gamma (\mathbf{J}_x)^\gamma, \\ \mathbf{A}_{2,\gamma} &:= (\mathbf{J}_y)^\gamma (\mathbf{J}_z)^\gamma + (\mathbf{J}_z)^\gamma (\mathbf{J}_y)^\gamma, \quad \text{and} \\ \mathbf{A}_{3,\gamma} &:= (\mathbf{J}_x)^\gamma (\mathbf{J}_y)^\gamma + (\mathbf{J}_y)^\gamma (\mathbf{J}_x)^\gamma \end{aligned} \quad (142)$$

carry the same block-diagonal structure.

*A side remark:* The numerical range of a direct sum of operators, say,  $(A \oplus A', B \oplus B')$  is the convex hull of the numerical ranges of  $(A, B)$  and  $(A', B')$  provided  $A$  and  $B$  act on the same Hilbert space, and similarly for  $A'$  and  $B'$  [11, 40]. Hence, we can express the numerical range of  $(\mathbf{J}_x^2, \mathbf{J}_y^2)$  as

$$\mathcal{E}(\mathbf{J}_x^2, \mathbf{J}_y^2) = \text{Conv} \left\{ \bigcup_{j=0 \text{ or } \frac{1}{2}}^{\frac{N}{2}} \mathcal{E}((J_x^{(j)})^2, (J_y^{(j)})^2) \right\}. \quad (143)$$



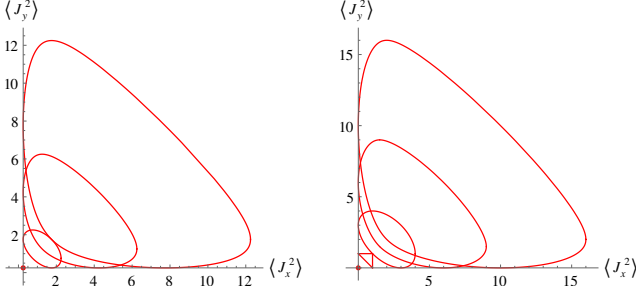


FIG. 18. The left and right portrayals are for  $N = 7$  and  $N = 8$  number of qudits. The red closed curves and the red points are the boundaries of  $\mathcal{E}((J_x^{(j)})^2, (J_y^{(j)})^2)$  for different  $j = \frac{N}{2}, \frac{N}{2} - 1, \dots, 0$  or  $\frac{1}{2}$ . The curves are taken from Figs. 2–5.

By looking at Fig. 18 one can tell, at least up to  $N = 8$ , that  $\mathcal{E}(\mathbf{J}_x^2, \mathbf{J}_y^2)$  is the convex hull of  $\mathcal{E}((J_x^{(N/2)})^2, (J_y^{(N/2)})^2)$  and the point  $(0, 0)$  or  $(\frac{1}{4}, \frac{1}{4})$  when  $N$  is an even or odd number. The point  $(0, 0)$  is the allowed region of  $(J_x^2, J_y^2)$  when the quantum number  $j = 0$ . Since  $(0, 0)$  or  $(\frac{1}{4}, \frac{1}{4})$  is a vertex of the hyperrectangle (3) in the case of  $\mathbf{J}_x^2$  and  $\mathbf{J}_y^2$ , we do not get a nontrivial UR and CR for them based on the procedure given in Sec. II. Whereas, in the case of anticommutators (138) and (142), we observe a nested sequence of regions and thus  $\mathcal{E}(\mathbf{A}_{1,1}, \mathbf{A}_{2,1}, \mathbf{A}_{3,1}) = \mathcal{E}(A_{1,1}^{(N/2)}, A_{2,1}^{(N/2)}, A_{3,1}^{(N/2)})$ , which we have checked up to  $N = 50$ .

Now coming back to our main task, we only need the eigenspace of  $\mathbf{J}^2$  that corresponds to the largest quantum number  $j = \frac{N}{2}$ . Since  $\mathbf{J}_z$  commutes with  $\mathbf{J}^2$ , we choose their common eigenkets, known as the Dicke kets [37, 39],

$$|j, m\rangle = \frac{1}{(j-m)!} \frac{1}{\sqrt{\binom{2j}{j-m}}} (\mathbf{J}_-)^{j-m} |+\frac{1}{2}\rangle^{\otimes N}, \quad \text{where} \quad (144)$$

$$\mathbf{J}_\pm = \mathbf{J}_x \pm i\mathbf{J}_y, \quad m \in \{j, j-1, \dots, -j\}, \quad j = \frac{N}{2}, \quad (145)$$

$\binom{2j}{j-m}$  is the binomial coefficient, and  $|+\frac{1}{2}\rangle = \mathbf{Z}|+\frac{1}{2}\rangle$ . Dicke kets satisfy the eigenvalue equations

$$\mathbf{J}^2 |j, m\rangle = j(j+1) |j, m\rangle, \quad (146)$$

$$\mathbf{J}_z |j, m\rangle = m |j, m\rangle, \quad \text{and} \quad (147)$$

$$U_P |j, m\rangle = |j, m\rangle \quad \text{for all } P, \quad (148)$$

where  $U_P$  is the unitary operator associated with a permutation  $P$  of qubits' indices  $\{1, \dots, N\}$ . Equation (147) is same as (24). Due to Eq. (148), all Dicke kets (144) have the Bose-Einstein symmetry [31], and they form an orthonormal basis of the symmetric subspace

$$\text{Sym}(\mathcal{H}_2^{\otimes N}) := \text{span}\{| \frac{N}{2}, m \rangle \mid m = \frac{N}{2}, \dots, -\frac{N}{2} \} \quad (149)$$

of the  $N$ -qubit Hilbert space. In short,  $\text{Sym}(\mathcal{H}_2^{\otimes N})$  is the eigenspace  $\mathbf{J}^2$  and  $U_P$  for all  $P$ 's.

The  $N$ -qubit operators  $(\mathbf{J}_x, \mathbf{J}_y, \mathbf{J}_z)$  restricted to this subspace behave as  $(J_x, J_y, J_z)$  [see (22)–(25)], that is,

$$\mathbf{J}|_{\text{Sym}(\mathcal{H}_2^{\otimes N})} \equiv \vec{J} = (J_x, J_y, J_z) \quad \text{on } \mathcal{H}_d, \quad (150)$$

where the dimension  $d = 2j + 1 = N + 1$ . We put the same restriction, (150), on the  $N$ -qubit operators in (141) and (142). Now let us form a set

$$\Omega_{\text{BE}} = \text{Conv}\left\{ |\psi\rangle\langle\psi| \mid |\psi\rangle \in \text{Sym}(\mathcal{H}_2^{\otimes N}) \right\} \quad (151)$$

of all those  $N$ -qubit density operators whose supports lie in symmetric subspace (149).  $\Omega_{\text{BE}}$  is analogous to the state space—mentioned in (2) for a  $d$ -level system—but here every state also has the Bose-Einstein symmetry  $U_P \rho = \rho \in \Omega_{\text{BE}}$  as described in [31].

Here we quote a special case of the celebrated quantum de Finetti theorem [30, 31]:

In the limit  $N \rightarrow \infty$ ,  $\Omega_{\text{BE}}$  becomes a Choquet simplex, extreme points of which are pure product states. (152)

In a simplex, every point has a unique decomposition in terms of its extreme points, and the word “pure” in (152) is attributed to the Bose-Einstein symmetry. Every pure qubit's state

$$\begin{aligned} \rho &= \frac{1}{2}(1 + \vec{r} \cdot \vec{\sigma}), \quad \text{where} \\ \vec{r} &= \langle \vec{\sigma} \rangle = (x, y, z) = (\sin \mu \cos \nu, \sin \mu \sin \nu, \cos \mu), \\ \mu &\in [0, \pi], \quad \text{and} \quad \nu \in [0, 2\pi), \end{aligned} \quad (153)$$

provides a symmetric product state  $\rho^{\otimes N}$  that is an extreme point of  $\Omega_{\text{BE}}$  for all  $N = 1, 2, \dots$ , particularly, in the limit  $N \rightarrow \infty$  thanks to (152). Now we can present our allowed regions.

For a finite  $N$ , one can realize

$$\begin{aligned} (2\mathbf{J}_x)^\gamma &= \sum_{i_1 \neq i_2 \neq \dots \neq i_\gamma} \mathbf{X}_{i_1} \mathbf{X}_{i_2} \dots \mathbf{X}_{i_\gamma} + \text{Rest}, \\ \left\langle \left( \frac{\mathbf{J}_x}{2} \right)^\gamma \right\rangle_{\rho^{\otimes N}} &= \frac{1}{N^\gamma} \frac{N!}{(N-\gamma)!} x^\gamma + \langle \frac{\text{Rest}}{N^\gamma} \rangle_{\rho^{\otimes N}}, \end{aligned} \quad (154)$$

where  $i_1, \dots, i_\gamma$  are qubits' indices and  $\mathbf{x} = \langle \mathbf{X} \rangle_\rho$  [see (153)]. Then we take the limit and obtain

$$\begin{aligned} \lim_{N \rightarrow \infty} \left\langle \left( \frac{\mathbf{J}_x}{2} \right)^\gamma \right\rangle_{\rho^{\otimes N}} &= x^\gamma, \quad \text{likewise} \\ \lim_{N \rightarrow \infty} \left\langle \left( \frac{\mathbf{J}_y}{2} \right)^\gamma \right\rangle_{\rho^{\otimes N}} &= y^\gamma \quad \text{and} \\ \lim_{N \rightarrow \infty} \left\langle \left( \frac{\mathbf{J}_z}{2} \right)^\gamma \right\rangle_{\rho^{\otimes N}} &= z^\gamma. \end{aligned} \quad (155)$$

In Fig. 19, we plot

$$\begin{aligned} \mathcal{J}_\gamma &= \{ (x^\gamma, y^\gamma, z^\gamma) \mid 0 \leq \mu \leq \pi \text{ and } 0 \leq \nu < 2\pi \} \\ &= \{ (\mathbf{x}, \mathbf{y}, \mathbf{z}) \in \mathcal{H}^{\text{us}} \mid \mathbf{x}^{\frac{2}{\gamma}} + \mathbf{y}^{\frac{2}{\gamma}} + \mathbf{z}^{\frac{2}{\gamma}} = 1 \} \end{aligned} \quad (156)$$

for  $\gamma = 1, \dots, 4$ . The hyperrectangle  $\mathcal{H}^{\text{us}}$  in (156) is  $[0, 1]^{\times 3}$  and  $[-1, 1]^{\times 3}$  for an even and odd  $\gamma$ , and  $\mathbf{x} = x^\gamma$  and so on. Basically,  $\mathcal{J}_\gamma$  is an image of the Bloch sphere, which is identified with  $x^2 + y^2 + z^2 = 1$ . In the case of  $\gamma > 4$ , the shape of  $\mathcal{J}_\gamma$  is same as  $\mathcal{J}_3$  and  $\mathcal{J}_4$  for an odd and even  $\gamma$ , respectively.

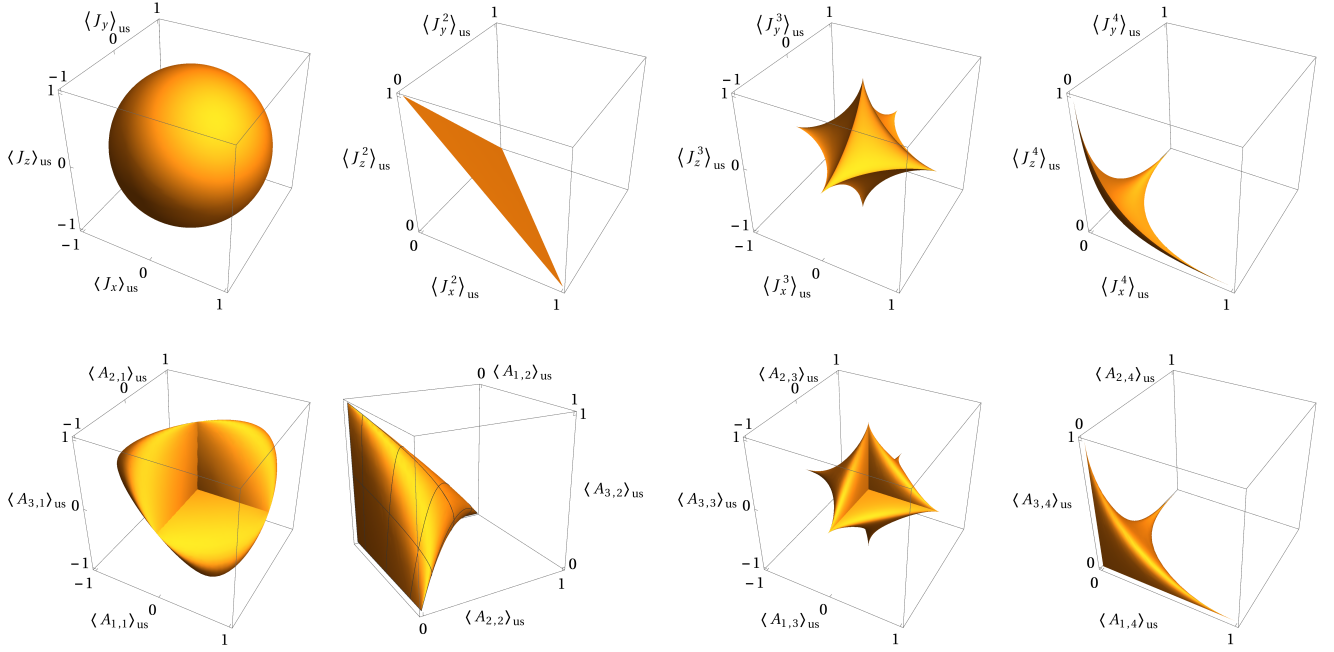


FIG. 19. In top and bottom rows, the parametric plots of  $\mathcal{J}_\gamma$  of (156) and  $\mathcal{A}_\gamma$  of (162) are displayed sequentially for  $\gamma = 1, \dots, 4$ . The convex hull of  $\mathcal{J}_\gamma$  and  $\mathcal{A}_\gamma$  are the numerical range of  $((\frac{J_x}{j})^\gamma, (\frac{J_y}{j})^\gamma, (\frac{J_z}{j})^\gamma)$  and  $(\frac{A_{1,\gamma}}{a_{M,\gamma}}, \frac{A_{2,\gamma}}{a_{M,\gamma}}, \frac{A_{3,\gamma}}{a_{M,\gamma}})$ , respectively, in the limit  $j \rightarrow \infty$ . Here  $\langle J_x^\gamma \rangle_{\text{us}}$  and  $\langle A_{1,\gamma} \rangle_{\text{us}}$  represent  $\langle (\frac{J_x}{j})^\gamma \rangle$  and  $\langle \frac{A_{1,\gamma}}{a_{M,\gamma}} \rangle$ , correspondingly.

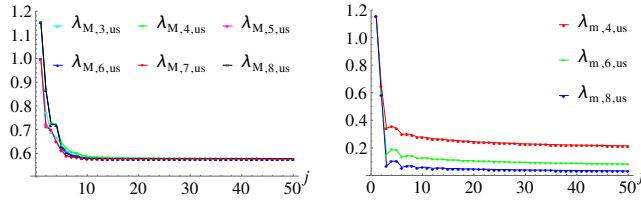


FIG. 20. On the left-hand-side, we present list-line-plots of  $\{\lambda_{M,\gamma,\text{us}}\}_{j=1}^{50}$  for  $\gamma = 3, \dots, 8$ .  $\lambda_{M,\gamma,\text{us}}$  denotes  $\frac{\lambda_{M,\gamma}(\theta_1, \phi_1)}{j^\gamma}$ , where  $\lambda_{M,\gamma}(\theta_1, \phi_1)$  is the maximum eigenvalue of  $\hat{n}_1 \cdot \vec{E}_\gamma$ . The unit vector  $\hat{n}_1$  and the vector operator  $\vec{E}_\gamma$  are given in Table III and (122), correspondingly. On the right-hand-side, we show list-line-plots of  $\{\lambda_{m,\gamma,\text{us}}\}_{j=1}^{50}$  for  $\gamma = 4, 6, 8$ , where  $\lambda_{m,\gamma,\text{us}} = \frac{\lambda_{m,\gamma}(\theta_1, \phi_1)}{j^\gamma}$ , and  $\lambda_{m,\gamma}(\theta_1, \phi_1)$  is the minimum eigenvalue of  $\hat{n}_1 \cdot \vec{E}_\gamma$ .

Since  $\Omega_{\text{BE}}$  is the convex hull of pure product states as  $\frac{N}{2} = j \rightarrow \infty$  [see (151) and (152)], the numerical range  $\mathcal{E}_\gamma^{\text{us}}$  of  $\frac{1}{j^\gamma} \vec{E}_\gamma$  [ $\vec{E}_\gamma$  is given in (122)] is the convex hull of  $\mathcal{J}_\gamma$  in that limit. For  $\gamma = 1$  and  $\gamma = 2$ ,  $\mathcal{E}$  is the unit ball and the triangle, respectively, as reported in Secs. III and V as well as in [10, 15]. For an odd and even  $\gamma > 1$ , the

allowed region is

$$\begin{aligned} \mathcal{E}_\gamma^{\text{us}} &= \text{Conv}\{(\pm 1, 0, 0), (0, \pm 1, 0), (0, 0, \pm 1)\} \quad \text{and} \\ \mathcal{E}_\gamma^{\text{us}} &= \{(x, y, z) \in [0, 1]^{\times 3} \mid 1 \leq x^{\frac{2}{\gamma}} + y^{\frac{2}{\gamma}} + z^{\frac{2}{\gamma}} \text{ and} \\ &\quad x + y + z \leq 1\}, \end{aligned} \quad (157)$$

respectively. It means that, in the case of every odd power  $\gamma > 1$ ,  $\mathcal{E}_\gamma^{\text{us}}$  is the octahedron, and tight URs and CRs are listed in (125)–(128). In CR (128), recall that  $u_{\text{max}}$  approaches 2 as  $j \rightarrow \infty$ . While, in the case of an even power  $\gamma$ , three corners of the hyperrectangle  $\mathcal{H}^{\text{us}} = [0, 1]^{\times 3}$  lie in the numerical range  $\mathcal{E}_\gamma^{\text{us}}$ , therefore we do not get a non-trivial UR or CR for  $\frac{1}{j^\gamma} \vec{E}_\gamma$  [for a justification, see the last two paragraphs in Sec. II].

Taking the unit vector  $\hat{n}_1$  and  $\vec{E}_\gamma$  from Table III and (122), respectively, we find the extreme eigenvalues of the operator  $\hat{n}_1 \cdot \vec{E}_\gamma$  for  $j = 1, \dots, 50$  and  $\gamma = 3, \dots, 8$ . With the largest  $\lambda_{M,\gamma}(\theta_1, \phi_1)$  and smallest  $\lambda_{m,\gamma}(\theta_1, \phi_1)$  eigenvalues one can draw two parallel supporting hyperplanes (9) of  $\mathcal{E}_\gamma^{\text{us}}$  whose outward normal vectors are  $\pm \hat{n}_1$ . We plot the eigenvalues in Fig. 20. Since  $\lambda_{m,\gamma} = -\lambda_{M,\gamma}$  for an odd power  $\gamma$ , we present  $\lambda_{m,\gamma}$  for even  $\gamma$ 's. The plots suggest

$$\begin{aligned} \lim_{j \rightarrow \infty} \frac{\lambda_{M,\gamma}(\theta_1, \phi_1)}{j^\gamma} &= \frac{1}{\sqrt{3}} \quad \text{for } \gamma > 1 \quad \text{and} \\ \lim_{j \rightarrow \infty} \frac{\lambda_{m,\gamma}(\theta_1, \phi_1)}{j^\gamma} &= \frac{1}{\sqrt{3}} \frac{1}{3^{\frac{\gamma}{2}-1}} \quad \text{for an even } \gamma > 1, \end{aligned} \quad (158)$$

which agree with what is achieved by applying the quantum de Finetti theorem on a  $N$ -qubit system.



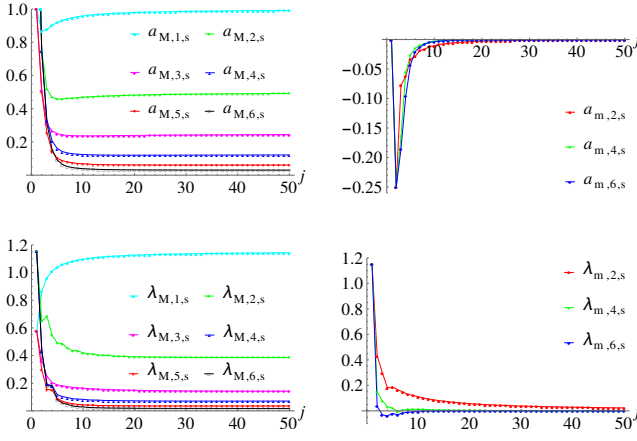


FIG. 21. We numerically compute  $a_{M,\gamma,s}$ ,  $a_{m,\gamma,s}$ ,  $\lambda_{M,\gamma,s}$ , and  $\lambda_{m,\gamma,s}$  for  $j = 1, 2, \dots, 50$  and  $\gamma = 1, \dots, 6$ , and show their list-line-plots here.  $a_{M,\gamma,s}$  and  $a_{m,\gamma,s}$  symbolize  $\frac{a_{M,\gamma}}{j^{2\gamma}}$  and  $\frac{a_{m,\gamma}}{j^{2\gamma}}$ , respectively, where  $a_{M,\gamma}$  and  $a_{m,\gamma}$  are the maximum and minimum characteristic values of the anticommutators in (138). Likewise,  $\lambda_{M,\gamma,s}$  and  $\lambda_{m,\gamma,s}$  express  $\frac{\lambda_{M,\gamma}(\theta_1, \phi_1)}{j^{2\gamma}}$  and  $\frac{\lambda_{m,\gamma}(\theta_1, \phi_1)}{j^{2\gamma}}$ , respectively, where  $\lambda_{M,\gamma}(\theta_1, \phi_1)$  and  $\lambda_{m,\gamma}(\theta_1, \phi_1)$  are the largest and smallest eigenvalues of the operator  $\hat{\eta}_1 \cdot \vec{E}_\gamma$ . The unit vector  $\hat{\eta}_1$  and the vector operator  $\vec{E}_\gamma$  are registered in Table III and (138), correspondingly.

Now we move to our second example: the anticommutators from (138) and (142). Like (154) and (155), first we acquire

$$2^{2\gamma} \mathbf{A}_{1,\gamma} = \sum_{i_1 \neq \dots \neq k_\gamma} (\mathbf{X}_{i_1} \dots \mathbf{X}_{i_\gamma} \mathbf{Z}_{k_1} \dots \mathbf{Z}_{k_\gamma} + \mathbf{Z}_{k_1} \dots \mathbf{Z}_{k_\gamma} \mathbf{X}_{i_1} \dots \mathbf{X}_{i_\gamma}) + \text{Rest}, \quad (159)$$

$$\left\langle \left( \frac{\mathbf{A}_{1,\gamma}}{2} \right)^{2\gamma} \right\rangle_{\rho^{\otimes N}} = 2 \frac{1}{N^{2\gamma}} \frac{N!}{(N-2\gamma)!} \mathbf{x}^\gamma \mathbf{z}^\gamma + \left\langle \frac{\text{Rest}}{N^{2\gamma}} \right\rangle_{\rho^{\otimes N}},$$

and then we apply the limit

$$\begin{aligned} \lim_{N \rightarrow \infty} \left\langle \left( \frac{\mathbf{A}_{1,\gamma}}{2} \right)^{2\gamma} \right\rangle_{\rho^{\otimes N}} &= 2 (\mathbf{xz})^\gamma, \quad \text{similarly} \\ \lim_{N \rightarrow \infty} \left\langle \left( \frac{\mathbf{A}_{2,\gamma}}{2} \right)^{2\gamma} \right\rangle_{\rho^{\otimes N}} &= 2 (\mathbf{yz})^\gamma \quad \text{as well as} \\ \lim_{N \rightarrow \infty} \left\langle \left( \frac{\mathbf{A}_{3,\gamma}}{2} \right)^{2\gamma} \right\rangle_{\rho^{\otimes N}} &= 2 (\mathbf{xy})^\gamma. \end{aligned} \quad (160)$$

The numerical range of  $\frac{1}{j^{2\gamma}} \vec{E}_\gamma$ , where  $\vec{E}_\gamma$  is from (138), is the convex hull of points  $2((\mathbf{xz})^\gamma, (\mathbf{yz})^\gamma, (\mathbf{xy})^\gamma)$ . However, we want the range  $\mathcal{E}_\gamma^{\text{US}}$  of  $\frac{1}{a_{M,\gamma}} \vec{E}_\gamma$ , where  $a_{M,\gamma}$  is the maximum eigenvalue of the (unitary equivalent) anticommutators  $A_{t,\gamma}$  and  $t = 1, 2, 3$ .

In Fig. 21, we display  $\frac{a_{M,\gamma}}{j^{2\gamma}}$  as a function of  $j$  for  $\gamma = 1, \dots, 6$ , which indicates that

$$\lim_{j \rightarrow \infty} \frac{a_{M,\gamma}}{j^{2\gamma}} = \frac{1}{2^{\gamma-1}}. \quad (161)$$

Hence, in the limit  $j \rightarrow \infty$ , the numerical range  $\mathcal{E}_\gamma^{\text{US}}$  of

$\frac{1}{a_{M,\gamma}} \vec{E}_\gamma$  is the convex hull of

$$\begin{aligned} \mathcal{A}_\gamma &= \{((2\mathbf{xz})^\gamma, (2\mathbf{yz})^\gamma, (2\mathbf{xy})^\gamma) | 0 \leq \mu \leq \pi, 0 \leq \nu < 2\pi\} \\ &= \{(\mathbf{a}_1, \mathbf{a}_2, \mathbf{a}_3) \in \mathcal{H}^{\text{US}} | (\mathbf{a}_1 \mathbf{a}_2)^{\frac{2}{\gamma}} + (\mathbf{a}_2 \mathbf{a}_3)^{\frac{2}{\gamma}} + (\mathbf{a}_3 \mathbf{a}_1)^{\frac{2}{\gamma}} \\ &= 2(\mathbf{a}_1 \mathbf{a}_2 \mathbf{a}_3)^{\frac{1}{\gamma}}\}, \end{aligned} \quad (162)$$

where the hyperrectangle  $\mathcal{H}^{\text{US}}$  is  $[0, 1]^{\times 3}$  and  $[-1, 1]^{\times 3}$  for an even and odd  $\gamma$ . The equation in second expression of  $\mathcal{A}_\gamma$  comes from the normalization condition,  $\vec{r} \cdot \vec{r} = 1$ , of the Bloch vector in (153). In Fig. 19, we exhibit  $\mathcal{A}_\gamma$  for  $\gamma = 1, \dots, 4$ .

One can perceive that, for  $\gamma = 1$ ,  $\mathcal{A}_\gamma$  is Steiner's Roman surface characterized by Eq. (117). In this case, tight URs and CRs will be (98)–(101) [see (121)]. Like the previous example, in the case of an even power  $\gamma$ , we do not get a non-trivial UR or CR because four corners of the hyperrectangle  $\mathcal{H}^{\text{US}} = [0, 1]^{\times 3}$  fall in the range  $\mathcal{E}_\gamma^{\text{US}}$ . Next one can check that, for  $\gamma > 4$ , the shape of  $\mathcal{A}_\gamma$  is similar to  $\mathcal{A}_3$  and  $\mathcal{A}_4$  in the case of an odd and even  $\gamma$ , respectively. Hence, the permitted region is the octahedron and tetrahedron,

$$\begin{aligned} \mathcal{E}_\gamma^{\text{US}} &= \text{Conv}\{(\pm 1, 0, 0), (0, \pm 1, 0), (0, 0, \pm 1)\} \text{ and} \\ \mathcal{E}_\gamma^{\text{US}} &= \text{Conv}\{(0, 0, 0), (1, 0, 0), (0, 1, 0), (0, 0, 1)\}, \end{aligned} \quad (163)$$

for an odd and even  $\gamma \geq 3$ , respectively. In the case of the octahedron, one will have the same tight URs and CRs (125)–(128) for the anticommutators.

Figure 21 also carries the plots of  $\frac{a_{M,\gamma}}{j^{2\gamma}}$ ,  $\frac{\lambda_{M,\gamma}(\theta_1, \phi_1)}{j^{2\gamma}}$ , and  $\frac{\lambda_{m,\gamma}(\theta_1, \phi_1)}{j^{2\gamma}}$  as functions of  $j = 1, 2, \dots, 50$  for different  $\gamma$ 's.  $a_{m,\gamma}$  represents the minimum eigenvalue of the anticommutators  $A_{t,\gamma}$ , and  $a_{m,\gamma} = -a_{M,\gamma}$  when  $\gamma$  is a positive odd number. Similarly, for an odd  $\gamma$ , the minimum eigenvalue  $\lambda_{m,\gamma}(\theta_1, \phi_1)$  is same in magnitude but opposite in sign of the maximum eigenvalue  $\lambda_{M,\gamma}(\theta_1, \phi_1)$  of the operator  $\hat{\eta}_1 \cdot \vec{E}_\gamma$  [ $\vec{E}_\gamma$  is given in (138)]. The plots in Fig. 21 indicate that

$$\begin{aligned} \lim_{j \rightarrow \infty} \frac{a_{m,\gamma}}{j^{2\gamma}} &= 0 \quad \text{for an even } \gamma > 1, \\ \lim_{j \rightarrow \infty} \frac{\lambda_{M,\gamma}(\theta_1, \phi_1)}{j^{2\gamma}} &= \begin{cases} \frac{2}{\sqrt{3}} & \text{for } \gamma = 1 \\ \frac{2}{3\sqrt{3}} & \text{for } \gamma = 2, \text{ and} \\ \frac{1}{2^{\gamma-1}\sqrt{3}} & \text{for } \gamma \geq 3 \end{cases} \\ \lim_{j \rightarrow \infty} \frac{\lambda_{m,\gamma}(\theta_1, \phi_1)}{j^{2\gamma}} &= 0 \quad \text{for an even } \gamma > 1, \end{aligned} \quad (164)$$

which supports the above results secured via the quantum de Finetti theorem.

## IX. SUMMARY AND OUTLOOK

In this paper, we studied three kinds of Hermitian operators: the combinations  $(X_\gamma, Y_\gamma)$  of powers of the ladder operators, powers of the angular momentum operators  $(J_x^\gamma, J_y^\gamma, J_z^\gamma)$ , and their anticommutator

$(A_{1,\gamma}, A_{2,\gamma}, A_{3,\gamma})$ . In each case, we presented the joint numerical range  $\mathcal{E}$  and tight lower and upper bounds for URs and CRs, respectively. Essentially, all the main results are displayed in Figs. 1–21.

Boundary  $\partial\mathcal{E}$  of the allowed region is entirely generated by the maximum-eigenvalue-kets of  $\Lambda(\theta, \phi)$ . In simple cases, where the angular momentum quantum number  $j$  is small, we provided analytical expressions of its maximum eigenvalue  $\lambda_m(\theta, \phi)$ , the associated eigenkets  $|\theta, \phi\rangle$ , and the boundary  $\partial\mathcal{E}$ . For large quantum numbers, we obtained these numerically. Up to  $j = 50$ , the bounds for tight URs and CRs are also gained numerically by exploiting a finite set of boundary points. The limiting case  $j \rightarrow \infty$  is handled by applying the quantum de Finetti theorem on a  $N$ -qubit system, where  $N \rightarrow \infty$ , and the allowed regions as well as tight URs and CRs are achieved.

In the case of  $(J_x, J_y, J_z)$ ,  $(X_\gamma, Y_\gamma)$ , and for a pair of the anticommutators  $(A_t, A_{t' \neq t})$ , recall that  $A_t = A_{t, \gamma=1}$ , the allowed region is bounded by a sphere (circle, in the case of two operators) centered at the origin for all the quantum numbers  $j$ . Their lower and upper bounds in the tight URs and CRs do not change with  $j$ . In the case of  $(J_x^2, J_y^2)$ , the numerical range changes its shape from triangular to elliptical to triangular as  $j$  goes from 1 to infinity. In this case, the lower bounds decrease and upper bounds increase as  $j$  grows, and they reach their trivial values in the limit  $j \rightarrow \infty$ .

In the case of anticommutators, after the uniform scaling, the allowed region  $\mathcal{E}^{\text{us}}$  for  $\frac{1}{a_m}(A_1, A_2, A_3)$  is the convex hull of a Roman surface for both  $j = 1$  and  $j \rightarrow \infty$ . Whereas, for  $j = \frac{3}{2}, 2$ ,  $\mathcal{E}^{\text{us}}$  is a unit ball centered at  $(0, 0, 0)$ , then it starts contracting in four directions and expanding in their antipodal directions as  $j$  increases. One of our tight URs for  $(A_1, A_2, A_3)$  does not change with  $j$ , whereas the other grows weaker because its lower bound decreases with  $j$  but it never becomes trivial even in the limit  $j \rightarrow \infty$ . Likewise, our tight CRs for the anticommutators grow weaker with the expansion of  $\mathcal{E}^{\text{us}}$  but they stay nontrivial for all  $j$ s.

In the case of odd powers  $\gamma > 1$ , the numerical range  $\mathcal{E}^{\text{us}}$  of  $\frac{1}{j^\gamma}(J_x^\gamma, J_y^\gamma, J_z^\gamma)$  shrinks from a ball to an octahedron as the quantum number  $j$  rises. With the rise of  $j$ , some of our tight URs and CRs stay as they are, whereas one CR becomes stronger because of its upper bound decreases with the contraction of  $\mathcal{E}^{\text{us}}$ .

In the case of an even power  $\gamma > 2$ , particularly for  $(J_x^4, J_y^4, J_z^4)$ , we discovered that distinct eigenvalues of  $\Lambda(\theta, \phi)$  cross each other and dominate in different parts of the parameter space. As a result of this level crossing and the disappearance of the gap between eigenvalues, the largest eigenvalue  $\lambda_m(\theta, \phi)$  of  $\Lambda$  turns degenerate in different sections of the parameter space, and thus we observe flat faces on the boundary of the allowed region. The degeneracy is a necessary but not sufficient requirement for  $\mathcal{E}$  to have a flat face. For small quantum numbers, it is difficult to predict the shape of  $\mathcal{E}$  for  $(J_x^4, J_y^4, J_z^4)$ , but around  $j = 10$  the allowed region roughly takes the shape

that is suggested by the quantum de Finetti theorem for  $j \rightarrow \infty$ . For  $(J_x^4, J_y^4, J_z^4)$ , our tight URs and CRs turn weaker as  $j$  grows, and they become trivial in the limit  $j \rightarrow \infty$ .

With the de Finetti theorem, when  $\gamma > 2$  and  $j \rightarrow \infty$ , we realized that the numerical range of  $\frac{1}{j^\gamma}(J_x^\gamma, J_y^\gamma, J_z^\gamma)$  is an octahedron for an odd  $\gamma$  and is bounded by one curved and four plane surfaces for an even  $\gamma$ , and the numerical range of  $\frac{1}{a_{m,\gamma}}(A_{1,\gamma}, A_{2,\gamma}, A_{3,\gamma})$  is an octahedron and tetrahedron for an odd and even  $\gamma$ .

Recently, quantum phase transitions are explored through the joint numerical range of certain observables in [2, 7–11]. Results from this paper may become useful for such an investigation as operators, for example,  $\mathbf{J}_x^\gamma$  and  $\mathbf{A}_{1,\gamma}$  represent  $\gamma$ - and  $2\gamma$ -body interactions between qubits.

## ACKNOWLEDGMENTS

I am very grateful to Aditi Sen(De), Ujjwal Sen, and Arun Kumar Pati for many helpful discussions.

## Appendix: Supplementary material

For  $j = \frac{3}{2}, 2, \frac{5}{2}, \dots, 50$ , the values of  $\mathfrak{h}$  displayed in Fig. 6 are

0.491551, 0.491551, 0.41986, 0.427261,  
0.351636, 0.356853, 0.302929, 0.30647,  
0.266717, 0.269349, 0.238819, 0.240789,  
0.216628, 0.218167, 0.198523, 0.199764,  
0.183432, 0.184472, 0.170624, 0.171533,  
0.15963, 0.160408, 0.15008, 0.150755,  
0.141701, 0.142292, 0.134283, 0.134806,  
0.127667, 0.128132, 0.121724, 0.122142,  
0.116355, 0.116733, 0.111478, 0.111821,  
0.107026, 0.107339, 0.102945, 0.103232,  
0.0991885, 0.0994531, 0.0957188, 0.0959634,  
0.0925031, 0.0927299, 0.0895138, 0.0897248,  
0.0867271, 0.0869239, 0.0841192, 0.0843066,  
0.0816738, 0.0818534, 0.0793778, 0.0795465,  
0.0772175, 0.0773764, 0.0751809, 0.0753308,  
0.0732574, 0.0733991, 0.0714375, 0.0715717,  
0.0697129, 0.0698402, 0.0680761, 0.068197,  
0.0665204, 0.0666353, 0.0650396, 0.0651491,  
0.0636285, 0.0637329, 0.062282, 0.0623817,  
0.0609957, 0.061091, 0.0597655, 0.0598567,  
0.0585877, 0.0586752, 0.0574591, 0.0575429,  
0.0563764, 0.0564569, 0.0553368, 0.0554142,  
0.0543379, 0.0544122, 0.053377, 0.0534486,  
0.0524522, 0.0525211, 0.0515612, 0.0516277,  
0.0507023, 0.0507664.

For  $j = \frac{3}{2}, 2, \frac{5}{2}, \dots, 50$ , the values of  $u_{1/2}$  displayed in Fig. 6 are

2.36603, 2.36603, 2.32112, 2.32112, 2.28897,  
2.28897, 2.26491, 2.26491, 2.2461, 2.2461,  
2.23089, 2.23089, 2.21825, 2.21825, 2.20753,

TABLE IV. For  $\gamma = 2$ , the eigenkets  $|\phi\rangle_k \in \mathcal{S}_k^\gamma$  are presented below. They correspond to the maximum eigenvalue  $\lambda_M$  [listed in Table I] of  $\Lambda_2(\phi)$ . Note that, for a given  $j$ , an invariant space  $\mathcal{S}^2$  of  $\Lambda_2(\phi)$  belongs to the Hilbert space  $\mathcal{H}_d$ , where  $d = 2j + 1$ . Therefore, for example,  $\mathcal{S}_0^2$  for distinct  $j$ -values are distinct subspaces.

$j$	Eigenkets
$\frac{1}{2}$	All kets in the Hilbert space $\mathcal{H}_2$
1	$ \phi\rangle_0 = \frac{1}{\sqrt{2}} (e^{i\phi} +1\rangle +  -1\rangle) \in \mathcal{S}_0^2 \subset \mathcal{H}_3$
$\frac{3}{2}$	$ \phi\rangle_0 = \frac{1}{\sqrt{2}} (e^{i\phi} +\frac{3}{2}\rangle +  -\frac{1}{2}\rangle) \in \mathcal{S}_0^2 \subset \mathcal{H}_4$ $ \phi\rangle_1 = \frac{1}{\sqrt{2}} (e^{i\phi} +\frac{1}{2}\rangle +  -\frac{3}{2}\rangle) \in \mathcal{S}_1^2 \subset \mathcal{H}_4$
2	$ \phi\rangle_0 = \frac{1}{2} (e^{i2\phi} +2\rangle + \sqrt{2}e^{i\phi} 0\rangle +  -2\rangle) \in \mathcal{S}_0^2 \subset \mathcal{H}_5$
$\frac{5}{2}$	$ \phi\rangle_0 = \frac{1}{\sqrt{28}} (\sqrt{5}e^{i2\phi} +\frac{5}{2}\rangle + \sqrt{14}e^{i\phi} +\frac{1}{2}\rangle + 3 -\frac{3}{2}\rangle) \in \mathcal{S}_0^2 \subset \mathcal{H}_6$ $ \phi\rangle_1 = \frac{1}{\sqrt{28}} (3e^{i2\phi} +\frac{3}{2}\rangle + \sqrt{14}e^{i\phi} -\frac{1}{2}\rangle + \sqrt{5} -\frac{5}{2}\rangle) \in \mathcal{S}_1^2 \subset \mathcal{H}_6$
3	$ \phi\rangle_0 = \frac{1}{\sqrt{8(4+\sqrt{6})}} (\sqrt{5}e^{i3\phi} +3\rangle + (2\sqrt{2} + \sqrt{3})e^{i2\phi} +1\rangle + (2\sqrt{2} + \sqrt{3})e^{i\phi} -1\rangle + \sqrt{5} -3\rangle) \in \mathcal{S}_0^2 \subset \mathcal{H}_7$
$\frac{7}{2}$	$ \phi\rangle_0 = \frac{(6-\sqrt{21})\sqrt{21+4\sqrt{21}}e^{i3\phi} +\frac{7}{2}\rangle + 3(\sqrt{3}+2\sqrt{7})e^{i2\phi} +\frac{3}{2}\rangle + \sqrt{15}\sqrt{21+4\sqrt{21}}e^{i\phi} -\frac{1}{2}\rangle + 15 -\frac{5}{2}\rangle}{\sqrt{72(14+\sqrt{21})}} \in \mathcal{S}_0^2 \subset \mathcal{H}_8$ $ \phi\rangle_1 = \frac{(14-\sqrt{21})\sqrt{21+4\sqrt{21}}e^{i3\phi} +\frac{5}{2}\rangle + 7\sqrt{5}(2\sqrt{3}+\sqrt{7})e^{i2\phi} +\frac{1}{2}\rangle + 5\sqrt{7}\sqrt{21+4\sqrt{21}}e^{i\phi} -\frac{3}{2}\rangle + 35 -\frac{7}{2}\rangle}{\sqrt{1960(6+\sqrt{21})}} \in \mathcal{S}_1^2 \subset \mathcal{H}_8$
4	$ \phi\rangle_0 = \frac{1}{\sqrt{208}} (\sqrt{7}e^{i4\phi} +4\rangle + 2\sqrt{13}e^{i3\phi} +2\rangle + 3\sqrt{10}e^{i2\phi} 0\rangle + 2\sqrt{13}e^{i\phi} -2\rangle + \sqrt{7} -4\rangle) \in \mathcal{S}_0^2 \subset \mathcal{H}_9$

TABLE V. Like Table IV, the maximum-eigenvalue-kets  $|\phi\rangle_k \in \mathcal{S}_k^\gamma$  of  $\Lambda_\gamma(\phi)$  are registered here for  $\gamma = 3$  and  $\gamma = 4$ .

$j$	Eigenkets for $\gamma = 3$	Eigenkets for $\gamma = 4$
$\frac{1}{2}$	All kets in the Hilbert space $\mathcal{H}_2$	All kets in the Hilbert space $\mathcal{H}_2$
1	All kets in the Hilbert space $\mathcal{H}_3$	All kets in the Hilbert space $\mathcal{H}_3$
$\frac{3}{2}$	$ \phi\rangle_0 = \frac{1}{\sqrt{2}} (e^{i\phi} +\frac{3}{2}\rangle +  -\frac{3}{2}\rangle) \in \mathcal{S}_0^3 \subset \mathcal{H}_4$	All kets in the Hilbert space $\mathcal{H}_4$
2	$ \phi\rangle_0 = \frac{1}{\sqrt{2}} (e^{i\phi} +2\rangle +  -1\rangle) \in \mathcal{S}_0^3 \subset \mathcal{H}_5$ $ \phi\rangle_1 = \frac{1}{\sqrt{2}} (e^{i\phi} +1\rangle +  -2\rangle) \in \mathcal{S}_1^3 \subset \mathcal{H}_5$	$ \phi\rangle_0 = \frac{1}{\sqrt{2}} (e^{i\phi} +2\rangle +  -2\rangle) \in \mathcal{S}_0^4 \subset \mathcal{H}_5$
$\frac{5}{2}$	$ \phi\rangle_1 = \frac{1}{\sqrt{2}} (e^{i\phi} +\frac{3}{2}\rangle +  -\frac{3}{2}\rangle) \in \mathcal{S}_1^3 \subset \mathcal{H}_6$	$ \phi\rangle_0 = \frac{1}{\sqrt{2}} (e^{i\phi} +\frac{5}{2}\rangle +  -\frac{3}{2}\rangle) \in \mathcal{S}_0^4 \subset \mathcal{H}_6$ $ \phi\rangle_1 = \frac{1}{\sqrt{2}} (e^{i\phi} +\frac{3}{2}\rangle +  -\frac{5}{2}\rangle) \in \mathcal{S}_1^4 \subset \mathcal{H}_6$
3	$ \phi\rangle_0 = \frac{1}{2} (e^{i2\phi} +3\rangle + \sqrt{2}e^{i\phi} 0\rangle +  -3\rangle) \in \mathcal{S}_0^3 \subset \mathcal{H}_7$ $ \phi\rangle_1 = \frac{1}{\sqrt{2}} (e^{i\phi} +2\rangle +  -1\rangle) \in \mathcal{S}_1^3 \subset \mathcal{H}_7$ $ \phi\rangle_2 = \frac{1}{\sqrt{2}} (e^{i\phi} +1\rangle +  -2\rangle) \in \mathcal{S}_2^3 \subset \mathcal{H}_7$	$ \phi\rangle_1 = \frac{1}{\sqrt{2}} (e^{i\phi} +2\rangle +  -2\rangle) \in \mathcal{S}_1^4 \subset \mathcal{H}_7$
$\frac{7}{2}$	$ \phi\rangle_0 = \frac{\sqrt{7}e^{i2\phi} +\frac{7}{2}\rangle + \sqrt{23}e^{i\phi} +\frac{1}{2}\rangle + 4 -\frac{5}{2}\rangle}{\sqrt{46}} \in \mathcal{S}_0^3 \subset \mathcal{H}_8$ $ \phi\rangle_1 = \frac{4e^{i2\phi} +\frac{5}{2}\rangle + \sqrt{23}e^{i\phi} -\frac{1}{2}\rangle + \sqrt{7} -\frac{7}{2}\rangle}{\sqrt{46}} \in \mathcal{S}_1^3 \subset \mathcal{H}_8$	$ \phi\rangle_1 = \frac{1}{\sqrt{2}} (e^{i\phi} +\frac{5}{2}\rangle +  -\frac{3}{2}\rangle) \in \mathcal{S}_1^4 \subset \mathcal{H}_8$ $ \phi\rangle_2 = \frac{1}{\sqrt{2}} (e^{i\phi} +\frac{3}{2}\rangle +  -\frac{5}{2}\rangle) \in \mathcal{S}_2^4 \subset \mathcal{H}_8$
4	$ \phi\rangle_1 = \frac{1}{2} (e^{i2\phi} +3\rangle + \sqrt{2}e^{i\phi} 0\rangle +  -3\rangle) \in \mathcal{S}_1^3 \subset \mathcal{H}_9$	$ \phi\rangle_2 = \frac{1}{\sqrt{2}} (e^{i\phi} +2\rangle +  -2\rangle) \in \mathcal{S}_2^4 \subset \mathcal{H}_9$

2.20753, 2.19829, 2.19829, 2.19021, 2.19021, 2.18307, 2.18307, 2.1767, 2.1767, 2.17096, 2.17096, 2.16577, 2.16577, 2.16103, 2.16103, 2.15668, 2.15668, 2.15268, 2.15268, 2.14898, 2.14898, 2.14553, 2.14553, 2.14233, 2.14233, 2.13933, 2.13933, 2.13651, 2.13651, 2.13387, 2.13387, 2.13137, 2.13137, 2.12901, 2.12901, 2.12678, 2.12678, 2.12466, 2.12466, 2.12265, 2.12265, 2.12073, 2.12073, 2.1189, 2.1189, 2.11716, 2.11716, 2.11549, 2.11549, 2.11389, 2.11389, 2.11235, 2.11235, 2.11088, 2.11088, 2.10947, 2.10947, 2.10811, 2.10811, 2.1068, 2.1068, 2.10553, 2.10553, 2.10432, 2.10432, 2.10314, 2.10314, 2.102, 2.102, 2.1009,

2.1009, 2.09984, 2.09984, 2.09881, 2.09881,  
2.09781, 2.09781, 2.09684, 2.09684, 2.0959,  
2.0959, 2.09499, 2.09499.

For  $j = \frac{3}{2}, 2, \frac{5}{2}, \dots, 50$ , the values of  $u_2$  displayed in Fig. 6 are

1.75, 1.75, 1.78071, 1.7736, 1.82246, 1.81637,  
1.85267, 1.84851, 1.87446, 1.87161, 1.89076,  
1.88872, 1.90336, 1.90183, 1.91337, 1.91219,  
1.92153, 1.92058, 1.9283, 1.92752, 1.93399,  
1.93334, 1.93885, 1.9383, 1.94304, 1.94257,  
1.9467, 1.94629, 1.94992, 1.94956, 1.95277,  
1.95245, 1.95531, 1.95503, 1.9576, 1.95735,  
1.95966, 1.95944, 1.96153, 1.96133, 1.96324,  
1.96305, 1.9648, 1.96463, 1.96623, 1.96608,  
1.96755, 1.96741, 1.96878, 1.96864, 1.96991,  
1.96979, 1.97096, 1.97085, 1.97195, 1.97184,  
1.97287, 1.97277, 1.97373, 1.97363, 1.97453,  
1.97445, 1.97529, 1.97521, 1.97601, 1.97593,  
1.97668, 1.97661, 1.97732, 1.97725, 1.97792,  
1.97786, 1.9785, 1.97844, 1.97904, 1.97898,  
1.97956, 1.9795, 1.98005, 1.98, 1.98052,  
1.98047, 1.98097, 1.98092, 1.98139, 1.98135,  
1.9818, 1.98176, 1.98219, 1.98215, 1.98257,  
1.98253, 1.98293, 1.98289, 1.98327, 1.98324,  
1.9836, 1.98357.

For  $j = \frac{3}{2}, 2, \frac{5}{2}, \dots, 50$ , the values of  $u_{\max}$  displayed in Fig. 6 are

1.86603, 1.86603, 1.88192, 1.87766, 1.9052,  
1.90139, 1.92211, 1.91953, 1.93416, 1.93244,  
1.94306, 1.94186, 1.94988, 1.94899, 1.95525,  
1.95458, 1.95959, 1.95906, 1.96317, 1.96274,  
1.96616, 1.96581, 1.96871, 1.96841, 1.9709,  
1.97065, 1.97281, 1.97259, 1.97448, 1.97429,  
1.97596, 1.97579, 1.97728, 1.97713, 1.97846,  
1.97832, 1.97952, 1.9794, 1.98049, 1.98038,  
1.98136, 1.98127, 1.98216, 1.98208, 1.9829,  
1.98282, 1.98358, 1.9835, 1.9842, 1.98413,  
1.98478, 1.98472, 1.98532, 1.98526, 1.98582,  
1.98577, 1.98629, 1.98624, 1.98673, 1.98668,  
1.98714, 1.9871, 1.98753, 1.98749, 1.98789,  
1.98786, 1.98824, 1.9882, 1.98856, 1.98853,  
1.98887, 1.98884, 1.98916, 1.98913, 1.98944,  
1.98941, 1.9897, 1.98967, 1.98995, 1.98992,  
1.99019, 1.99016, 1.99042, 1.99039, 1.99063,  
1.99061, 1.99084, 1.99082, 1.99104, 1.99102,  
1.99123, 1.99121, 1.99141, 1.99139, 1.99158,  
1.99156, 1.99175, 1.99173.

For  $j = \frac{3}{2}, 2, \frac{5}{2}, \dots, 50$ , the values of  $\frac{\langle \theta_1, \phi_1 | A_1 | \theta_1, \phi_1 \rangle}{a_M}$  given in (119) are

0.57735, 0.57735, 0.629941, 0.632993,  
0.644427, 0.64715, 0.650684, 0.652506,  
0.654182, 0.65539, 0.656421, 0.65726,  
0.657979, 0.658592, 0.659125, 0.659592,  
0.660004, 0.660371, 0.660699, 0.660995,  
0.661263, 0.661507, 0.66173, 0.661934,  
0.662122, 0.662296, 0.662457, 0.662606,  
0.662745, 0.662875, 0.662997, 0.663111,

0.663218, 0.663319, 0.663414, 0.663504,  
0.663589, 0.66367, 0.663747, 0.663819,  
0.663888, 0.663954, 0.664017, 0.664077,  
0.664134, 0.664189, 0.664242, 0.664292,  
0.66434, 0.664387, 0.664431, 0.664474,  
0.664515, 0.664555, 0.664593, 0.66463,  
0.664666, 0.6647, 0.664734, 0.664766,  
0.664797, 0.664827, 0.664856, 0.664884,  
0.664912, 0.664938, 0.664964, 0.664989,  
0.665013, 0.665037, 0.66506, 0.665082,  
0.665103, 0.665125, 0.665145, 0.665165,  
0.665184, 0.665203, 0.665222, 0.66524,  
0.665258, 0.665275, 0.665291, 0.665308,  
0.665324, 0.665339, 0.665355, 0.665369,  
0.665384, 0.665398, 0.665412, 0.665426,  
0.665439, 0.665452, 0.665465, 0.665477,  
0.66549, 0.665502.

For  $j = \frac{3}{2}, 2, \frac{5}{2}, \dots, 50$ , the values of  $\mathfrak{h}$  showcased in Fig. 10 are

1.38629, 1.38629, 1.38629, 1.38629, 1.38629,  
1.38629, 1.38629, 1.38533, 1.38141, 1.37857,  
1.37614, 1.37415, 1.37246, 1.371, 1.36974,  
1.36863, 1.36765, 1.36678, 1.36599, 1.36529,  
1.36465, 1.36407, 1.36354, 1.36305, 1.3626,  
1.36218, 1.3618, 1.36144, 1.36111, 1.3608,  
1.36051, 1.36023, 1.35998, 1.35973, 1.35951,  
1.35929, 1.35909, 1.35889, 1.35871, 1.35854,  
1.35837, 1.35821, 1.35806, 1.35792, 1.35778,  
1.35765, 1.35752, 1.3574, 1.35728, 1.35717,  
1.35707, 1.35696, 1.35686, 1.35677, 1.35668,  
1.35659, 1.3565, 1.35642, 1.35634, 1.35626,  
1.35619, 1.35612, 1.35605, 1.35598, 1.35591,  
1.35585, 1.35579, 1.35573, 1.35567, 1.35561,  
1.35556, 1.3555, 1.35545, 1.3554, 1.35535,  
1.3553, 1.35526, 1.35521, 1.35517, 1.35512,  
1.35508, 1.35504, 1.355, 1.35496, 1.35492,  
1.35488, 1.35485, 1.35481, 1.35478, 1.35474,  
1.35471, 1.35468, 1.35464, 1.35461, 1.35458,  
1.35455, 1.35452, 1.35449.

For  $j = \frac{3}{2}, 2, \frac{5}{2}, \dots, 50$ , the values of  $u_2$  showcased in Fig. 10 are

2, 2, 2.09524, 2.10102, 2.12293, 2.12821,  
2.13508, 2.13865, 2.14193, 2.1443, 2.14633,  
2.14799, 2.1494, 2.15061, 2.15167, 2.15259,  
2.15341, 2.15413, 2.15479, 2.15537, 2.1559,  
2.15639, 2.15683, 2.15723, 2.15761, 2.15795,  
2.15827, 2.15857, 2.15885, 2.15911, 2.15935,  
2.15957, 2.15979, 2.15999, 2.16018, 2.16036,  
2.16053, 2.16069, 2.16084, 2.16098, 2.16112,  
2.16125, 2.16138, 2.1615, 2.16161, 2.16172,  
2.16183, 2.16193, 2.16202, 2.16211, 2.1622,  
2.16229, 2.16237, 2.16245, 2.16253, 2.1626,  
2.16267, 2.16274, 2.16281, 2.16287, 2.16293,  
2.16299, 2.16305, 2.16311, 2.16316, 2.16321,  
2.16327, 2.16332, 2.16336, 2.16341, 2.16346,  
2.1635, 2.16354, 2.16359, 2.16363, 2.16367,  
2.16371, 2.16374, 2.16378, 2.16382, 2.16385,  
2.16389, 2.16392, 2.16395, 2.16398, 2.16401,

2.16404, 2.16407, 2.1641, 2.16413, 2.16416,  
2.16419, 2.16421, 2.16424, 2.16427, 2.16429,  
2.16431, 2.16434.

For  $j = \frac{3}{2}, 2, \frac{5}{2}, \dots, 50$ , the values of  $u_{\max}$  showcased in Fig. 10 are

2.36603, 2.36603, 2.44491, 2.44949, 2.46664,  
2.47073, 2.47603, 2.47876, 2.48127, 2.48308,  
2.48463, 2.48589, 2.48697, 2.48789, 2.48869,  
2.48939, 2.49001, 2.49056, 2.49105, 2.49149,  
2.49189, 2.49226, 2.49259, 2.4929, 2.49318,  
2.49344, 2.49368, 2.49391, 2.49412, 2.49431,  
2.4945, 2.49467, 2.49483, 2.49498, 2.49512,  
2.49526, 2.49538, 2.49551, 2.49562, 2.49573,  
2.49583, 2.49593, 2.49603, 2.49612, 2.4962,  
2.49628, 2.49636, 2.49644, 2.49651, 2.49658,  
2.49665, 2.49671, 2.49677, 2.49683, 2.49689,  
2.49695, 2.497, 2.49705, 2.4971, 2.49715,  
2.4972, 2.49724, 2.49728, 2.49733, 2.49737,  
2.49741, 2.49745, 2.49748, 2.49752, 2.49755,  
2.49759, 2.49762, 2.49766, 2.49769, 2.49772,  
2.49775, 2.49778, 2.49781, 2.49783, 2.49786,  
2.49789, 2.49791, 2.49794, 2.49796, 2.49799,  
2.49801, 2.49803, 2.49805, 2.49808, 2.4981,  
2.49812, 2.49814, 2.49816, 2.49818, 2.4982,  
2.49822, 2.49823, 2.49825.

For  $j = 1, \frac{3}{2}, \dots, 50$ , the values of  $u_{\max}$  exhibited in Fig. 12 are

2.36603, 2.25971, 2.16889, 2.10727, 2.09897,  
2.09021, 2.07744, 2.06386, 2.05085, 2.03903,  
2.02867, 2.02463, 2.02258, 2.01986, 2.01686,  
2.01389, 2.01113, 2.00871, 2.00759, 2.00704,  
2.00634, 2.00558, 2.00484, 2.00416, 2.00357,  
2.00321, 2.00301, 2.00278, 2.00255, 2.00233,  
2.00212, 2.00194, 2.0018, 2.0017, 2.0016,  
2.0015, 2.00141, 2.00133, 2.00125, 2.00118,  
2.00113, 2.00107, 2.00102, 2.00097, 2.00093,  
2.00089, 2.00085, 2.00081, 2.00078, 2.00075,  
2.00072, 2.00069, 2.00066, 2.00064, 2.00062,  
2.00059, 2.00057, 2.00055, 2.00053, 2.00052,  
2.0005, 2.00048, 2.00047, 2.00045, 2.00044,  
2.00043, 2.00041, 2.0004, 2.00039, 2.00038,  
2.00037, 2.00036, 2.00035, 2.00034, 2.00033,  
2.00032, 2.00031, 2.0003, 2.0003, 2.00029,  
2.00028, 2.00027, 2.00027, 2.00026, 2.00026,  
2.00025, 2.00024, 2.00024, 2.00023, 2.00023,  
2.00022, 2.00022, 2.00021, 2.00021, 2.0002,  
2.0002, 2.0002, 2.00019, 2.00019.

For  $j = 1, \frac{3}{2}, \dots, 50$ , the values of  $h$  shown in Fig. 17 are

0, 1.12467, 0.467583, 0.644239, 0.510273,  
0.416216, 0.336635, 0.29168, 0.250652,  
0.216753, 0.190117, 0.168017, 0.149996,  
0.134442, 0.121554, 0.110269, 0.100723,  
0.0922493, 0.0849666, 0.0784334, 0.0727424,  
0.0675917, 0.0630542, 0.0589167, 0.0552367,  
0.0518593, 0.0488306, 0.0460353, 0.0435107,

0.0411692, 0.0390411, 0.0370587, 0.035247,  
0.0335529, 0.031997, 0.0305369, 0.0291901,  
0.0279223, 0.0267482, 0.0256398, 0.0246096,  
0.0236345, 0.0227253, 0.0218627, 0.021056,  
0.020289, 0.0195696, 0.0188843, 0.01824,  
0.017625, 0.0170455, 0.0164914, 0.0159681,  
0.015467, 0.0149928, 0.0145381, 0.0141069,  
0.0136929, 0.0132996, 0.0129215, 0.0125618,  
0.0122155, 0.0118855, 0.0115675, 0.011264,  
0.0109712, 0.0106915, 0.0104213, 0.0101628,  
0.00991295, 0.00967359, 0.00944199,  
0.00921989, 0.0090048, 0.00879831, 0.00859819,  
0.00840586, 0.00821931, 0.00803986,  
0.00786568, 0.00769796, 0.00753505,  
0.00737805, 0.00722545, 0.00707826,  
0.0069351, 0.00679691, 0.00666242, 0.00653249,  
0.00640597, 0.00628366, 0.00616448,  
0.00604919, 0.00593679, 0.00582798,  
0.00572185, 0.00561904, 0.00551871, 0.00542146.

For  $j = 1, \frac{3}{2}, \dots, 50$ , the values of  $u_{1/2}$  shown in Fig. 17 are

3, 3.73205, 3.43649, 3.53517, 3.46883,  
3.41326, 3.37114, 3.33513, 3.30647, 3.28143,  
3.26077, 3.2424, 3.22684, 3.21281, 3.20069,  
3.18963, 3.17992, 3.17098, 3.16303, 3.15566,  
3.14904, 3.14286, 3.13725, 3.13199, 3.12719,  
3.12266, 3.1185, 3.11456, 3.11092, 3.10746,  
3.10425, 3.10119, 3.09834, 3.09561, 3.09306,  
3.09061, 3.08832, 3.08611, 3.08403, 3.08204,  
3.08015, 3.07833, 3.0766, 3.07494, 3.07336,  
3.07184, 3.07038, 3.06898, 3.06763, 3.06634,  
3.06509, 3.06389, 3.06274, 3.06162, 3.06054,  
3.0595, 3.0585, 3.05753, 3.05659, 3.05568,  
3.0548, 3.05394, 3.05312, 3.05231, 3.05154,  
3.05078, 3.05005, 3.04934, 3.04864, 3.04797,  
3.04732, 3.04668, 3.04606, 3.04545, 3.04487,  
3.04429, 3.04373, 3.04319, 3.04266, 3.04214,  
3.04163, 3.04114, 3.04065, 3.04018, 3.03972,  
3.03927, 3.03883, 3.0384, 3.03798, 3.03757,  
3.03716, 3.03677, 3.03638, 3.03601, 3.03564,  
3.03527, 3.03492, 3.03457, 3.03423.

For  $j = 1, \frac{3}{2}, \dots, 50$ , the values of  $u_2$  shown in Fig. 17 are

3, 2.25, 2.76563, 2.65958, 2.74466, 2.80312,  
2.85131, 2.87386, 2.89556, 2.91262, 2.9257,  
2.93601, 2.94425, 2.95117, 2.95675, 2.96153,  
2.96548, 2.96892, 2.97182, 2.97438, 2.97656,  
2.97851, 2.98021, 2.98173, 2.98306, 2.98427,  
2.98534, 2.98632, 2.98719, 2.98799, 2.98871,  
2.98938, 2.98998, 2.99053, 2.99104, 2.99151,  
2.99194, 2.99235, 2.99272, 2.99306, 2.99338,  
2.99369, 2.99396, 2.99423, 2.99447, 2.9947,  
2.99492, 2.99512, 2.99531, 2.99549, 2.99566,  
2.99582, 2.99597, 2.99612, 2.99625, 2.99638,  
2.9965, 2.99662, 2.99673, 2.99684, 2.99694,  
2.99703, 2.99712, 2.99721, 2.99729, 2.99737,  
2.99745, 2.99752, 2.99759, 2.99766, 2.99772,  
2.99778, 2.99784, 2.9979, 2.99795, 2.99801,

2.99806, 2.9981, 2.99815, 2.9982, 2.99824,  
2.99828, 2.99832, 2.99836, 2.9984, 2.99844,  
2.99847, 2.9985, 2.99854, 2.99857, 2.9986,  
2.99863, 2.99866, 2.99869, 2.99871, 2.99874,  
2.99876, 2.99879, 2.99881.

For  $j = 1, \frac{3}{2}, \dots, 50$ , the values of  $u_{\max}$  shown in Fig. 17 are

3, 2.5, 2.875, 2.81354, 2.86259, 2.89639,  
2.92288, 2.93487, 2.94638, 2.95534, 2.96215,  
2.96749, 2.97174, 2.97528, 2.97814, 2.98058,  
2.98259, 2.98434, 2.98581, 2.98711, 2.98821,  
2.9892, 2.99005, 2.99082, 2.99149, 2.9921,  
2.99264, 2.99314, 2.99357, 2.99398, 2.99434,  
2.99467, 2.99498, 2.99526, 2.99551, 2.99575,

2.99596, 2.99617, 2.99635, 2.99653, 2.99669,  
2.99684, 2.99698, 2.99711, 2.99723, 2.99735,  
2.99745, 2.99756, 2.99765, 2.99774, 2.99783,  
2.99791, 2.99798, 2.99806, 2.99812, 2.99819,  
2.99825, 2.99831, 2.99836, 2.99842, 2.99847,  
2.99851, 2.99856, 2.9986, 2.99865, 2.99869,  
2.99872, 2.99876, 2.99879, 2.99883, 2.99886,  
2.99889, 2.99892, 2.99895, 2.99898, 2.999,  
2.99903, 2.99905, 2.99908, 2.9991, 2.99912,  
2.99914, 2.99916, 2.99918, 2.9992, 2.99922,  
2.99923, 2.99925, 2.99927, 2.99928, 2.9993,  
2.99931, 2.99933, 2.99934, 2.99936, 2.99937,  
2.99938, 2.99939, 2.99941.

- 
- [1] R. Schwonnek, L. Dammeier, and R. F. Werner, Phys. Rev. Lett. **119**, 170404 (2017).  
[2] K. Szymański, e-print arXiv:1707.03464 [quant-ph].  
[3] S. Weis, Linear Algebra Its Appl. **435**, 3168 (2011).  
[4] K. E. Gustafson and D. K.M. Rao, *Numerical range: the field of values of linear operators and matrices* (Springer-Verlag, New York, 1997).  
[5] D. S. Keeler, L. Rodman, and I. M. Spitkovsky, Linear Algebra Its Appl. **252**, 115 (1997).  
[6] K. Szymański, S. Weis, and K. Życzkowski, Linear Algebra Its Appl. **545**, 148 (2018).  
[7] J. Chen, Z. Ji, C.-K. Li, Y.-T. Poon, Y. Shen, N. Yu, B. Zeng, and D. Zhou, New J. Phys. **17**, 083019 (2015).  
[8] V. Zauner, D. Draxler, L. Vanderstraeten, J. Haegeman, and F. Verstraete, New J. Phys. **18**, 113033 (2016).  
[9] J.-Y. Chen, Z. Ji, Z.-X. Liu, Y. Shen, and B. Zeng, Phys. Rev. A **93**, 012309 (2016).  
[10] J.-Y. Chen, Z. Ji, Z.-X. Liu, X. Qi, N. Yu, B. Zeng, and D. Zhou, Sci. China-Phys. Mech. Astron. **60**, 020311 (2017).  
[11] J. Chen, C. Guo, Z. Ji, Y.-T. Poon, N. Yu, B. Zeng, and J. Zhou, Sci. China-Phys. Mech. Astron. **60**, 020312 (2017).  
[12] K. Szymański and K. Życzkowski, e-print arXiv:1804.06191 [quant-ph].  
[13] L. Maccone and A. K. Pati, Phys. Rev. Lett. **113**, 260401 (2014).  
[14] R. Schwonnek and R. F. Werner, e-print arXiv:1802.08342 [quant-ph] and arXiv:1802.08343 [quant-ph].  
[15] A. Sehwat, e-print arXiv:1706.09319 [quant-ph].  
[16] G. Kimura, Phys. Lett. A **314**, 339 (2003).  
[17] M. S. Byrd and N. Khaneja, Phys. Rev. A **68**, 062322 (2003).  
[18] J. Kaniewski, M. Tomamichel, and S. Wehner, Phys. Rev. A **90**, 012332 (2014).  
[19] A. A. Abbott, P.-L. Alzieu, M. J. W. Hall, and C. Branciari, Mathematics **4**, 8 (2016).  
[20] C. D. Meyer, *Matrix Analysis and Applied Linear Algebra* (Society for Industrial and Applied Mathematics, Philadelphia, 2000), Chap. 5, Sec. 12.  
[21] A. Sehwat, Phys. Rev. A **96**, 022111 (2017).  
[22] H. J. Landau and H. O. Pollak, Bell Syst. Tech. J. **40**, 65 (1961).  
[23] A. Lenard, J. Funct. Anal. **10**, 410 (1972).  
[24] J. Sánchez-Ruiz, Phys. Lett. A **181**, 193 (1993).  
[25] H. F. Hofmann and S. Takeuchi, Phys. Rev. A **68**, 032103 (2003).  
[26] Á. Rivas and A. Luis, Phys. Rev. A **77**, 022105 (2008).  
[27] L. Dammeier, R. Schwonnek, and R. F. Werner, New J. Phys. **17**, 093046 (2015).  
[28] A. Riccardi, C. Macchiavello, and L. Maccone, Phys. Rev. A **95**, 032109 (2017).  
[29] M. Kitagawa and M. Ueda, Phys. Rev. A **47**, 5138 (1993).  
[30] E. Størmer, J. Funct. Anal. **3**, 48 (1969).  
[31] R. L. Hudson, and G. R. Moody, Probab. Theory Relat. Fields **33**, 343 (1976).  
[32] I. Bengtsson and K. Życzkowski, *Geometry of Quantum States: An Introduction to Quantum Entanglement* (Cambridge University Press, Cambridge, 2006).  
[33] B. Grünbaum, *Convex Polytopes*, (Springer-Verlag, New York, 2003).  
[34] H. P. Robertson, Phys. Rev. **34**, 163 (1929).  
[35] H. Maassen and J. B. M. Uffink, Phys. Rev. Lett. **60**, 1103 (1988).  
[36] P. W. Atkins and J. C. Dobson, Proc. R. Soc. London Ser. A **321**, 321 (1971).  
[37] F. T. Arecchi, E. Courtens, R. Gilmore, and H. Thomas, Phys. Rev. A **6**, 2211 (1972).  
[38] D. Henrion, Acta Appl. Math. **115**, 319 (2011).  
[39] R. H. Dicke, Phys. Rev. **93**, 99 (1954).  
[40] P. Binding and C.-K. Li, Linear Algebra Its Appl. **151**, 157 (1991).